NORTHWESTERN UNIVERSITY

# Evaluation of Metal-Organic Frameworks as Adsorbent Materials with Applications in Hydrogen Storage and Carbon Dioxide Separations

A DISSERTATION

SUBMITTED TO THE GRADUATE SCHOOL
IN PARTIAL FULFILLMENT OF THE REQUIREMENTS

For the degree

DOCTOR OF PHILOSOPHY

In the field of
Chemical Engineering

By:

Houston Frost

Evanston, Illinois
December 2007

# ABSTRACT

Evaluation of Metal-Organic Frameworks as Adsorbent Materials with Applications in Hydrogen Storage and Carbon Dioxide Separations

Houston Frost

The task of designing porous materials for use in specific applications requires a detailed understanding of the adsorption process and how adsorption is affected by material properties. Applications of interest include maximizing gravimetric or volumetric adsorption capacity for hydrogen and carbon dioxide and increasing the selectivity for carbon dioxide in mixtures with other light gasses. Metal-Organic Frameworks (MOFs) are a new class of microporous materials that are synthesized via self-assembly in a "building-block" approach such that the pore size, geometry, and chemical composition can be "tailor made" to produce materials that exhibit specific adsorption and chemical behavior. This study uses a mix of classical simulations (e.g. simulating adsorption using grand canonical Monte Carlo), as well as quantum calculations, to investigate how best to design these materials for hydrogen storage and carbon dioxide separations. Ultimately, material design guidelines, in terms of surface area, free volume, and heat of adsorption are reported that would enable a material to meet hydrogen storage requirements set by the Department of Energy. Short studies are also described to test ideas for increasing the heat of adsorption in MOFs. Finally, the behavior of carbon dioxide adsorption is investigated, which provides insight into how various materials might perform in adsorption separations.

## Acknowledgements

The relationships I have built in life are the most valuable of my possessions. First and foremost, family support is the foundation of everything I produce. I cannot be more appreciative of my mother and my father, Don and Lou Frost, and the undying support for whatever intellectual pursuit I valued. My identity is a result of the freedoms they allowed me. My grandfather, Tom Frost, Jr. has been an inspiration to me since the time I understood the meaning of that word. For certain, he defined that word in my personal dictionary. The impact he has had in my life and the lives of many in his community is immeasurable. Thank you for all the wisdom lent and opportunities provided.

There have been many other mentors along the way; without whom I would certainly not be writing this manuscript. Carol Brown, my high school chemistry teacher, opened my eyes to the field of Chemistry in a way that prompted me to dedicate my post-baccalaureate career to it. Indeed, her recommendations and encouragement allowed me to begin my university research experience at the age of sixteen. At the University of Colorado, Professors David Clough, Christine Hrenya, and Alan Weimer are without a doubt the reason I decided and was able to continue my studies in graduate school. I thank them for their encouragement and support, and the important attention they give to their undergraduate students. If students are the blood, it is professors of this caliber that create the heart of a university. Finally, I have had the privilege to work with some of the most talented and brightest individuals in the fields of Chemical Engineering and Chemistry at Northwestern University. I appreciate Professor Linda Broadbelt's support; she was an integral factor in bringing me to this University. Professor Joseph Hupp has

been someone I greatly admire and I cannot thank him enough for his support during my last couple years. His respect for this research has been empowering. Most importantly, I must thank my advisor, Professor Randy Snurr. Without his guidance and understanding, I may have never crossed the finish line. He allowed me unparalleled freedoms in my research, the way in which I presented it, and in the timeline that I accomplished it. He also introduced me to a fascinating field at the crossroads between chemistry and computational modeling. Learning the techniques of his expertise and working in his research group have provided me skills that have opened the doors to a great variety of professional opportunities.

Lastly, my personal relationships have kept me grounded over the years. The list could go on as long as this paper. I want to thank Eddie Drumheller, Jon Ericson, and Ayman Salamah; their friendships were invaluable in my undergraduate years and continue today. Graduate school certainly would not have been the same without Sofia Garcia, Seth Levine, Mo Murthi, and David Dubbledam. David has been an incredible "personality" to get to know and I truly admire his dedication to his research. Mo, what can I say, I don't think I would have finished without his wisdom (without your mistakes I wouldn't have grown). As much of a friend as a mentor, he helped me every step of the way. To everyone else I'm failing to mention, there are so many, I appreciate your friendship; the world would not be the same without you.

## Table of Contents

`

## List of Figures

`

`

## List of Tables

# Chapter 1: Introduction

Twenty-first century scientists, equipped with the theories of quantum physics and statistical mechanics along with the tools of molecular modeling and computational chemistry, are thinking smaller than ever. Indeed, the engineers of the new millennium, also outfitted with this knowledge, are now looked upon to develop the products of nanotechnology. Novel materials are designed from the atomic level, and proper engineering requires not only predictable synthesis routes but also recognition of the end application during the synthesis stage. Chemists employing new found tools in supramolecular chemistry such as reticular synthesis, or the use of predetermined molecular building blocks to direct the assembly of ordered frameworks, have developed new classes of porous materials called metal-organic frameworks (MOFs)[1-6]. MOFs are generally composed of metal vertices interconnected by organic linker molecules. These materials, which are easily tailored on the molecular level, have potential applications in hydrogen storage and carbon dioxide separation and capture because of their ability to adsorb significant quantities of these gasses at reasonable pressures.

The task of designing porous materials for use in specific applications, for example maximizing gravimetric or volumetric hydrogen or carbon dioxide adsorption capacities, or increasing the selectivity of carbon dioxide in mixtures with other light gasses, requires a detailed understanding of the adsorption process and how adsorption is affected by material properties. The great variety of potential geometries and structures and different metal corner and organic linker units leads to practically innumerable possible metal-organic frameworks. In addition, the commonly used adsorption models

do not provide direct insight into the relationship between microporous material characteristics and adsorption within these materials. The daunting task of experimentally testing the seemingly unending portfolio of extended metal-containing frameworks, over 13000 crystalline structures of this type have been catalogued in the Cambridge Structure Database to date[2], can be mitigated through the use of computational techniques.

In this work, computational techniques are employed to investigate MOFs and their various applications in adsorption based technologies. Data from these computer simulations are compared to experimental data and these comparisons validate and can help improve the computational model, as well as identify potential inaccuracies, sample degradation, or impurities in the experiments.

The materials are characterized through the determination of three key properties: the accessible surface area, the free volume, and the heat of adsorption they provide with various adsorbates. Grand canonical Monte Carlo (GCMC) is used to simulate the adsorption isotherms for the various gasses of interest. In chapters 2 and 3, simulated hydrogen adsorption results in a variety of MOF materials, along with the corresponding calculated material characteristics, reveal the dependence of these characteristics on hydrogen uptake. In addition, these chapters evaluate the feasibility of these materials for use in mobile hydrogen storage technology and provide material design guidelines that must be met in order for MOFs to reach specific loading targets. Chapter 4 contains results of quantum chemical calculations used to estimate the heat of adsorption and investigate the idea of increasing the heat of adsorption through the chemical reduction of MOFs. Chapters 5 and 6 are studies on carbon dioxide adsorption and the occurrence of

inflections in the adsorption isotherms using classical (GCMC) simulations. In chapter 6, quantum calculations are also performed to estimate atomic charges in a variety of MOFs for use in classical simulations. Chapter 7 investigates carbon dioxide and methane mixtures in a metal-organic framework. Finally, chapter 8 investigates carbon dioxide and nitrogen adsorption sites in IRMOF-1 using both classical and quantum models.

### *1.1: Metal-organic frameworks*

Metal-organic frameworks (MOFs) are a new class of microporous materials with potential applications in adsorption separations, catalysis, and gas storage[5,7-9]. They are known as modular materials as they are assembled from discrete molecules referred to as molecular building blocks which can be modified to have well-defined function[10]. While there is a true alphabet soup of acronyms used for various metal-organic extended structures, including MOFs[1-6], IRMOFs[1], MOMs[11], and MMOMs[12], they more generally belong to a group of structures consisting of a metal ion or metal cluster linked by an organic moiety where the linking functionality is a cyanide, pyridal, phosphate, or carboxylate[1]. The structures of most interest in adsorption and separations are those that are three-dimensional, crystalline, and porous, and for the purpose of this discussion these are generically referred to as MOFs.

MOFs are synthesized via self-assembly chemistry where the two primary molecular building blocks, the metal ion or cluster and organic linker, are combined to form an interconnected, rigid network through a process known as reticular synthesis[1]. While the synthesis process ostensibly is straightforward, the desired regular network geometry and molecular topology are not necessarily easily obtained[10]. Furthermore, during synthesis

the frameworks often interpenetrate, which refers to the mutual intergrowth of more than one framework where the networks are physically but not chemically linked[1,10,13,14]. Usually this leads to blocked pores and lower surface area and free volume which is detrimental to adsorption, but if interpenetrated structures were properly designed it could lead to enhanced adsorbate-adsorbent interactions and acceptable pore volumes.

An example of one class of MOFs is shown in *figure 1.1*. The materials illustrated in *figure 1.1* were discovered by Yaghi and co-workers and are known specifically as isoreticular metal-organic frameworks or IRMOFs[15-17]. They feature oxide-centered $Zn_4O$ tetrahedra, serving as the vertices, each connected by six dicarboxylate linkers. A variety of linker molecules can be used to create an entire family of materials having different pore sizes and containing different chemical functionalities within the linkers but all with the same basic framework topology. In addition, different metal corners and different linkage chemistries can yield a wide variety of other framework topologies[3,7,13,18-20]. *Figure 1.2a* is a space-fill model of the unit cell of IRMOF-1 (also known as MOF-5), and *figure 1.2b* displays the extended framework of the same material.

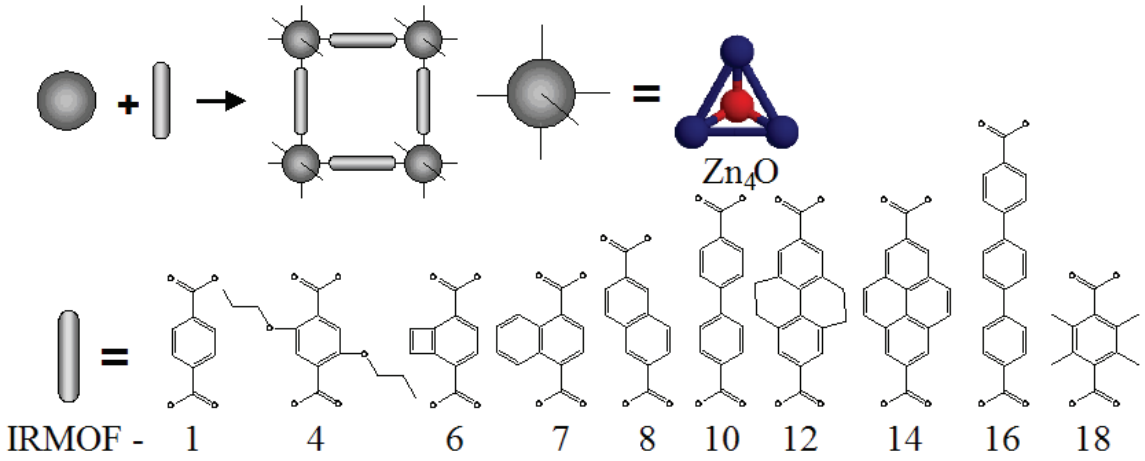


**Figure 1.1: The geometry and building blocks of a series of IRMOFs. (Important properties of these materials can be found in Appendix A).**

The building-block approach has generated much excitement about the possibility to design new porous materials. For example, within the IRMOF family, if one conceives of a new linker molecule, say with a desired chemical functionality, there is a good chance that it can be incorporated into an IRMOF if the required carboxylate groups can be synthesized at the ends and if the linker is fairly rigid[1,2]. However, if MOFs are to be truly designed for particular applications, we need a better understanding of how the key structural features affect adsorption of guest molecules.

a) b)

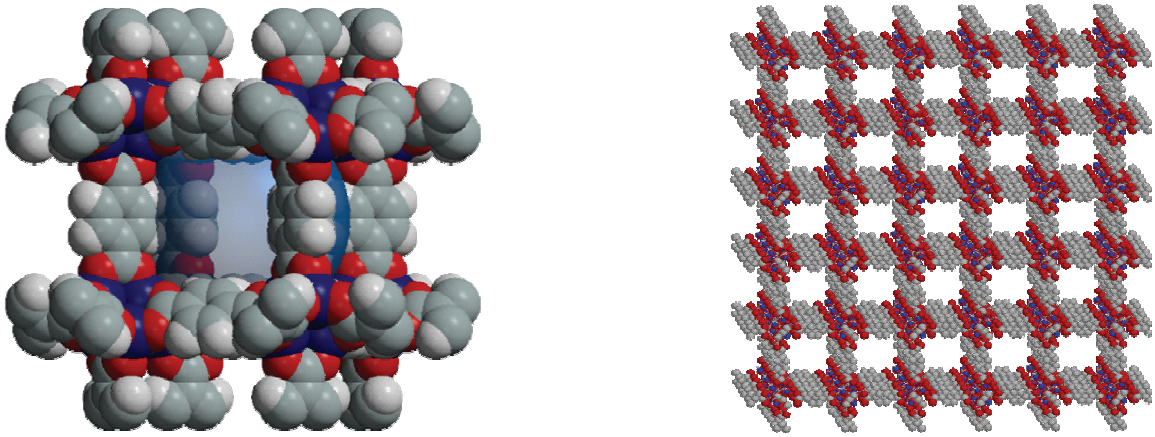

**Figure 1.2(a,b): The unit cell (a) and extended framework (b) for IRMOF-1.**

## *1.2: Material characterization techniques*

Various theories and methods for measuring and calculating three important material characteristics, the heat of adsorption, surface area, and free volume are discussed in the proceeding section.

### *1.2.1: Heats of adsorption*

A number of different 'heats of adsorption' are reported in the literature and can be a source of confusion if precise definitions are either not reported or not properly followed. Care must also be taken in comparing the heat that is measured experimentally and the thermodynamic results from molecular simulation, as the evolved heat is a path dependent process[21-23]. A rigorous discussion of the numerous 'heats of adsorption' would prove too lengthy for this document. There are several sources that provide this discussion, the most comprehensive of which is in the book by Young and Crowell[21]. A helpful overview of the various quantities can be found in the *Adsorption Equilibrium Data Handbook*[24]. Intuitively, one might define the value of the heat of adsorption to simply be the difference in the molar enthalpies of the species in the adsorbed and bulk

gas phases ($H_a$-$H_g$). This value is known as the equilibrium heat of adsorption and is commonly denoted as simply ($\Delta H$)[21,24]. However, this value is not amenable to direct calorimetric or experimental measurement and therefore not often used. The most commonly used heat of adsorption is the isosteric heat of adsorption, as it is commonly calculated using an isostere, which is a plot of the pressure vs. temperature of the adsorption system at constant adsorbate loading. The isosteric heat of adsorption is the difference of the molar enthalpy of the gas phase ($H_g$) and the differential enthalpy in the adsorbed phase ($\hat{H}_s$), which is the partial derivative of the absolute enthalpy of the adsorbed phase with respect to the number of adsorbed moles at constant pressure, temperature, and number of moles of adsorbent. This value is commonly written as $q_{st}$ or $\Delta H^{ads}$. It is referred to as $Q_{st}$ in this document. Furthermore, the use of the generic term, heat of adsorption, refers specifically to the isosteric heat of adsorption, as it is the most widely used value. The differences of the many 'heats of adsorption' are subtle and the names often misused; therefore it is good practice to investigate the specific method used for the calculation or measurement of the heat and not rely on the given nomenclature.

It is important to realize that the heat of adsorption is dependent on the adsorbate loading within the adsorbent, and hence the pressure of the ambient gas phase. This is because the differential enthalpy of the adsorbed phase changes as the number of adsorbed molecules increases, because they begin to adsorb onto sites with less favorable energetics (when considering materials with surface heterogeneities), and the interactions with other adsorbed molecules increases (especially in multilayer and pore filling adsorption). The molar enthalpy of the gas phase can usually be considered independent of pressure, with this approximation becoming exact in the ideal-gas limit[25].

`



Using simulation, the isosteric heat of adsorption can be calculated from the change in the average potential energy of the adsorbed phase $<\mathcal{V}>$, with changing average number of molecules in the system <N>[26,27]:

$$Q_{st} = RT - \left( \frac{\partial < \mathcal{V} >}{\partial < N >} \right)_T n_a \tag{1.1}$$

The derivative is multiplied by Avogadro's number, $n_a$, to obtain the change per mole. The ideal gas constant, R, multiplied by the temperature, T, is the result of assuming an ideal ambient gas phase and constant adsorbed phase volume (with respect to the number of adsorbed moles at constant pressure, temperature, and number of moles of adsorbent)[21]. Without this term, the value would be the negative of what is known as the differential heat of adsorption, yet another possible 'heat of adsorption[21]. It should also be noted that this method assumes no change in kinetic energy of the adsorbate between the gaseous and adsorbed phase[27]. At low loading, where the potential energy contribution from adsorbate-adsorbate interactions is small, and adsorbate molecules are adsorbing on areas of the adsorbent with similar energetics, the derivative can be assumed constant and the average potential energy of the system, $<\mathcal{V}>$, can simply be divided by the number of molecules <N>. The low loading heat of adsorption is generally the value used for comparison between various materials as it provides a clear measure of the strength of the interaction between the adsorbate and adsorbent. Simulations, however, do provide the ability to see how the heat of adsorption changes with loading and can also allow for the separation of the potential energy contribution due to adsorbate-adsorbate interactions and those due to adsorbate-adsorbent interactions. The latter is obviously not possible in experiments.

Experimentally, the heat of adsorption can be obtained in a variety of manners. There is of course direct calorimetry, where the heat is measured directly in either an adiabatic or isothermal calorimeter[28]. Again, the specific method used corresponds to a specific definition of the heat. Since, physisorption heats are generally small, experimental error can be significant in direct calorimetry. A more popular method employed for physisorbed systems is to apply the Clausius-Clapyeron equation to obtain the isosteric heat[25,28]:

$$Q_{st} = -R\frac{d\ln P}{d(1/T)} \tag{1.2}$$

If the natural log of pressure is plotted against the inverse of temperature at constant adsorption, usually a straight line is obtained and the slope of this line can be used in equation (2) to calculate the heat of adsorption. The Clausius-Clapyeron equation makes two assumptions: the ambient gas phase behaves ideally and the molar volume of the adsorbed phase is negligible compared with the molar volume of the gas phase. This technique easily allows for the comparison of heats of adsorption at different loadings.

### *1.2.2: Surface area*

The surface area can be obtained in several ways, either computationally or through experiment. Because of the different manners and assumptions used in the various methods, often it is difficult to compare the values.

The primary method used in this research for calculating surface area is a computational method where a simple Monte Carlo algorithm is used to probe the surface

of an adsorbent material. A spherical probe molecule with diameter equal to the Lennard-Jones sigma parameter for a given adsorbate is used. The probe is randomly inserted thousands of times around the surface of the material's framework atoms, which are also given sizes according to their Lennard-Jones (L-J) parameters. At each insertion the probe is checked for overlap with other atoms. A visual representation of this can be seen in *figure 1.3* where the large yellow circles represent the material atoms and the small blue and red circles represent the probe insertion trials. Ultimately, after a large number of insertions the ratio of accepted insertions over the rejected insertions (i.e. when the probe overlaps nearby atoms) is used to determine the surface area. The surface area is highly dependent on the probe size, and calculating the surface area in this manner provides the amount of area accessible to a given adsorbate molecule. Thus, this value is referred to in this manuscript as the accessible surface area. This surface area algorithm has been modified so that it can also handle the more difficult non-orthorhombic geometry of some MOFs. Materials with non-orthorhombic geometries require a change in the coordinate system in order to efficiently employ periodic boundary conditions. *Appendix B* outlines the method used to transform the coordinate system. Another technique applying a different geometric method and employing a specifically sized probe was popularized by Connolly[29].

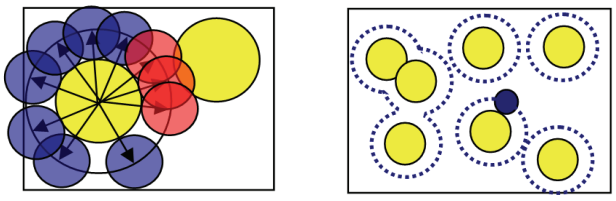

**Figure 1.3: Monte Carlo technique for determining accessible surface area.**

Experimentally, the surface area is generally obtained by applying the Brunauer, Emmit, and Teller (BET) method to nitrogen isotherms[27]. However, calculating the surface area using the BET method directly employs all the assumptions used in the derivation of the BET isotherm model. An even simpler method of experimentally determining the surface area is by using the Langmuir model[27]. Often assumptions in these models are not valid which can cause significant errors in surface area estimation.

### *1.2.3: Free volume*

The free volume can also be calculated computationally using a similar Monte Carlo technique as described for the surface area. In this case however, we probe the entire volume of the material. Also, we do not give the probe a finite size, rather random points within the volume are checked to see if they fall within the framework atoms, which are given their corresponding L-J size, or outside of them. The ratio of points that fall outside of the framework atom over the total number of trial points provides the void fraction of the material. Throughout this discussion, this value is referred to as the free volume or $V_f$.

Experimentally the free volume, which is referred to as the pore volume or $V_g$, to differentiate it from the computationally calculated value, $V_f$, can be calculated using helium gas adsorption. This value can also be determined through simulation in order to mimic the helium calibration used experimentally. The derivation is outlined by Myers[23], and the end result is:

$$V_g = \frac{1}{m}\int \exp(-\mathcal{V}(\mathbf{r})/k_B T)d\mathbf{r} \qquad (1.3)$$

Here, $\mathcal{V}$ is the adsorbate-adsorbent interaction for a single helium atom, **r** is the position of the helium atom, and m is the mass of the adsorbent, $k_B$ is Boltzmann's constant, and T is the temperature. The pore volume, $V_g$, is used to determine excess adsorption values from the absolute adsorption determined in simulations.

One final commonly used experimental method is via the extrapolation of the Dubnin-Radushkevich equation[30] where pore volumes are determined from Ar, $N_2$, or other light gas experimental adsorption data[31-33]. This method is not employed with any of our simulation data, but merits notation here because of its use in experiments[31-33].

### *1.3: Grand canonical Monte Carlo (GCMC) simulations*

The grand canonical Monte Carlo technique is well suited for studying adsorption systems. Since the dynamic behavior of the adsorbed molecules are of little importance in analyzing adsorption, using a molecular dynamics simulation where the momenta of the particles are tracked is unnecessary. Monte Carlo is a technique that explores configuration space randomly. Specifically, we are randomly sampling from the grand canonical ensemble, which is governed by a fixed chemical potential, μ, volume, V, and temperature, T. Grand canonical is the appropriate ensemble for modeling an adsorption system since realistically the adsorbent would be exposed to a gas at a specific pressure which has a constant chemical potential, μ. Further, the condition for adsorption equilibrium is:

$$\mu_a = \mu_g \tag{1.4}$$

Here the subscript, a, is for the adsorbed phase, and subscript, g, is for the gaseous phase. Therefore, given the pressure of the gas and its corresponding chemical potential, one can simulate the adsorbed phase.

The essence behind the Monte Carlo technique is that the double integral in the relevant ensemble partition function, in this case the grand canonical partition function Ξ, can be separated into two integrals, one over the positions, which determines the potential energy of the system, and the other over the momenta of the particles, which provides the kinetic energy of the system. The integral over momenta can be integrated analytically. This allows for the determination of ensemble averages via a numerical integration of the potential energy term. The Monte Carlo method is used for this integration through the generation of numerous configurations of the system. However, if purely random configurations were attempted, many would not be statistically important or representative of the ensemble and therefore would have little impact on the integration. It would be extremely computationally expensive because of the number of random configurations that would be required before the integral would converge to its final value. In order to efficiently derive configurations that make significant contributions to this integral, importance sampling must be invoked. The Metropolis-Hastings method is the tool used for importance sampling which enforces criteria for accepting or rejecting various moves. The set of allowed moves in our adsorption system are molecule translation and rotation, as well as insertion and deletion (as we are sampling the grand canonical ensemble). No other move types are necessary, as the adsorbent atoms are fixed, and adsorbate molecule are represented simply as a united atom or as a rigid molecule. After numerous moves, the system eventually reaches equilibrium and the

energy, along with the adsorption loadings converges to the equilibrium value (although there is still some fluctuation).

The potential energy function $\mathcal{V}(\mathbf{r}^N)$ is calculated by summing up the pair wise interaction energies of particles comprising the system. These pair wise interaction energies are determined from a force field model that is assumed to describe them. Dispersion interactions are most commonly estimated using a Lennard-Jones 6-12 potential[34], and this is what is employed for all GCMC simulations in the proposed research. Coloumbic interactions can also be taken into account, although they are not always necessary for an accurate description of the interactions. When used, these are calculated using a point-charge electrostatic model. Bond stretching, angle bending and torsions are not considered in the force-field models used in this research as these simple molecules are assumed rigid.

### *1.4: Quantum chemical calculations*

Quantum chemical calculations are also employed to study the various adsorption systems. The software package Gaussian 03[35] is used for all calculations. The primary purpose of quantum calculations is to determine the limiting heat of adsorption for various adsorbate-adsorbent combinations. The geometry optimizations also provide some insight as to where the preferential adsorption sites on various materials may be. Only small representative sections or clusters of the material are used as opposed to the full periodic structure since high level calculations are necessary to model the dispersion interactions dominant in largely non-polar molecules such as $H_2$ and $N_2$. This is deemed the cluster approximation.

Computational quantum chemistry allows for a numerical estimation of solutions to the Schrödinger equation[34]:

$$\mathcal{H}\Psi = E\Psi \tag{1.5}$$

Here $\mathcal{H}$ is the well known Hamiltonian operator, which operates on $\Psi$, the wave function of a particle or system of particles. Essentially the wave function characterizes the particle's motion. It can be used to provide the probability of the particle or system being in a certain position or state, and from the wave function various properties of the particle or system can be derived[34].

The Schrödinger equation (1.5) cannot be solved exactly for a system containing more than one electron. However, the wave function for a multi-electron system (e.g. atom or molecule) can be approximated by using single electron atomic orbitals[34]. These single electron orbitals are represented by basis functions. While the functional form of the basis function is given as an input, the coefficients of the basis function are optimized so that the energy of the electron system is minimized, according to the variational principle. The other important element for the solution of the Schrödinger equation is how exactly these basis functions are used to calculate the energy. The two general methods used for energy calculations are known as Hartree-Fock (HF) and Density Functional Theory (DFT). HF uses the basis functions to determine an approximate wave function for the system. This approximate wave function is then operated on by the exact Hamiltonian operator to find the energy. DFT on the other hand uses the basis functions to calculate an electron density. This electron density is then used in an approximate manner to calculate the energy. Thus, the situation is considered reversed and an exact wave function is determined and operated on by an approximate Hamiltonian.

In order to calculate a 'heat of adsorption' from quantum chemical calculations, one must determine the energy of the lone gaseous adsorbate molecule and the bare adsorbent cluster that has been chosen to represent the material. Subtracting these from the energy of the combined adsorbate molecule and adsorbent cluster yields the binding energy of adsorption, $E_{ads}$:

$$E_{ads} = E_{cluster+molecule} - E_{cluster} - E_{molecule} \tag{1.6}$$

This electronic binding energy is used as an estimate specifically for the isosteric heat of adsorption at low loading or limiting heat of adsorption in this study.

Basis set superposition error (BSSE) is caused by having a larger basis set for the combined adsorbate-adsorbent system than for the two species alone; simply because the former system has more electrons. This is corrected for by adding what are known as ghost atoms to the system; ghost atoms are atoms without electrons or nuclei but still carrying their corresponding basis sets. BSSE values are determined for only some of the binding energies determined so as to get an estimate of the magnitude of this contribution

The energy values determined through quantum chemical calculations are only the electronic portion of the total molecular energy at 0 K.

$$E_{tot} = E_{electronic} + E_{vibrational} + E_{rotational} + E_{translational} \tag{1.7}$$

It should be mentioned that to determine the total binding energy one must evaluate the difference of vibrational, rotational, and translational contributions between the adsorbed and separated species at the temperature of interest. For the gaseous molecules and the cluster it can be estimated that there is no change in translational and rotational energy if all respective modes are fully accessible in accordance with the equipartition theorem and this is generally the case at room temperature. However, the vibrational contribution of

the species may be important. For the purpose of this study however, we only the electronic portion of the binding energy is investigated.

### *1.5: Hydrogen storage review*

There are a number of options for storing hydrogen for use in mobile applications. Currently, the DOE has set 2010 hydrogen storage targets at 6 wt. % and 45 g $H_2$/L storage vessel, and 2015 targets at 9 wt. % and 81 g $H_2$/L storage vessel[36]. These targets must be met at pressures and temperatures that allow for an economically feasible storage system. Current methods of hydrogen storage include compressed hydrogen, liquid hydrogen, chemisorbed hydrogen, and physisorbed hydrogen. *Table 1.1* below lists the gravimetric and volumetric densities currently obtainable via these various methods as well as the required temperatures and pressures.

**Table 1.1: Currently obtained gravimetric and volumetric densities of hydrogen for various materials[36-38].**

| Storage method: | $\rho_g$ (wt. %) | $\rho_v$ (g $H_2$/mL) | T ($^oC$) | P (bar) |
|---|---|---|---|---|
| **DOE 2010 targets** | 6 | 45 | -30 to 85 | 100 (for adsorbed $H_2$) |
| **DOE 2015 targets** | 9 | 81 | -40 to 85 | 100 (for adsorbed $H_2$) |
| **compressed hydrogen** | 13 | <40 | 25 | 800 |
| **liquid hydrogen** | n/a | 70.8 | -252 | 1 |
| **chemisorbed hydrogen (e.g. metal hydrides)** | ~2 | 150 | 25 | 1 |
| **physisorbed hydrogen (in various materials)** | 11 (absolute) | 20 | -196 | 70 |

The numbers contained in *table 1.1* seem to favor chemisorbed hydrogen as the hydrogen can obtain a volumetric density greater than that of hydrogen in its compressed or liquid form, and doesn't require high pressures or a loss of hydrogen due to boil off

that is experienced in compressed or liquid hydrogen storage. The gravimetric density seems to miss the DOE required values. However new complex hydrides containing light metals such as lithium, magnesium, boron, or aluminum have been reported to obtain gravimetric densities as high as 18 wt. %[37]. While metal hydrides seem to be a viable option, meeting the DOE requirements at room temperature and atmospheric pressure, approximately 25 % of the higher heating value of the hydrogen is required for the endothermic desorption of the hydrogen[37]. Thus only 75% of the $H_2$ energy stored in the material can be realized and this does not meet DOE's efficiency guidelines[36]. The large inefficiency is due to the high heat of adsorption. This leads to the investigation of materials that physisorb hydrogen, which provides for a lesser heat of adsorption. MOFs have been found to have high gravimetric hydrogen uptake at 77K[38].

In addition there are claims that carbonaceous materials such as a nanostructured graphite can be designed to store nearly 8% wt. $H_2$ [39,40], as well arguments based on surface area correlations that a theoretical maximum of 3% wt. $H_2$ can be obtained at 77 K in SWNTs (single wall carbon nanotubes) that have a surface area of 1315 $m^2/g$ [37].

The second and third chapters of this dissertation concentrate on the physisorption of hydrogen in MOFs. There is considerable debate as to whether acceptable densities of hydrogen at moderate pressures can be obtained through physisorption[15,37,39-41]. The aforementioned chapters investigate this possibility and determine the required material properties to obtain acceptable densities.

# Chapter 2: Effects of Surface Area, Free Volume, and Heat of Adsorption on Hydrogen Uptake in Metal-Organic Frameworks


## *Abstract*

Grand canonical Monte Carlo simulations were performed to predict adsorption isotherms for hydrogen in a series of 10 isoreticular metal-organic frameworks (IRMOFs). The results show acceptable agreement with the limited experimental results from the literature. The effects of surface area, free volume, and heat of adsorption on hydrogen uptake were investigated by performing simulations over a wide range of pressures on this set of materials, which all have the same framework topology and surface chemistry but varying pore sizes. The results reveal the existence of three adsorption regimes: at low pressure (loading), hydrogen uptake correlates with the heat of adsorption; at intermediate pressure, uptake correlates with the surface area; and at the highest pressures, uptake correlates with the free volume. The accessible surface area and free volume, calculated from the crystal structures, were also used to estimate the potential of these materials to meet gravimetric and volumetric targets for hydrogen storage in IRMOFs.


## *2.1: Introduction*

Metal-organic frameworks are a new class of microporous materials with potential applications in adsorption separations, catalysis, and gas storage[5,7-9]. They are synthesized in a building block approach from metal or metal oxide vertices interconnected by organic linkers. An example of one class of MOFs is shown in *figure 2.1*. The materials illustrated in *figure 2.1* were discovered by Yaghi and co-workers and are known as isoreticular metal-organic frameworks or IRMOFs[15-17]. They feature oxide-

centered $Zn_4O$ tetrahedra each connected by six dicarboxylate linkers, resulting in extended 3-dimensional cubic networks having very high porosity. A variety of linker molecules can be used to create an entire family of materials having different pore sizes and containing different chemical functionalities within the linkers but all with the same basic framework topology. In addition, different metal corners and different linkage chemistries can yield a wide variety of other framework topologies[3,7,13,18,19].

The building-block approach has generated much excitement about the possibility to design new nanoporous materials. For example, within the IRMOF family, if one conceives of a new linker molecule, say with a desired chemical functionality, there is a good chance that it can be incorporated into an IRMOF if the required carboxylate groups can be synthesized at the ends and if the linker is fairly rigid[1,2]. However, if MOFs are to be truly designed for particular applications, we need a better understanding of how the key structural features affect adsorption of guest molecules. This paper will focus on gas storage applications, where the adsorption isotherm is of particular importance, but the same considerations are clearly applicable to adsorption separations with MOFs.

Alternative fuels such as hydrogen and natural gas have been studied extensively for their potential use in next-generation vehicles. A key issue in implementing alternative fuels in vehicles is how to store the fuel safely and cost efficiently, which requires a way to keep the fuel at high densities at reasonable pressures. MOFs have been investigated for use in this application for their ability to adsorb both methane[17,42,43], the primary component of natural gas, and hydrogen[12,13,15,44-46].

To maximize gas storage by physisorption, much attention has focused on the role of surface area[13,41,42,45,47-50]. Some of the MOFs synthesized to date have incredibly high

surface areas. For example MOF-177 has a surface area of 4,500 $m^2\ g^{-1}$ estimated from nitrogen adsorption[47]. This is much higher than the zeolite with the highest surface area, namely zeolite Y at 904 $m^2\ g^{-1}$, and even higher than activated carbons, which have surface areas around 2000 $m^2\ g^{-1}$ [47]. Adsorption is primarily due to interactions of guest molecules with atoms of the adsorbent walls, so it seems logical that a high surface area – either per unit mass or per unit volume – should be desirable for high uptake. Düren et al.[42] examined a variety of microporous materials, including MOFs, zeolites, and carbon nanotubes, using atomistic grand canonical Monte Carlo (GCMC) simulations and found that adsorption of methane at 35 bar and 298 K does correlate with the surface area. They found, however, that the free volume and the strength of adsorbent/guest interactions also play a role and that these factors are interlinked in a non-trivial way.

The development of simple heuristics to avoid the need for full GCMC simulations or adsorption experiments would be helpful to researchers synthesizing new materials. In this paper, we revisit the role of surface area, free volume, and adsorbent/guest energetics in determining adsorption of small molecules in microporous materials. In contrast to the work of Düren et al.[42], we consider a series of materials all having the same framework topology and the same "wall" chemistry. We used GCMC simulations to predict adsorption of hydrogen and methane in the ten IRMOFs shown in *figure 2.1*. In addition, rather than focusing just on the adsorption at a single pressure, we considered the full range of loadings from very dilute to complete pore filling.

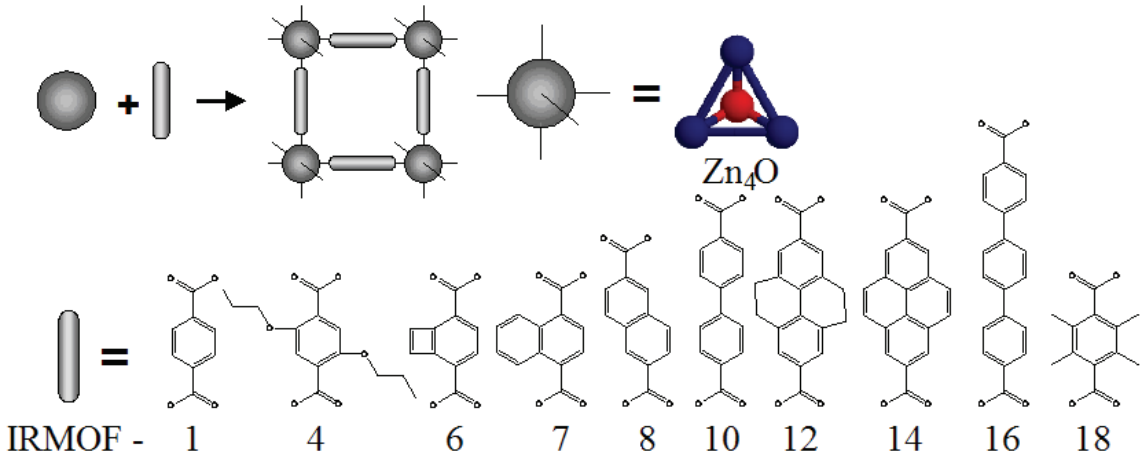


**Figure 2.1: The geometry and building blocks of IRMOF materials studied in chapter 2.**

### *2.2: Simulation methods*

Hydrogen adsorption in the IRMOFs was simulated with GCMC[51,52] using our multi-purpose simulation code Music[53]. Gas-phase fugacities for hydrogen were calculated using the Peng-Robinson equation of state. A united-atom model was used for the guest molecules, and an atomistic model was used for the porous frameworks, which were considered rigid with atoms at the positions reported from crystallography[15-17]. All inter-atomic interactions were modeled with a standard Lennard-Jones potential. The Lennard-Jones parameters for the hydrogen molecule are known from experimental work[54] and have been used in similar simulation studies by Dakrim[55], whereas the parameters for the framework atoms were taken from the DRIEDING force field[56]. Lorentz-Berthelot mixing rules were employed to calculate sorbate/framework parameters. Interactions beyond 12.8 Å were neglected. The Lennard-Jones parameters can be found in *table C.1* in *appendix C*. For each point on the isotherm, one million Monte Carlo steps were performed. A Monte Carlo step consisted of one of the following: insertion of a new

molecule, deletion of an existing molecule, or translation of an existing molecule. Rotation and intramolecular moves were unnecessary as the $H_2$ molecule was represented as a single sphere (united atom model). The first 600,000 steps were used for equilibration, and the last 400,000 steps were used to calculate the ensemble averages. Adsorption isotherms were calculated for hydrogen in the ten IRMOFs shown in *figure 2.1* at 77 K and pressures up to 120 bar.

Molecular simulation predicts the absolute number of sorbate molecules within the framework material at the given gas-phase conditions, whereas experimental measurements yield the excess amount adsorbed. The excess adsorption is the amount of sorbate within the adsorbent above and beyond what is found in the ambient gas phase. The conversion from absolute to excess sorption can be performed as follows:

$$N_{ex} = N_{abs} - V_g \rho_g \tag{2.1}$$

The excess adsorption, $N_{ex}$, is determined from the absolute adsorption, $N_{abs}$, by subtracting the pore volume of the adsorbent, $V_g$, calculated as described by Myers and Monson[23], multiplied by the density of the ambient gas phase, $\rho_g$, calculated using the Peng-Robinson equation of state.

The available surface area and free volume were calculated for all IRMOFs using a numerical Monte Carlo integration technique. The surface area was calculated by "rolling" a probe molecule with a diameter equal to the Lennard-Jones sigma parameter for $H_2$ ($\sigma$ = 2.958 Å) over the framework surface. Surface area is highly dependent on the probe size used for measurement, and calculating the surface area in this manner provides the amount of area accessible to hydrogen molecules. The probe was randomly inserted around the surface of each framework atom in turn, which were also given sizes

equal to their Lennard-Jones sigma parameters, and tested for overlap. The fraction of probes that did not overlap with other framework atoms was used to calculate the available surface area. The free volume, $V_f$ (different than $V_g$ above), was calculated using a similar method of trial insertions within the entire volume of the unit cell. A probe size of 0 Å was used to enable us to determine the total free volume in the unit cell. Probing the material in this manner enables us to determine the volume of the simulation cell that is not occupied by framework atoms. This method of calculating free volume is based solely on the system geometry, whereas the pore volume, $V_g$, is based on a thermodynamic definition. The isosteric heat of adsorption, $Q_{st}$, was calculated at low loadings, between 0 and 0.5 bar, as described by Snurr et al.[26] The isosteric heat was found to be approximately constant within this pressure range.

### *2.3: Results and discussion*

Simulations of hydrogen adsorption were performed at 77 K to compare against experimental data from the literature. As *figure 2.2* shows, the simulation results are in reasonable agreement with the experimental data of Rowsell et al.[15] for IRMOF-1 and 8, but the concavity of the adsorption isotherms deviates somewhat. Agreement for IRMOF-18 (not shown) is not as good, as simulation overestimates adsorption by about a factor of 2 throughout the pressure range. Several other research groups have reported similar results recently with somewhat different force fields[57-59]. Yang and Zhong[58] obtained better results for these three MOFs by fitting the force field parameters. Garberoglio[59] discuss the effects of changing the force field, for example by adding a

Coulomb potential. We did not attempt to improve the force field, but the results are reasonably good given the simplicity of the model[60-63].

Most of the materials are predicted to have very similar heats of adsorption at low loadings, between 4.5 and 5.5 kJ/mol. These values agree well with numbers reported in the literature from experiment[61,63] and quantum chemical calculations[44,57,64,65]. IRMOF-4 has a noticeably higher heat of adsorption at low loading than the other materials (7.2 kJ/mol) due to the small pore size and the high number of framework atoms resulting from the alkyl chains.

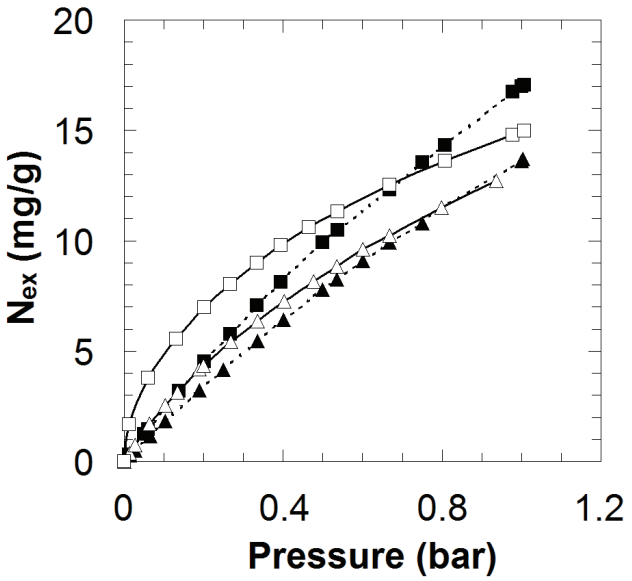


**Figure 2.2: Simulated and experimental adsorption isotherms for IRMOF-1 and IRMOF-8 at 77 K. ▲- IRMOF-1 simulation, △- IRMOF-1 experiment, ■- IRMOF-8 simulation, □- IRMOF-8 experiment. The lines were added to guide the eye.**

Absolute adsorption isotherms for the ten IRMOFs considered are presented in *figure 2.3* in terms of gravimetric uptake. At low pressures (*figure 2.3a*), IRMOFs-4 and -7 show the highest uptake of hydrogen, but at pressures above about 15 bar (*figure 2.3b*), IRMOF-16 displays the largest uptake per gram of sorbent. The qualitative reason for this crossing of the isotherms is well understood from the adsorption literature[27,66]. At

low loadings, materials with the strongest enthalpic interactions with sorbed molecules show the highest levels of adsorption. These tend to be materials with narrow pores, such as IRMOFs-1, 4, 6, and 7, because small pores increase the interaction between hydrogen and the framework[67,68]. However, materials with narrow pores also have the highest framework densities (see *appendix A*) and thus the lowest amounts of free void space per gram of material. Therefore, at the highest pressures when the pores are nearly filled, the materials with the largest free volumes have more room for guest molecules and consequently show the highest uptake.

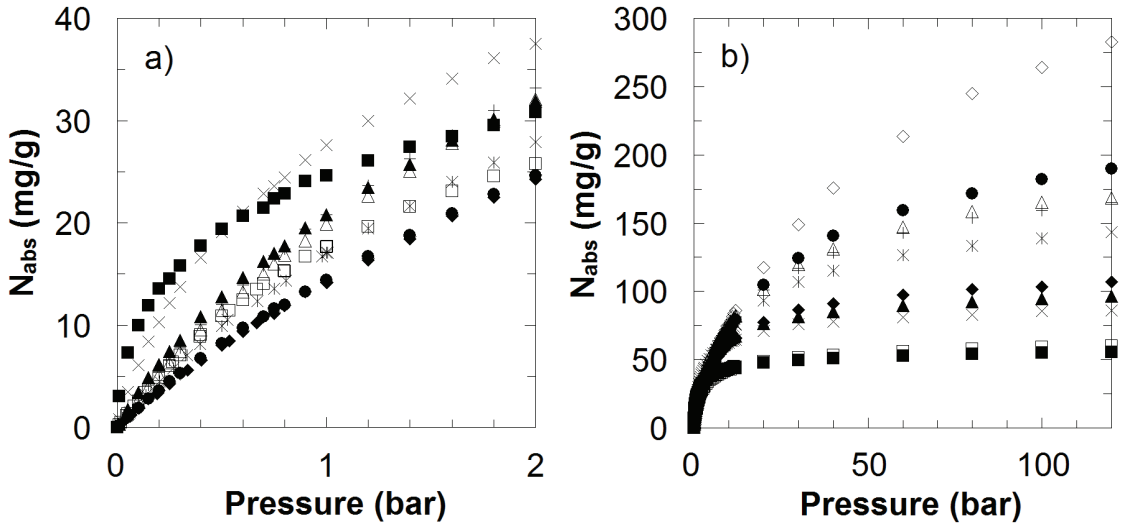


**Figure 2.3: a) Low pressure simulation adsorption isotherms at 77 K. b) High pressure simulation adsorption isotherms at 77 K. ◆- IRMOF-1, ■- IRMOF-4, ▲- IRMOF-6, ×- IRMOF-7, ✳- IRMOF-8, ●- IRMOF-10, ┼- IRMOF-12, △- IRMOF-14, ◇- IRMOF-16, □- IRMOF-18.**

To make this idea more quantitative, we plotted the amount adsorbed at low pressure (0.1 bar) against the isosteric heat of adsorption and the amount adsorbed at high pressure (120 bar) against the free volume of the frameworks. The results, presented in *figures 2.4a and 2.4c*, show that there are excellent correlations in both cases. Between these two limiting cases, one might expect that the surface area would be important. In *figure*

*2.4b*, the amount of hydrogen adsorbed at an intermediate pressure (30 bar) is plotted as a function of the surface area per gram. An excellent correlation is also found in this case.

It appears that three different adsorption regimes can be identified. At low pressure, the amount adsorbed correlates with the heat of adsorption. At intermediate pressures, the amount adsorbed correlates with the surface area. And at the highest pressures, the amount adsorbed correlates with the free volume. *Figure 2.4* shows these correlations using a gravimetric basis, but the correlations hold on a volumetric basis as well. This simply requires dividing the specific surface area, the specific free volume, and the amount adsorbed per gram by the framework density. Furthermore, the correlations also hold for the excess amount adsorbed, although the correlations are slightly weaker. Absolute adsorption was used here because it is more closely tied to the physics underlying the correlations.

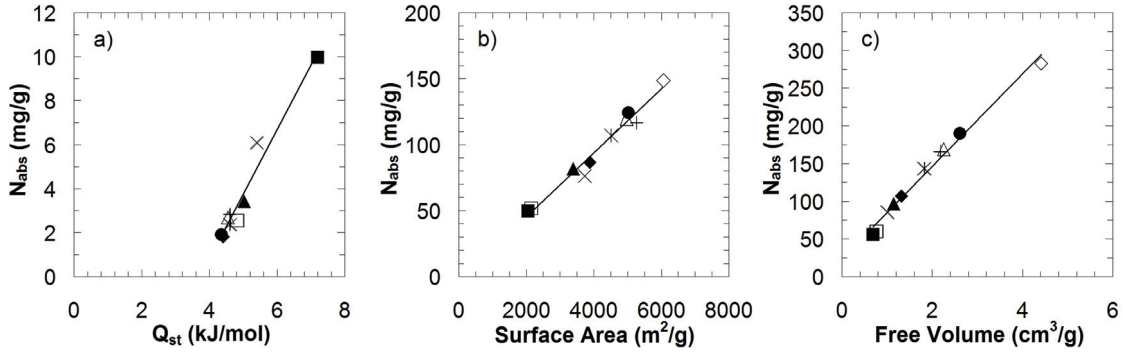


**Figure 2.4: a) Amount adsorbed at 0.1 bar vs. isosteric heat of adsorption. b) Amount adsorbed at 30 bar vs. accessible surface area. c) Amount adsorbed at 120 bar vs. free volume. The symbols are the same as in figure 2.3.**

As a further demonstration that these three regimes hold, we tested for correlation of the amount adsorbed at each of the three pressures with all three properties (heat of adsorption, surface area, and free volume). For example, in *figure 2.5*, the amount

adsorbed at 0.1 bar is plotted against the surface area, and it can be seen that there is no correlation. Similarly there is no correlation of the amount adsorbed at 0.1 bar with the free volume. A summary of these determinations is given in *figure 2.6*, which shows the coefficient of multiple determination ($R^2$) for each of the nine cases. $R^2$ represents the fraction of variability in the observations accounted for by the first order linear regression equation used, that is, the fraction of the total variability in the data that is captured by the regression equation, the remainder of which is considered random noise. The $R^2$ values for adsorption vs. heat of adsorption in *figure 2.6* clearly indicate a linear regression is not adequate to quantify adsorption at 30 and 120 bar. Similarly $R^2$ values for adsorption vs. surface area indicate a linear regression is best at intermediate pressures. Finally, the $R^2$ values for adsorption vs. free volume show that as pressure increases the quality of regression improves. There exists a loose correlation between surface area and free volume for this series of materials ($R^2 = 0.87$), and this is the cause of the high $R^2$ values for the surface area correlation at 120 bar and the free volume correlation at 30 bar. The correlations in *figure 2.4* all pass a significance of regression test[69] with 99.99% confidence or greater, and the residuals have been found to be normally distributed uncorrelated random variables with a mean of zero and constant variance.

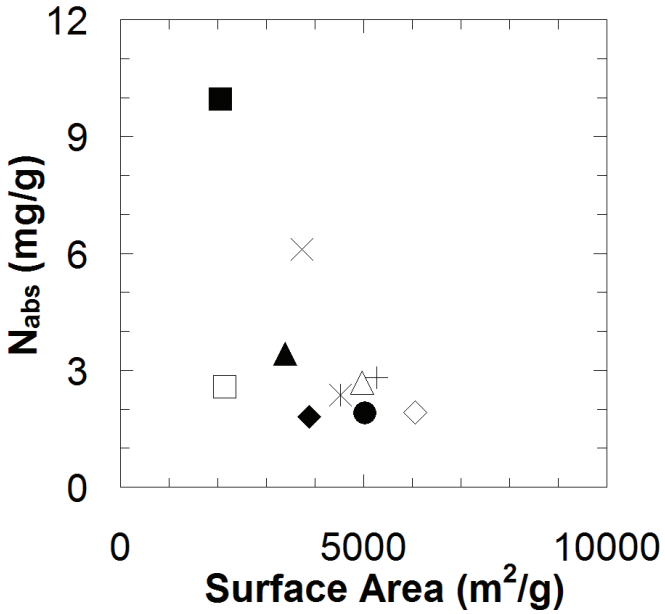


**Figure 2.5: Amount adsorbed at 0.1 bar vs. accessible surface area. There is no correlation. The symbols are the same as in figure 2.3.**

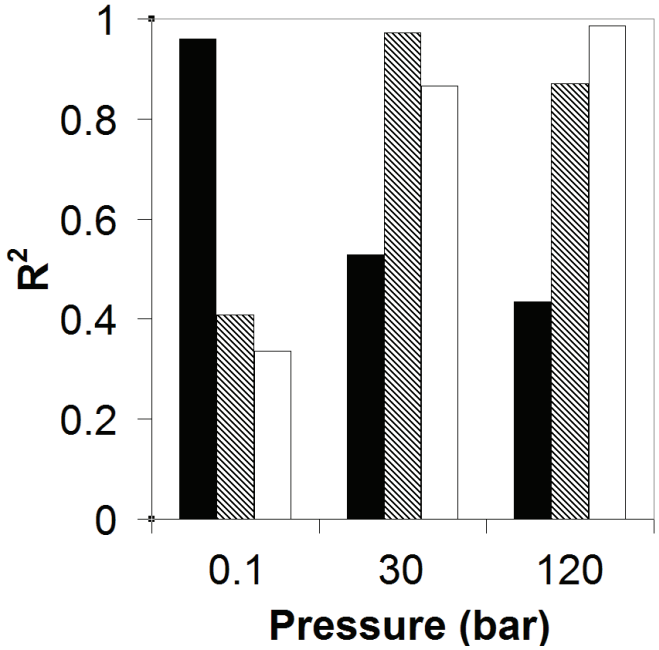


**Figure 2.6: Coefficient of multiple determination (R2) for correlation of amount adsorbed with: ■- heat of adsorption, ▤- surface area, □- free volume.**

Visualizations of molecular siting within IRMOF-10 are shown in *figure 2.7* in the three different pressure/loading regimes. *Figure 2.7a* shows that at low pressure hydrogen molecules are mostly near the zinc corners, which are the most favorable

energetic adsorption regions due to the high concentration of framework atoms. This has also been reported by other simulation studies,[57,58,70] and inelastic neutron scattering experiments have also found that hydrogen tends to adsorb near the zinc corners[71]. *Figure 2.7b* shows that at 30 bar, molecules adsorb preferentially in the corners and along the linker molecules, with fewer molecules in the centers of the cavities. *Figure 2.7c* displays the limiting adsorption behavior where hydrogen fills the majority of the void regions of the material.

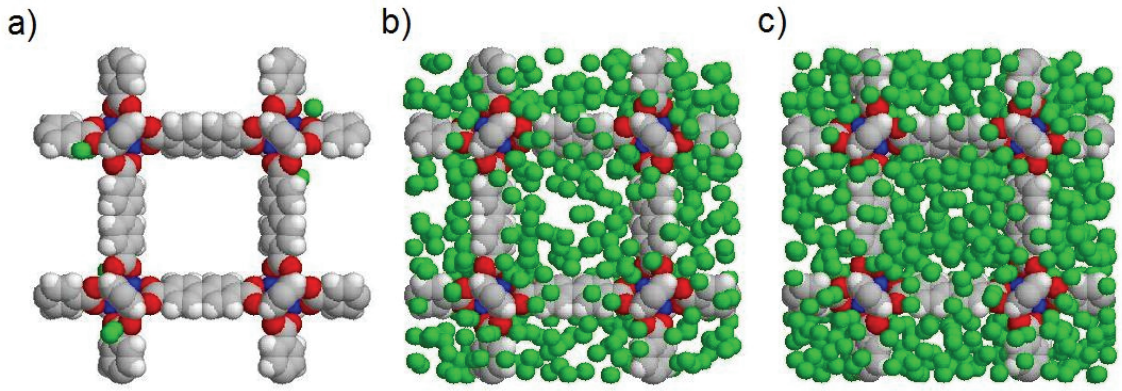


**Figure 2.7: Snapshots of hydrogen adsorption in IRMOF-10. a) 0.1 bar b) 30 bar c) 120 bar.**

The three adsorption regimes were also found for methane in IRMOFs at 298 K using pressures of 0.1 bar, 50 bar, and 200 bar[72]. Presumably the existence of these three regimes is a general result that holds for other adsorbates and adsorbents because the fundamental physics of adsorption thermodynamics is the same. It should be noted that the transitions between regimes do not occur at distinct pressures; rather they occur gradually as pressure, and hence the loading in the pores, is increased. In addition, the specific pressures corresponding to low, intermediate, and high pressures will be different for different systems and also for different temperatures. This is because the correlations are a result of the extent of loading rather than tied directly to any pressure values.

The discovery of the excellent correlations in *figure 2.4* was mainly made possible by the recent synthesis of these materials that all have the same framework topology, constituent atom types, and wall chemistry. When Düren et al.[42] performed a similar analysis for methane adsorption in IRMOFs, carbon nanotubes, and zeolites, they found a correlation of the amount adsorbed at 35 bar with the surface area, but the correlation was a band of data points rather than the single line seen in *figure 2.4b*.

The calculated surface areas and free volumes allow for a simple estimate of an upper bound on the adsorption capacity, and we used this to examine the potential of these 10 IRMOFs to meet the targets for hydrogen storage set by the U.S. Department of Energy[36]. The 2010 targets are 6 wt. % and 45 g/L, and the 2015 targets are 9 wt. % and 81 g/L. First, we considered the surface area. In a simple "back-of-the-envelope" calculation, we took the accessible surface area of each material and asked what loading would be possible if monolayer adsorption could be achieved. Two different packing models of molecules were explored: a randomly packed monolayer[73] with a coverage fraction of 0.55 and a hexagonally packed monolayer with a coverage fraction of 0.91. Hydrogen molecules were assumed to be spherical with a diameter of 2.958 Å. The accessible surface area per gram of sorbent was multiplied by the coverage fraction and then divided by the cross-sectional area of a hydrogen molecule to estimate the potential gravimetric hydrogen uptake, naively assuming monolayer adsorption. The results, presented in columns 4 and 5 of t*able 2.1*, indicate that the upper bound for hydrogen uptake in these IRMOF materials are above the DOE gravimetric targets of 6 or 9 wt. %. In a similar simple calculation, we took the free volume per gram for each material and calculated the gravimetric uptake of hydrogen if the void space could be filled with hydrogen at either

its liquid or solid density. These results, shown in columns 6 and 7 of *table 2.1* are also encouraging.

*Table 2.2* shows analogous results on a volumetric basis. The results are mostly above the DOE 2010 volumetric target of 45 g/L, but the 2015 target (81 g/L) may be difficult to meet. This is, perhaps, not surprising, given that solid hydrogen (at 19.5 K and 1 atm) has a density of 88 g/L, which is only slightly higher than the 2015 target.

**Table 2.1: Potential gravimetric hydrogen uptake based on accessible surface area and free volume[74].**

| Material | Accessible Surface Area for $H_2$ ($m^2/g$) | Free Volume ($cm^3/g$) | $H_2$ Uptake (wt. %) assuming $\phi$=0.55 | $H_2$ Uptake (wt. %) assuming $\phi$=0.91 | $H_2$ Uptake (wt. %) assuming liquid $H_2$ within free volume | $H_2$ Uptake (wt. %) assuming solid $H_2$ within free volume |
|---|---|---|---|---|---|---|
| IRMOF-1 | 3882 | 1.315 | 10.4 | 17.2 | 9.3 | 11.6 |
| IRMOF-4 | 2056 | 0.694 | 5.5 | 9.1 | 4.9 | 6.1 |
| IRMOF-6 | 3395 | 1.142 | 9.1 | 15.0 | 8.1 | 10.0 |
| IRMOF-7 | 3730 | 1.013 | 10.0 | 16.5 | 7.2 | 8.9 |
| IRMOF-8 | 4518 | 1.834 | 12.1 | 20.0 | 13.0 | 16.1 |
| IRMOF-10 | 5029 | 2.615 | 13.5 | 22.3 | 18.6 | 23.0 |
| IRMOF-12 | 5267 | 2.188 | 14.1 | 23.3 | 15.5 | 19.3 |
| IRMOF-14 | 4964 | 2.259 | 13.3 | 22.0 | 16.0 | 19.9 |
| IRMOF-15 | 6075 | 1.962 | 16.3 | 26.9 | 13.9 | 17.3 |
| IRMOF-16 | 6055 | 4.413 | 16.2 | 26.8 | 31.3 | 38.8 |
| IRMOF-18 | 2148 | 0.780 | 5.8 | 9.5 | 5.5 | 6.9 |

$\phi$ is the coverage fraction; the liquid $H_2$ density at 20.3K and 1 atm is 70.96 g/L; the solid $H_2$ density at 13.8K and 1 atm is 88 g/L[75,76].

**Table 2.2: Potential volumetric hydrogen uptake based on accessible surface area and free volume[74].**

| Material | Accessible Surface Area for $H_2$ ($m^2/cm^3$) | Void Fraction | $H_2$ Uptake (g/L) assuming $\phi$=0.55 | $H_2$ Uptake (g/L) assuming $\phi$=0.91 | $H_2$ Uptake (g/L) assuming liquid $H_2$ within free volume | $H_2$ Uptake (g/L) assuming solid $H_2$ within free volume |
|---|---|---|---|---|---|---|
| IRMOF-1 | 2290 | 0.780 | 61.4 | 101.5 | 55.3 | 68.6 |
| IRMOF-4 | 1770 | 0.597 | 47.4 | 78.5 | 42.4 | 52.6 |
| IRMOF-6 | 2207 | 0.745 | 59.1 | 97.8 | 52.9 | 65.6 |
| IRMOF-7 | 2648 | 0.718 | 71.0 | 117.4 | 51.0 | 63.2 |
| IRMOF-8 | 2024 | 0.822 | 54.2 | 89.7 | 58.3 | 72.3 |
| IRMOF-10 | 1660 | 0.860 | 44.5 | 73.6 | 61.0 | 75.7 |
| IRMOF-12 | 2001 | 0.832 | 53.6 | 88.7 | 59.1 | 73.2 |
| IRMOF-14 | 1837 | 0.843 | 49.2 | 81.4 | 59.8 | 74.2 |
| IRMOF-15 | 2509 | 0.808 | 67.2 | 111.2 | 57.3 | 71.1 |
| IRMOF-16 | 1241 | 0.905 | 33.3 | 55.0 | 64.2 | 79.6 |
| IRMOF-18 | 1837 | 0.667 | 49.2 | 81.4 | 47.3 | 58.7 |

$\phi$ is the coverage fraction; the liquid $H_2$ density at 20.3K and 1 atm is 70.96 g/L; the solid $H_2$ density at 13.8K and 1 atm is 88 g/L[75,76].

It should be kept in mind that the results in *tables 2.1 and 2.2* do not come from GCMC simulations, but only from the accessible surface area and free volume calculated from the crystal structures, along with an assumed monolayer coverage or an assumed density in the pores. The results in *tables 2.1 and 2.2* do not indicate what pressures would be required to achieve these loadings at room temperature. The assumption of uniform monolayer coverage or uniform filling of the void space is an upper limit on adsorption, so these simple calculations are a potentially valuable screening tool that could be applied to new materials very quickly.

### *2.4: Conclusions*

Molecular simulations of hydrogen adsorption isotherms in IRMOF materials revealed the existence of three distinct regimes. Comparing different materials, the amount adsorbed can be correlated with the heat of adsorption at low pressures

(loadings), the surface area at intermediate pressures, and the free volume at high pressures. Because the materials studied all have the same framework topology and surface chemistry, the transitions between the regimes occurred at similar pressures and this provided for the excellent correlations. For materials of differing topologies and surface chemistry, the correlations will not be as good[42], but the surface area and free volume are still clearly important characteristics in evaluating any potential hydrogen storage adsorbent.

Using the surface areas and free volumes calculated from the crystal structures, we made simple estimates of the potential of selected IRMOFs for hydrogen storage by assuming either monolayer coverage on the entire surface area or complete filling of the free volume with the density of liquid or solid hydrogen. The results indicate that IRMOFs are promising materials for meeting established hydrogen storage targets due to their very high surface areas and free volumes. A remaining challenge is to design new materials with increased heats of adsorption so that the desired densities of hydrogen can be concentrated within these materials at reasonable temperatures and pressures.

# Chapter 3: Design Requirements for Metal-Organic Frameworks as Hydrogen Storage Materials


## *Abstract*

Storing an acceptable density of hydrogen in porous materials by physisorption at room temperature and reasonable pressures is a challenging problem. Metal-organic frameworks (MOFs) are a new class of nanoporous materials that have shown early promise for meeting this goal. They have extremely large specific surface areas, but the heats of adsorption to date are too low to provide significant storage at room temperature. In this work, molecular simulations are used to provide guidelines for the design of MOFs for hydrogen storage. To learn how much the heat of adsorption must be increased to meet current targets, we artificially increase the hydrogen/MOF Lennard-Jones attraction. The correlation of the amount of hydrogen adsorbed with the heat of adsorption, the surface area, and the free volume is revisited. We also review the distinction between excess and absolute adsorption and show that comparing the density of hydrogen within the free volume of materials provides useful insight. The simulation results yield a graph showing the required heats of adsorption as a function of the free volume to meet gravimetric and volumetric storage targets at room temperature and 120 bar.


## *3.1: Introduction*

Metal-organic frameworks (MOFs) are a new, actively studied class of microporous materials that have shown promising results in adsorption separations, catalysis, and gas storage.[5,7-9] Several studies have concentrated on their use for on-board hydrogen storage,

but experimental studies to date have only reported useful uptake at cryogenic temperatures. MOFs are composed of metal or metal oxide vertexes that are connected by organic linker molecules containing functional groups that coordinate with the metal corners. The precise coordination geometry between the organic linkers and metal corners leads to porous materials that are highly ordered and periodic. Furthermore, this so-called reticular synthesis allows for chemical tailoring of materials to have specific chemical functionalities, pore sizes, and topologies[1,7]. In order to design new materials for specific applications, it is necessary to know the relationships between material characteristics and adsorption performance.

The safe and efficient storage of hydrogen, used for example in the on-board storage of next generation fuel-cell vehicles, remains a challenge. A wide variety of storage methods have been considered, including high pressure containers, liquid hydrogen, metal hydrides, and physisorption in porous materials[37,39-41]. Many of these options are energy intensive and cost prohibitive. The physisorption of hydrogen remains an attractive alternative because it does not require the extensive investment of energy required to pressurize or liquefy hydrogen or to desorb chemically bonded hydrogen[37]. Numerous materials have been investigated for physisorption, including zeolites, activated carbons, carbon nanotubes, and MOFs[41,77].

The U.S. Department of Energy has released volumetric and gravimetric density targets for hydrogen storage for on-board vehicular applications, along with fueling time, cost, and other targets.[36] Quantitative relationships between material characteristics and adsorption loadings are required to choose or design new materials to meet these targets. There exist many studies attempting to correlate adsorbate uptake with physical

characteristics such as the surface area and the free volume of an adsorbent material[36,41,42,45,47-50,77-79]. Nijkamp et al.[41] point out how the surface area and pore volume of a microporous material restrict the extents of adsorption in porous carbon and zeolitic materials. They conclude that materials with small pore volumes are less likely to be viable candidates for hydrogen storage. Vitillo et al.[78] determined a theoretical maximal storage of hydrogen in zeolites. They employed an interesting approach in determining these maxima by utilizing a flexible model of the material framework and assuming that the material was theoretically full once the volume of the material had expanded by 0.1% or 0.2% of its original volume. The enthalpy change upon adsorption ($\Delta H^{ads}$) is also clearly important for creating the negative free energy of adsorption ($\Delta G^{ads}$) required for adsorption to be favorable[23,27,59]. There are many quantities used to characterize $\Delta H^{ads}$ in the literature. In this work, we use the isosteric heat of adsorption at low loading ($Q_{st}$), as this reflects mainly the interaction between the adsorbate and the host framework.

In our previous work [79], we showed that $Q_{st}$, the surface area, and the free volume each take on a dominant role at different extents of loading in determining the amount of hydrogen adsorbed. We performed molecular simulations of hydrogen adsorption in a series of 10 isoreticular MOFs at 77 K up to 120 bar. These materials all have the same framework topology and surface chemistry. The results showed that at low loadings, hydrogen uptake correlates with the heat of adsorption; at intermediate loadings, hydrogen uptake correlates with the surface area; and at the highest pressures, uptake correlates with the free volume of the MOF. These correlations were based on the

absolute amount adsorbed. In this paper, we test these correlations at room temperature and for the excess amount adsorbed, the quantity that is measured experimentally.

Recently, Bhatia and Myers[80] discussed the optimum adsorption enthalpy change for hydrogen storage. They considered the full adsorption/desorption cycle in order to obtain an estimate of the optimum enthalpy change, noting that one must take into account both the loading pressure *and* the discharge pressure to determine the amount of gas actually delivered between the two pressures. They performed a classical thermodynamic analysis, assuming Langmuir isotherms with a constant entropy change of adsorption across all materials. One of the main points of their paper is that increasing the heat of adsorption is necessary, but increasing it too much will cause too much adsorption at the discharge pressure and lead to low gas delivery. At ambient temperature and delivery between 30 and 1.5 bar, Bhatia and Myers estimate an optimum adsorption enthalpy of 15.1 kJ/mol. It should be noted that this is a necessary but not sufficient condition; some materials may provide the optimal enthalpy but not have enough pore volume to store the required amount of gas.

Several means of increasing the heat of adsorption in MOFs have been suggested in the literature. Catenation[13,31,44,81] produces smaller pores and more corners, which both generally provide higher heats of adsorption, but there is a decrease in pore volume compared to the non-catenated structure that must also be taken into account. Impregnating nonvolatile guest molecules into the framework has similar potential advantages and disadvantages[44]. Coordinatively unsaturated metal sites have been credited with increasing $H_2$ uptake in MOFs and related materials[63,82-84]. This strategy does not sacrifice pore volume, but the increased adsorption is likely to be largest at low

pressures rather than at full loading. Another strategy is to add charges to the system. Molecular simulations have shown increased hydrogen adsorption in charged carbon nanotubes[85], supporting the idea that charged MOF frameworks would increase hydrogen storage. Recently Mulfort and Hupp showed that MOFs synthesized with redox-active ligands can be reduced by the addition of lithium metal, producing lithium cations and negatively charged frameworks[18,86]. This strategy increased the heat of adsorption and nearly doubled the hydrogen uptake. There are thus a variety of methods by which the heat of adsorption for hydrogen in MOFs may potentially be increased.

In this study we take an empirical approach, employing grand canonical Monte Carlo (GCMC) simulation results to determine a range of acceptable isosteric heats and free volumes that will provide the Department of Energy targets, for example 6 wt% and 45 g/cm$^3$ by 2010[36]. In this method we artificially turn up the heat of adsorption by increasing the Lennard-Jones interaction parameters between $H_2$ and the MOF atoms. In addition to calculating the usual gravimetric and volumetric adsorption quantities, we examine the density of hydrogen within the pore volume, $\rho_{ad}$, and show how this quantity can provide additional insight into the effect that varying free volumes among different MOFs has on the total volumetric or gravimetric uptake. We conclude by determining a simple, empirical relationship of the absolute amount adsorbed at 120 bar and 298 K with the isosteric heat at low loading ($Q_{st}$) in six materials and then present a graph that shows the required heats of adsorption for materials of various free volumes to meet specified gravimetric and volumetric storage targets.

### *3.2: Simulation methods*

This study investigates 6 different materials. Five are from the class known as IRMOFs, having oxide-centered $Zn_4O$ corners each connected to six dicarboxylate linkers to form cubic structures as shown in *Figure 3.1*[15-17]. These structures contain two types of cavities: cavities where the linkers point in and cavities where the linkers point out. There are, therefore, two distinct pore sizes, as listed in *Table 3.1*. The sixth material investigated is Cu-BTC, also known as HKUST-1[87]. This material contains metal corners consisting of two $Cu^{+2}$ ions coordinated to 1,3,5-benzenetricarboxylic acid organic linkers[87,88]. This leads to a different type of topology compared to the IRMOFs. Cu-BTC has main channels approximately 9 Å in diameter surrounded by tetrahedral side pockets of 5 Å in diameter connected to the larger channel via triangular windows of diameter of 3.5 Å[88].

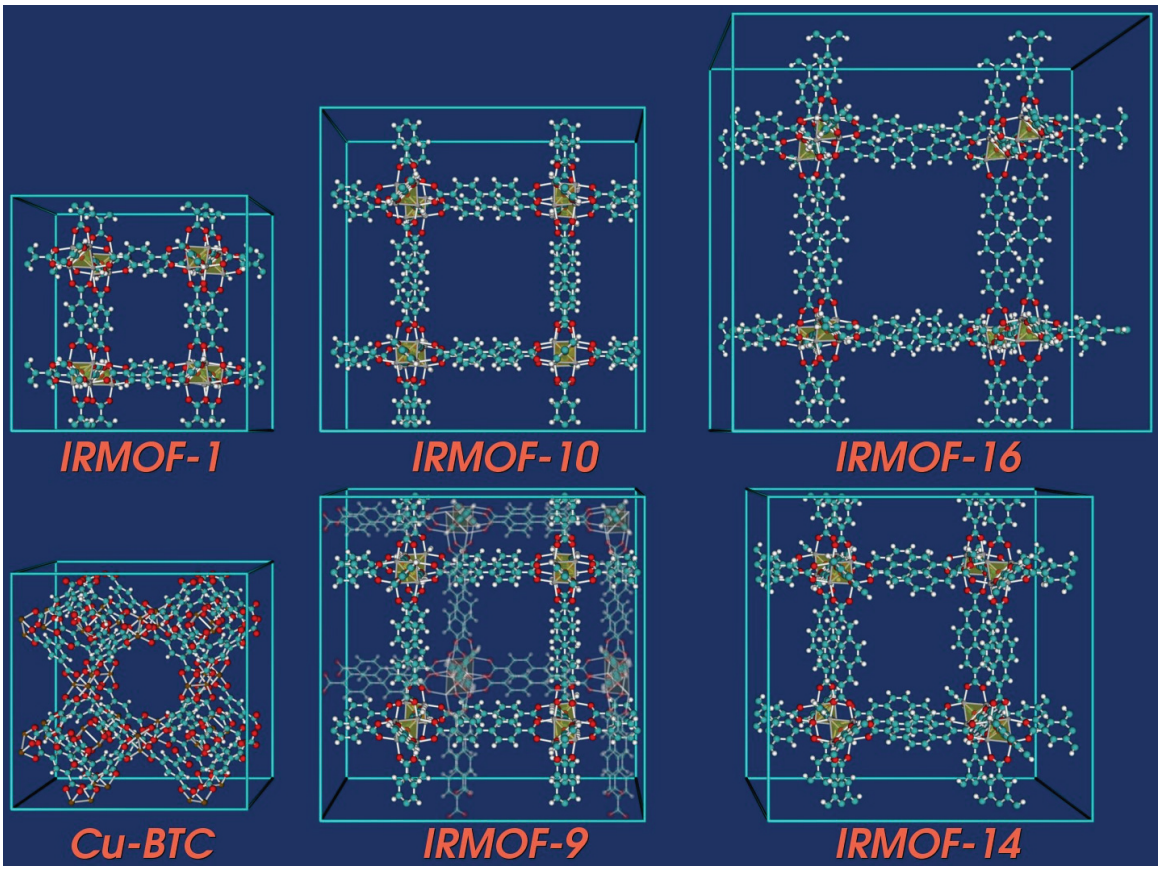


**Figure 3.1: Framework geometries of the MOF materials studied. Note that IRMOF-9 is a catenated form of IRMOF-10 and the interwoven structure has been made slightly transparent for easier viewing.**

**Table 3.1: Properties of the MOF materials studied.**

| Material | pore diameter Å | material density, ρ g/cm$^3$ | isosteric heat, $Q_{st}$[a] kJ/mol | free volume per mass cm$^3$/g | void fraction |
|---|---|---|---|---|---|
| **IRMOF-1** | 10.9/14.3 | 0.59 | 4.5 | 1.315 | 78% |
| **IRMOF-9** | 4.5/6.3/8.1/10.7 | 0.66 | 5.6 | 1.103 | 72% |
| **IRMOF-10** | 16.7/20.2 | 0.33 | 3.9 | 2.615 | 86% |
| **IRMOF-14** | 14.7/20.1 | 0.37 | 4.3 | 2.259 | 84% |
| **IRMOF-16** | 23.3 | 0.21 | 3.5 | 4.413 | 90% |
| **Cu-BTC** | 9/5 (3.5 windows) | 0.88 | 5.8 | 0.801 | 70% |

[a] The isosteric heat of adsorption for $H_2$ at low loading.

Hydrogen adsorption within the MOF materials was simulated with GCMC[51,52] using our multipurpose simulation code Music[53]. Each step in the Monte Carlo routine consisted of the insertion of a new molecule, deletion of an existing molecule, or

translation of an existing molecule. A total of 5 million steps were used, the first half for equilibration and the second half to calculate the ensemble averages. Gas-phase fugacities were calculated with the Peng-Robinson equation of state. The diatomic hydrogen molecule was modeled as a single sphere, and an atomistic model was used for the adsorbent material. The material was considered rigid with atoms positioned according to the crystallographic data[15-17,87]. We considered only dispersion and repulsion interactions, modeled using the standard Lennard-Jones equation.

$$\mathcal{V}(r) = 4\varepsilon\left[\left(\frac{\sigma}{r}\right)^{12} - \left(\frac{\sigma}{r}\right)^{6}\right] \tag{3.1}$$

Coulombic interactions were not included as they were stated to have little effect on $H_2$ adsorption at 298 K in the work of Garberoglio et al.[59] The Lennard-Jones parameters for the hydrogen molecule are derived from experimental work[54] and have been used in similar studies previously[55,79]. The parameters for the framework atoms were taken from the DREIDING force field[56], except for the copper atom which is not available in DREIDING and was found in UFF[89]. The Lorentz-Berthelot mixing rules were used to calculate the mixed-atom parameters. Interactions beyond 12.8 Å were neglected. The Lennard-Jones parameters are given in the Supporting Information.

The Lennard-Jones parameters were then systematically increased, multiplying the epsilon parameters (ε) by 1.1, 1.2, 1.5, 2, 3, 4, 5, and 10 times their original values. This provided us with 8 new parameter sets in addition to the original, for a total of 9 parameter sets using the same basic Lennard-Jones model. The epsilon parameter (ε) describing the $H_2$-$H_2$ interaction was left unaltered in all calculations, so the adsorbent-adsorbate interaction was enhanced while leaving the adsorbate-adsorbate interaction

constant. The effect on increasing ε in the Lennard-Jones potential can be seen in *figure 3.2*. Increasing epsilon while keeping sigma constant results in a deeper potential well but leaves the separation corresponding to the minimum of the well and the zero energy separation value constant. Thus, we increase the interaction energy without significantly affecting the size of the molecule in the various parameter sets.

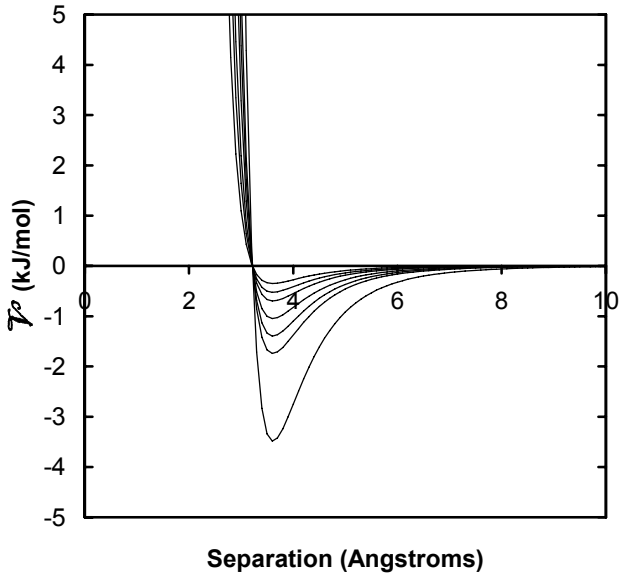


**Figure 3.2: Lennard-Jones potentials for H2-carbon interaction for all tested parameter sets.**

The isosteric heat at low loading was calculated between 0 and 0.5 bar assuming the gas phase to be ideal[26]. Note that throughout this paper, $Q_{st}$ indicates the isosteric heat of adsorption *at low loading*. The heat at low loading was used as it is relatively constant within this range and it reflects the interactions between hydrogen and the MOF with little contribution from hydrogen-hydrogen interactions. As in our previous study[79], we determined the so-called accessible surface area and free volume of each material using the experimental crystal structure and a simple Monte Carlo integration technique. We calculated the accessible surface area using a probe diameter of 2.958 Å to represent the

size of the $H_2$ molecule, and the free volume was calculated using a probe diameter of 0 Å to determine the absolute amount of volume not occupied by the framework atoms.

### *3.3: Results and discussion*

#### *3.3.1: Adsorption isotherms*

Hydrogen adsorption isotherms were calculated at 298 K first with the original parameter set described above. In order to compare our simulated results to experimental data from the literature they must be converted to excess adsorption values. Molecular simulation predicts the absolute number of hydrogen molecules within the framework, while experiments measure the so-called excess adsorption. The excess adsorption is the number of molecules above and beyond what would be found in a given volume if the adsorbent were not present[23]. The excess adsorption ($N_{ex}$) is determined from the absolute ($N_{abs}$) using the following equation:

$$N_{ex} = N_{abs} - V_g \, \rho_g \tag{3.2}$$

where $V_g$ is the pore volume calculated using the method of Myers and Monson[23] to mimic the experimental procedure, and $\rho_g$ is the density of the ambient gas phase calculated using the Peng-Robinson equation of state. Because of the various methods of calibrating experimental systems and determining the system volume and/or buoyancy corrections, some care should be taken in comparing results from different labs (including both simulations and experiments).

*Figure 3.3* compares simulation results from the original parameter set to experimental data from various sources. *Figure 3.3a* displays the comparison for $H_2$ adsorption in IRMOF-1 at 298 K[63,90,91], and *figure 3.3b* displays results in Cu-BTC at 298

K[63]. While the simulated and experimental curves are somewhat dissimilar, we correctly predict that Cu-BTC has higher excess adsorption than IRMOF-1 throughout the pressure range. Our model, while relatively simple, seems to provide acceptable results. It is evident from *figure 3.3a* that the experimental $H_2$ adsorption data is somewhat scattered. Earlier reports for $H_2$ adsorption in IRMOF-1 at 298 K indicated even higher uptake (as high as 10 mg/g at 20 bar)[71], but it was later determined these results were most likely contaminated by the presence of another gas. All of the results in *figure 3.3* indicate relatively low $H_2$ adsorption at 298 K compared to 77 K; the small excess values measured are inherently more susceptible to the effects of experimental and statistical error. The error between the experimental results and the simulations could be due to our standard method of calculating excess adsorption from absolute adsorption compared to the experimental procedures for system calibration and measurement of the excess isotherms. Using the same model we obtained reasonable agreement with experiment in our previous study for $H_2$ adsorption at 77 K[79]. It has been seen that fitting force field parameters to experimental data can improve the accuracy[58]. However, we are not as concerned with predicting experimental numbers with tight tolerances as we are with uncovering how the fundamental differences between materials affect adsorption. This can be accomplished with a model that captures the essential physics of the system.

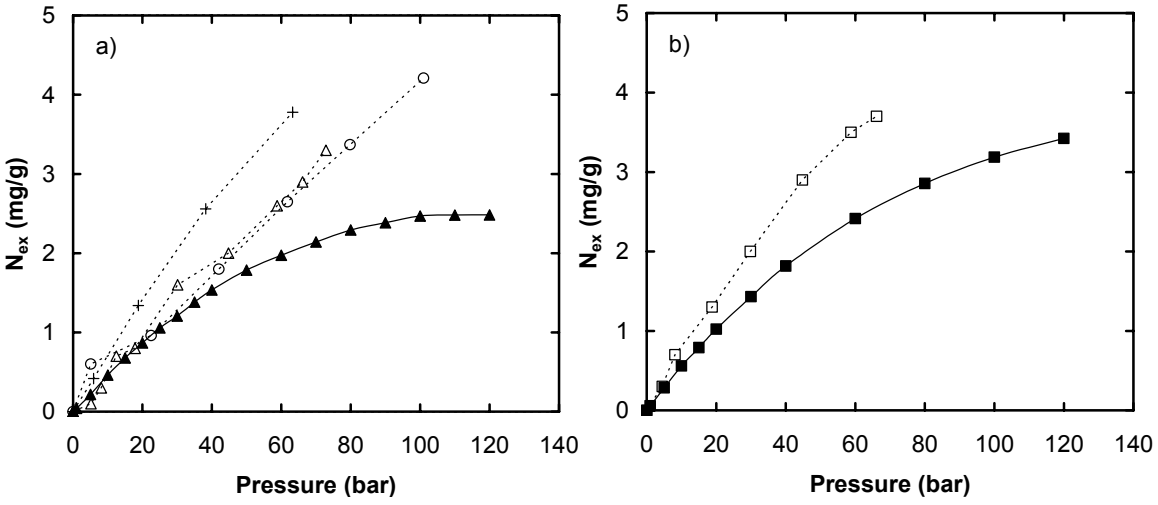


**Figure 3.3: a) Simulated and experimental adsorption isotherms for IRMOF-1 at 298K: ＋ Poirier et al. experiment[91]; △ Panella et al. experiment[63]; ○ Li et al. experiment[90]; ▲ simulation. b) Simulated and experimental adsorption isotherms for Cu-BTC at 298K: □ Panella et al. experiment[63]; ■ simulation.**

Next, we systematically altered the Lennard-Jones epsilon parameter (ε) to artificially increase the heat of adsorption within the MOF materials. We investigated 9 different parameter sets, the original and 8 systematically augmented interaction models. Multiplying epsilon by these values leads to a monotonic increase in the isosteric heat of adsorption at low loading ($Q_{st}$), as shown in *figure 3.4*.

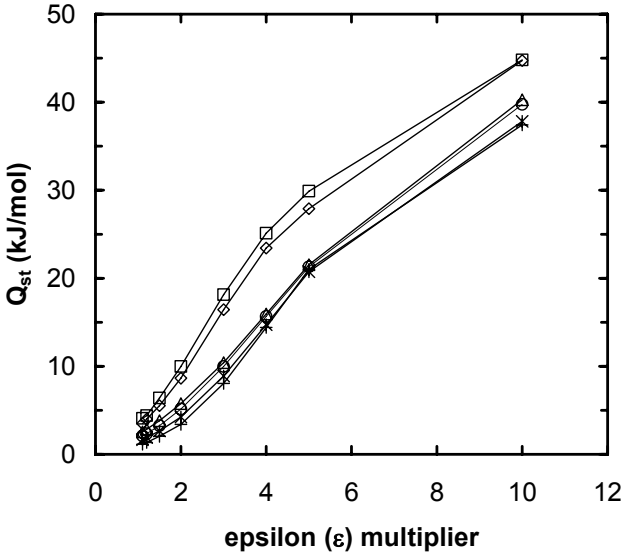


**Figure 3.4: The effect of changing the Lennard-Jones epsilon (□) parameter on the isosteric heat of adsorption at low loading (Qst). △ IRMOF-1; ◇ IRMOF-9; ∗ IRMOF-10; ○ IRMOF-14; + IRMOF-16; □ Cu-BTC.**

*Figure 3.4* indicates that Cu-BTC provides the largest heat of adsorption, followed by the interpenetrated IRMOF-9. While Cu-BTC is not interpenetrated, its structure contains very small pores. Most of the attention in the literature has focused on the open-metal sites within Cu-BTC as the cause of this increased adsorption enthalpy[31,63]. Rowsell et al.[31] note that the dipoles on the exposed surface of the open metal sites are expected to increase the interaction energy for adsorbate molecules around these sites. Our simulations employ only simple Lennard-Jones interactions, yet still show Cu-BTC as providing a larger heat of adsorption than the other materials studied. This suggests that the open-metal sites may not be the primary cause of the increased attraction of Cu-BTC compared to the IRMOFs. The smaller pores and increased number of corner sites also play a significant role.

$H_2$ adsorption was investigated in each of the six materials using the 8 new parameter sets described above along with the original parameter set from which they were derived.

The resulting isotherms at 298 K are shown in *figure 3.5*. Results are presented in terms of the absolute adsorption. The dashed line represents the adsorption of $H_2$ at 77 K with the original parameter set. This provides some idea of how much the energetic interactions must be increased to reach at 298 K the amount adsorbed at 77 K. *Figure 3.5* shows that IRMOF-1 adsorbs more hydrogen in an absolute sense than Cu-BTC does. However, *Figure 3.3* shows that Cu-BTC yields larger "excess" adsorption than IRMOF-1 from both simulation and experiment. This is due to the fact that IRMOF-1 has a substantially higher free volume than Cu-BTC, as discussed below. This reversal emphasizes the important difference between the absolute and excess adsorption.

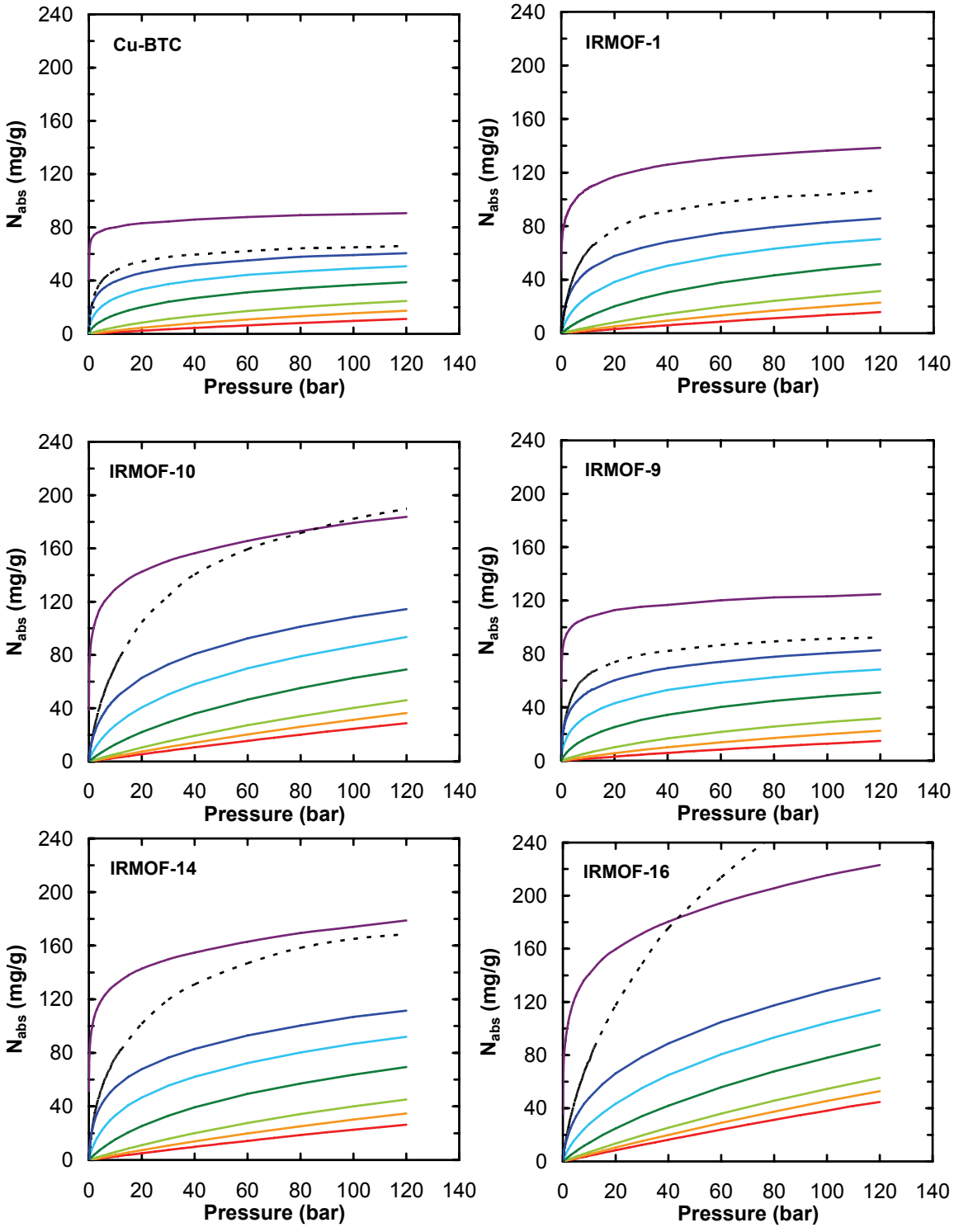


**Figure 3.5: Absolute hydrogen adsorption in 6 MOF materials at 298 K using various parameter sets. The isotherms from bottom to top start with the original parameter set and then the isotherms resulting from multiplying ε by 1.5, 2, 3, 4, 5, and 10 times the original value. The isotherms from multiplying ε by 1.1 and 1.2 times the original value were omitted for easier viewing. The dashed line represents the adsorption of $H_2$ within these materials at 77 K with the original parameter set.**

*3.3.2: Correlation of adsorption with $Q_{st}$, accessible surface area, and free volume*

In our previous work[79] based on GCMC simulations at 77 K, we proposed that the absolute amount adsorbed correlates with the isosteric heat at low loadings (low pressures), with the surface area at intermediate loadings, and with the free volume at high loadings. In this work we repeated this correlation analysis for hydrogen adsorption at 298 K and the different force field parameter sets. The results show more complexities in adsorption behavior than may have been inferred from our correlation results at 77 K[79].

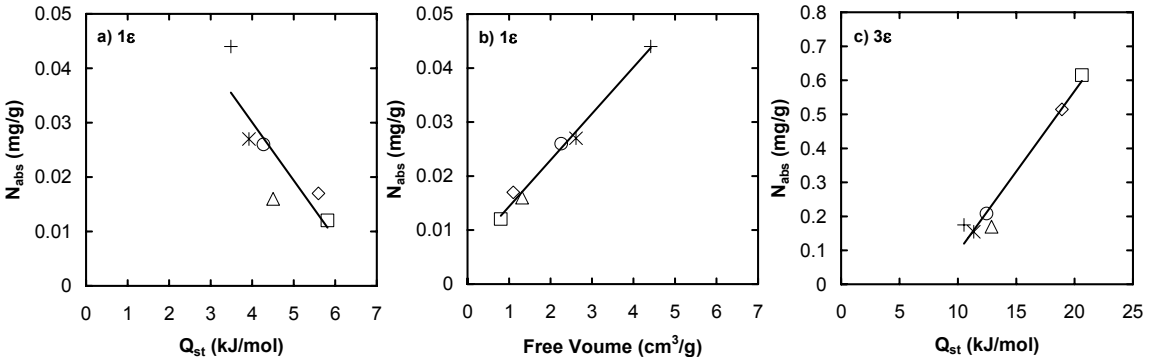


**Figure 3.6: Sample correlations of absolute adsorption with various material characteristics using different simulation parameter sets. a) correlation of the absolute $H_2$ adsorption at 0.1 bar with $Q_{st}$ using the original parameter set; b) correlation of the absolute $H_2$ adsorption at 0.1 bar with free volume using the original parameter set; c) correlation of the absolute $H_2$ adsorption at 0.1 bar with $Q_{st}$ using the augmented parameter set 3ε. Symbols are the same as in Figure 4, each symbol representing a different material.**

The first striking result can be seen in *figure 3.6a*, which shows the correlation of the absolute amount of $H_2$ adsorbed at low pressure (0.1 bar) with the isosteric heat, $Q_{st}$, using the original parameter set. Essentially no correlation is seen, or at best a negative correlation exists. Recall that at 77 K and 0.1 bar the amount adsorbed displayed a nearly linear (positive) correlation with $Q_{st}$[79]. *Figure 3.6b* shows the correlation between the absolute amount of $H_2$ adsorbed at 298 K and 0.1 bar and the free volume again using the

original parameter set. Here, a clear linear relationship can be seen, indicating that at low pressures (0.1 bar) the amount of $H_2$ adsorbed at 298 K is dictated by the free volume of the material as opposed to the isosteric heat – opposite to what was found for adsorption at low pressure at 77 K. The reason for this is that at 298 K, when using the original parameter set, the excess adsorption is a very small fraction of the absolute (total) adsorption. This indicates that much of the $H_2$ found in the material at this pressure would exist there also in the absence of any adsorbate-adsorbent interaction. Thus, the materials with the largest free volume per mass available will contain the most hydrogen (per mass of material). This points out an important consideration when considering absolute adsorption: the relative magnitudes of the excess amount adsorbed compared to the total amount adsorbed should be noted. The cause of the negative correlation between absolute adsorption and $Q_{st}$ in *figure 3.6a* is that materials with larger free volumes (and larger pore sizes) in general provide lower isosteric heats. Therefore *figure 3.6a* simply represents the linear relationship between $H_2$ adsorption and free volume at 298 K and 0.1 bar seen in *figure 3.6b*.

*Figure 3.6c* shows results for the absolute amount adsorbed at 298 K using the *augmented* parameter set where the original epsilon value was multiplied by a factor of three (3ε). Here, one can deduce that for stronger adsorbent-adsorbate interactions the excess amount adsorbed increases substantially, and once again the absolute adsorption at low pressure (0.1 bar) correlates well with the isosteric heat, $Q_{st}$ as in our previous study.

The absolute amount of $H_2$ adsorbed in each of the six materials was checked for correlation with $Q_{st}$, the surface area, and the free volume. We investigated these correlations at eight different pressures (0.1, 0.5, 1, 5, 10, 30, 60, and 120 bar) and two of

the parameter sets (1ε and 3ε). Instead of showing a large number of correlation graphs such as the examples in *Figure 3.6*, we summarized the goodness of fit of each correlation using the coefficient of multiple determination, commonly referred to as $R^2$. This number gives an indication of how well the amount adsorbed correlates with a given materials characteristic. The results are shown in *figure 3.7*. Keep in mind that each point on the graph represents the $R^2$ value for a correlation similar to those seen in *figure 3.6*. For example, in *figure 3.7a*, the green triangle at the lowest pressure point (0.1 bar), represents the $R^2$ value for the correlation that is seen in *figure 3.6b*.

*Figure 3.7* allows us to see what factors are important at what extents of loading (or pressures) and how they evolve as loading is increased. *Figure 3.7a* shows the results for the original parameter set (1ε). Here one can see that at *all* pressures the free volume is the most important factor at 298 K. As mentioned previously, this is very different from our previous findings at 77 K[79], but it can be explained by the fact that the excess adsorption at 298 K is very low at all pressures compared to the amount that would be found in the ambient gas phase; thus the free volume dictates how much "ambient" $H_2$ is present per mass of material. For materials with increased interactions, this result changes, as shown in *figure 3.7b* for the parameter set 3ε. Now with the adsorbent walls providing stronger attraction, the excess adsorption is larger. This influences the correlations, and the results are similar to what was found in our previous work at 77 K[79], namely at low pressures the amount adsorbed is correlated with $Q_{st}$, at intermediate pressures the amount adsorbed is correlated with the surface area, and at high pressures the amount adsorbed is correlated with the free volume.

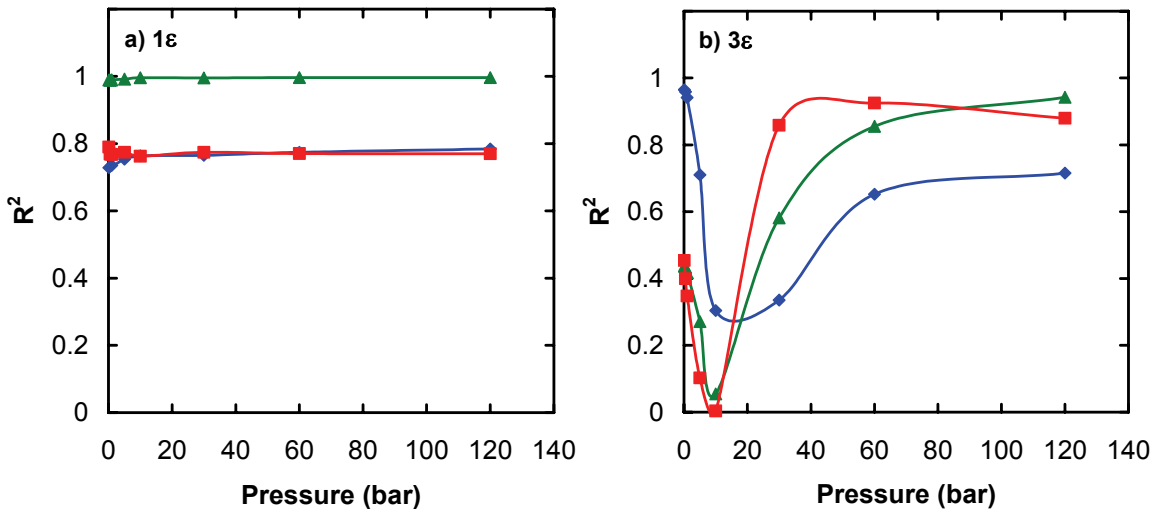


**Figure 3.7: Coefficients of multiple determination for correlations of absolute adsorption with the three material characteristics over a range of pressures at 298 K: ◆ isosteric heat; ■ accessible surface area; ▲ free volume. a) $R^2$ values for the original parameter set (1ε); b) $R^2$ values for the augmented parameter set 3ε.**

Another interesting feature in *figure 3.7b* is a dip in the $R^2$ values for the isosteric heat correlations as pressure is increased. This can be explained because there is a correlation between the free volume of the material and the isosteric heat as mentioned before. So as pressure is increased, the isosteric correlation begins to disappear, but then as the free volume correlation improves, this loose isosteric heat and free volume relationship comes into play.

Attempts to test similar correlations using experimental data necessarily focus on the excess adsorption, as this is the quantity measured, rather than the absolute adsorption[13,41,42,45,47-50,77]. Some recent experimental work by Panella et al.[77] showed that hydrogen adsorption at high pressures correlated well with the surface area. To examine how the excess adsorption data from our simulations correlates with material characteristics, we repeated the analysis of *figure 3.7* using the excess adsorption amounts instead of the absolute adsorption. The $R^2$ results for excess adsorption are

shown in *figure 3.8.* With the original parameter set (1ε) in *figure 3.8a*, there is no correlation with any of the three materials characteristics examined. This is not surprising, considering the extremely low excess adsorption amounts (shown below). The results for the augmented parameter set 3ε in *figure 3.8b* show that the isosteric heat, $Q_{st}$, is important at low pressures and correlation with the surface area becomes stronger at higher pressures. There is never a strong correlation with the free volume in this pressure range. These results seem to follow intuition; excess adsorption is due to interactions with the framework, so one would expect it to correlate with the amount of surface area available and not the free volume. In general, the correlations using the absolute adsorption are somewhat easier to understand from a physical point of view, but the correlations using the excess adsorption provide a link to experiments.

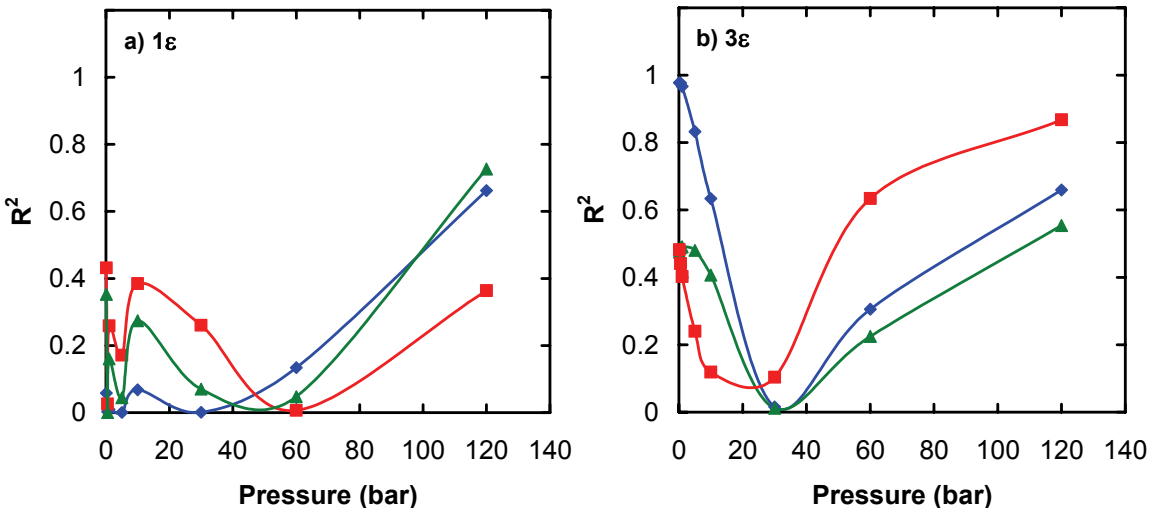


**Figure 3.8: Coefficients of multiple determination for correlations of excess adsorption with the three material characteristics over a range of pressures at 298 K: ◆ isosteric heat; ■ accessible surface area; ▲ free volume. a) $R^2$ values for the original parameter set (1ε); b) $R^2$ values for the augmented parameter set 3ε.**

The correlations of $H_2$ adsorption in *figures 3.6, 3.7,* and *3.8* suggest that the difference between the total amount adsorbed (i.e. the absolute adsorption) and the excess

amount adsorbed can be significant. A summary of the gravimetric adsorption uptake, both absolute and excess, for all six materials can be seen in *figure 3.9*. *Figure 3.9a* shows the results with the original parameter set and *figure 3.9b* shows the results from the 3ε parameters. The absolute adsorption isotherms are represented with a solid line and the excess adsorption is represented with a dashed curve. The low excess adsorption compared to the absolute adsorption is clearly displayed in *figure 3.9a*. As the interaction energy between the hydrogen and the material increased, so did the excess adsorption and the difference between the two values is much less significant in *figure 3.9b*.

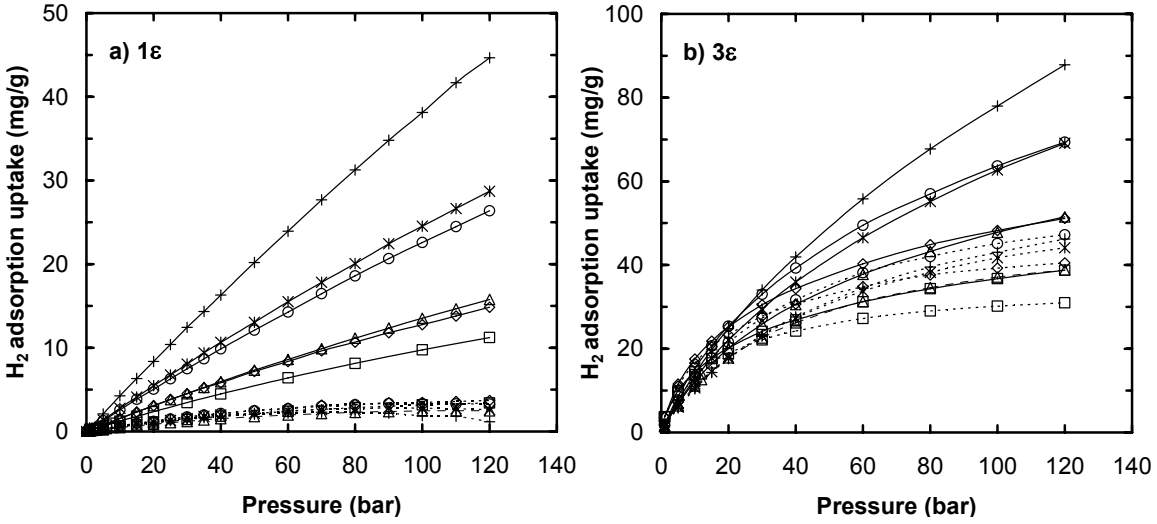


**Figure 3.9. Gravimetric hydrogen uptake at 298 K. △ IRMOF-1; ◇ IRMOF-9; ∗ IRMOF-10; ○ IRMOF-14; + IRMOF-16; □ Cu-BTC; solid line – absolute adsorption; dotted line – excess adsorption. a) Gravimetric hydrogen uptake using the original parameter set (1ε); b) Gravimetric hydrogen uptake using the augmented parameter set 3ε.**

Conceptually, the difference between absolute and excess values can be thought of as gas in its ambient state, i.e. gas that would exist within the pores even if the material provided no interaction energy. As the ambient $H_2$ density will be the same in all materials, it is the free volume that determines the amount of ambient $H_2$ that exists per mass of the material. As shown in Table 1, the free volumes of MOFs can vary widely.

For example the free volumes per mass of IRMOF-16 and Cu-BTC differ by a factor of 5.5. Thus, much of the magnitude of the absolute gravimetric adsorption seen in *figure 3.9* is due simply to differences in free volume. This suggests that to remove this effect, we should look at the adsorption in terms of the $H_2$ density *within the pore or free volume of the material*, a quantity we will call $\rho_{ad}$. This may enable us to see more clearly the effects of chemical functionality, interpenetration, and pore size on the ability of different materials to take up light gasses such as $H_2$. In addition, it is instructive to compare $\rho_{ad}$ with the density of the ambient $H_2$ gas, $\rho_g$. The quantity $\rho_{ad}$ can be calculated by simply dividing the amount adsorbed per mass by the free volume per mass:

$$\rho_{ad}\left[\frac{mg}{mL}\right] = \frac{N\left[\frac{mg}{g}\right]}{\left(\frac{FreeVolume}{Mass}\right)\left[\frac{mL}{g}\right]} \tag{3.3}$$

It should be noted in eq. (3.3) we leave the adsorbed amount, N, generic, as it could be either the absolute adsorption, $N_{abs}$, or the excess adsorption, $N_{ex}$, depending if we are considering the pore adsorption density, $\rho_{ad}$, as the $H_2$ density within the pores absolutely, $\rho_{ad,abs}$, or if we are considering it as the density within the pore due only to the excess adsorption, $\rho_{ad,excess}$.

*Figure 3.10a* contains the data for $H_2$ density within the pores, $\rho_{ad}$, in all 6 materials using the original force field (1ε). Each material is represented by a unique symbol, and there are two sets of curves for each material. The larger values with solid lines are the total (absolute) gas density within the material, and the smaller values with dotted lines represent the density due to excess adsorption. Finally, the thick black curve represents

the ambient hydrogen density, $\rho_g$, at 298 K. The addition of the excess density values to the ambient hydrogen density leads to the absolute density within the pores. This graph clearly indicates that the majority of the $H_2$ found within the materials is not due to the excess adsorption, as the excess values (the $H_2$ truly adsorbed) are much lower than the total. This explains the reason for the dominance of the free volume characteristic seen in *figure 3.7a*. In *figure 3.10b* the $H_2$ density within the pores, $\rho_{ad}$, is plotted for the adsorption data from the superficially augmented parameter set 3ε. In this case, the density within the pores due to excess adsorption (and thus also the absolute adsorption density, $\rho_{ad,abs}$) has increased substantially compared to *figure 3.10a*.

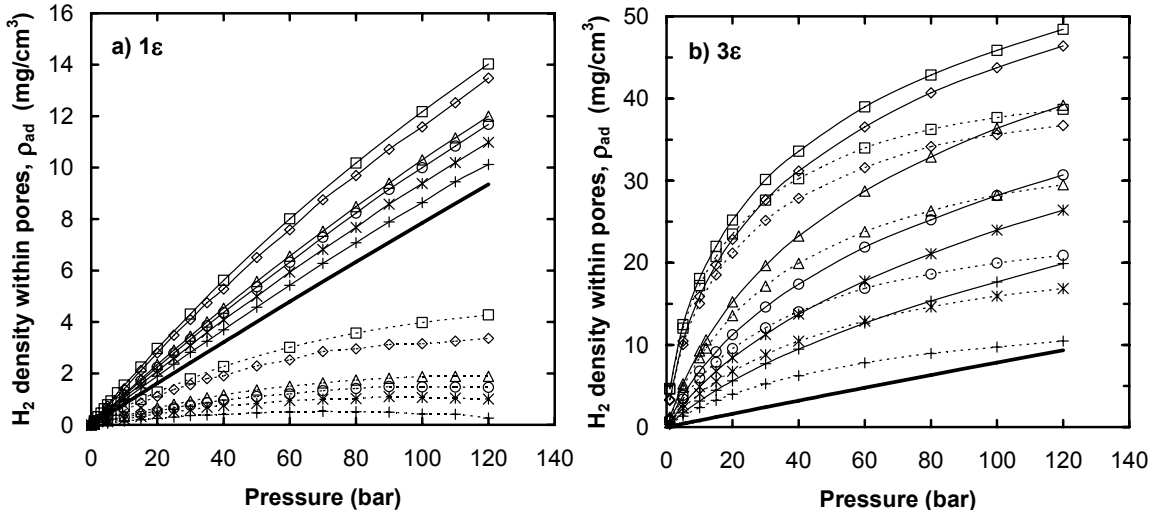


**Figure 3.10: Hydrogen density within the free volume or pore space of the material. △ IRMOF-1; ◇ IRMOF-9; ∗ IRMOF-10; ○ IRMOF-14; + IRMOF-16; □ Cu-BTC; solid line – absolute density, $\rho_{ad,abs}$; dotted line – excess density, $\rho_{ad,ex}$; thick black line – bulk gas-phase $H_2$ density. a) $H_2$ density within the pores, $\rho_{ad}$, using the original parameter set (1ε); b) $H_2$ density within the pores, $\rho_{ad}$, using the augmented parameter set 3ε.**

*Figure 3.10a* also shows that Cu-BTC and IRMOF-9 have the highest density of hydrogen within the pores. This can easily be attributed to the small pore sizes in these materials. IRMOF-9 is a catenated structure. Many groups have postulated that

restricting the pore size through catenation may be a promising strategy for increasing the heat of adsorption and thus hydrogen storage in MOFs. The important question is whether the increase in hydrogen density within the pores, $\rho_{ad}$, is enough to compensate the loss of free volume from catenation. To answer this question, consider the density of hydrogen found at 120 bar in IRMOFs-9 and -10 found in *figure 3.10b*. This graph shows that hydrogen in IRMOF-9 has a density 80% larger than the non-interpenetrated IRMOF-10 at this pressure. However, the gravimetric uptake shown in *figure3.9b* clearly indicates that once the hydrogen density has been multiplied by the materials' corresponding free volume, this enhancement of density is not enough to offset the fact that IRMOF-9 has less than 43% of the free volume per mass of IRMOF-10. Thus, IRMOF-10, the non-catenated structure, has the larger gravimetric uptake.

Our previous study[79] provided perhaps the false picture that (absolute) uptake at high pressures was *solely* dependent on the free volume. However, the isotherms in *figure 3.5* with the various parameter sets clearly indicate that the heat of adsorption substantially affects hydrogen uptake at high pressure. For a given material, the free volume is fixed, but the uptake increases as the interaction energy is increased.

*Figure 3.11* charts the absolute hydrogen density within the pores, $\rho_{ad,\ abs}$ at 120 bar and 298 K vs. the isosteric heat, $Q_{st}$ for all 6 materials and the 9 parameter sets studied. There is a clear relationship between the density in the pores and $Q_{st}$. It is interesting to note the difference in slopes among the various materials. For example, the density in the pores of IRMOF-16 does not increase as much with increasing $Q_{st}$ as in the other materials. This indicates a pore size effect and that the density of hydrogen in materials with different geometries can vary for different pore sizes at the same value of $Q_{st}$. A

material with large pores can provide high interaction energies near the walls but will have more space further from walls where adsorbate molecules have little attraction to the material surface. This provides a picture of how efficiently or effectively a material uses its pore volume. Interestingly, IRMOF-1 seems to use its pore volume the most efficiently. Note that both smaller pores (Cu-BTC and IRMOF-9) and larger pores (IRMOF-10, 12 16) have lower densities than IRMOF-1 at the same values of $Q_{st}$.

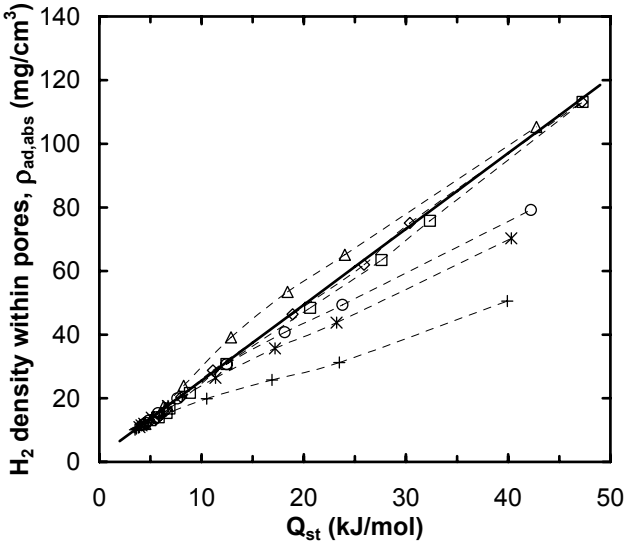


**Figure 3.11: Relationship between absolute adsorbed hydrogen density within the pores at 298 K and 120 bar and isosteric heat at low loading, $Q_{st}$. △ IRMOF-1; ◇ IRMOF-9; ∗ IRMOF-10; ○ IRMOF-14; + IRMOF-16; □ Cu-BTC; thick black line – equation of best fit for data from IRMOFs-1, -9 and Cu-BTC.**

### *3.3.3: Design trade-off between $Q_{st}$ and free volume*

*Figure 3.11* provides a useful relationship between the isosteric heat and the density of hydrogen within the free volume at 120 bar and 298K. A line was fitted to the data of IRMOFs-1 and -9 and Cu-BTC in *figure 3.11* and is shown as a thick black line. The resulting empirical equation is:

$$\rho_{ad,abs} = 2.38 Q_{st} + 1.79 \qquad (3.4)$$

where $\rho_{ad,\,abs}$ is the absolute density of hydrogen within the pores in mg/cm$^3$ and $Q_{st}$ is the isosteric heat at low loadings in kJ/mol. This equation can then be used in a rearranged eq. (3.3), with the free volume corresponding to the material of interest, to estimate the gravimetric uptake, N. Alternatively, the density can be multiplied by the void fraction instead of the free volume per mass to determine the volumetric adsorption loadings.

This analysis allows us to show the trade-off between the isosteric heat and the free volume. Using eq. (3.4) with eq. (3.3) and assuming an absolute gravimetric adsorption target, a curve displaying the required isosteric heats, $Q_{st}$, and free volumes for the desired adsorption uptake can be obtained. *Figure 3.12a* illustrates the resulting free volume per mass and heat of adsorption requirements for a material to take up 6, 7, 8, and 9 wt. % based on our simulation work. These curves highlight the importance of free volume, as materials with free volumes less than 1 cm$^3$/g require very high $Q_{st.}$ However, materials with larger free volumes show more realistic targets for $Q_{st}$. *Figure 3.12b* displays the resulting void fractions and isosteric heats of adsorption for a material to obtain 30, 45, 60, and 81 g $H_2$/cm$^3$. The DOE volumetric targets are 45 g/cm$^3$ by 2010 and 81 g/cm$^3$ by 2015[36]. (These values are italicized in *figure 3.12.*) It is evident that IRMOFs will have great difficulty meeting the 2015 volumetric targets, and even the 2010 target of 45 g/cm$^3$ will require a material a $Q_{st}$ of at least 25 kJ/mol if the void fraction is 0.9. A seemingly more realistic target of 30 g/cm$^3$ is also provided in the figure. Upon comparing the two graphs, a reasonable goal of 9 wt.% and 30 g/cm$^3$ could be obtained with MOFs if a new material can provide an isosteric heat of 15 kJ/mol or higher while maintaining a free volume of 2.5 cm$^3$/g and void fraction of 85%.

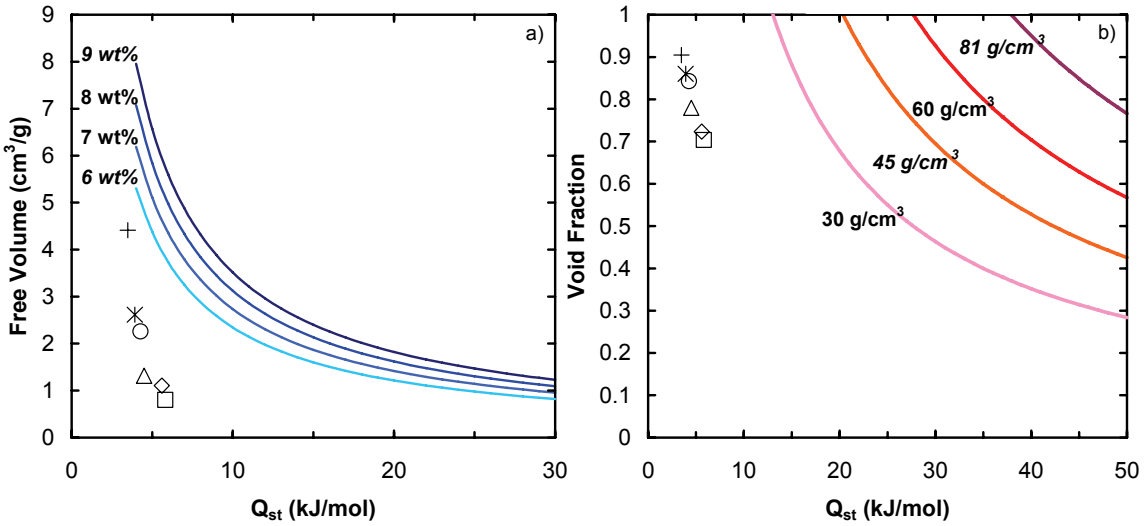


**Figure 3.12: a) Requirements for target gravimetric loadings at 120 bar and 298 K. b) Requirements for target *volumetric* loadings at 120 bar and 298 K. △ IRMOF-1; ◇ IRMOF-9; ✳ IRMOF-10; ○ IRMOF-14; + IRMOF-16; □ Cu-BTC.**

The decision to determine the correlation in eq. 4 using only IRMOFs-1, -9 and Cu-BTC was made for two reasons. First, it was decided that we would rather report the minimum requirements, in terms of free volume and isosteric heat, and so we chose a line with a slightly larger slope than what some materials represented. Second, the materials left out of the correlation (IRMOFs-10, -14, and -16) are of higher free volumes (2.6, 2.3 and 4.4 $cm^3/g$), and *figure 3.12a* shows that the materials with free volumes between 2.3 and 4.4 $cm^3/g$ require isosteric heats between 5 and 15 kJ/mol for the various gravimetric (wt. %) targets. Returning to *figure 3.11*, it is evident that these three materials (IRMOFs-10, -14, and -16) are predicted well using the correlation in eq. (4) in this low $Q_{st}$ range (5 to 15 kJ/mol). We believe that *figure 3.12* provides useful design requirements for obtaining target gravimetric $H_2$ loadings within MOFs (and perhaps other similar microporous materials). Certainly, *figure 3.12* illustrates the trade-off between free volume and $Q_{st}$.

*Figure 3.12* also displays the actual free volumes and $Q_{st}$ of the six materials studied (identified by unique symbols). It is evident that because of the chemical and geometric nature of adsorption within these materials they exhibit a weak negative correlation between free volume and $Q_{st}$ as mentioned previously. It is also evident from a comparison of IRMOFs-9 and -10 that the increase in $Q_{st}$ due to interpenetration does not adequately compensate for the decrease in free volume that occurs. IRMOF-16 is the closest material to reaching the required 6 wt. % goal. This suggests that researchers should concentrate on increasing the isosteric heat of adsorption for materials with large free volumes.

### *3.4: Conclusion*

This study has highlighted several important aspects of physisorption in MOFs, with particular attention to comparing hydrogen storage in different microporous materials. In our previous work, we showed correlations of the amount adsorbed with the heat of adsorption at low loadings, the surface area at intermediate loadings, and the free volume at high loadings. Here we showed that the correlations, which were developed for absolute adsorption, do not hold well for very weak adsorption, where the gas inside the pores is close to the bulk gas density. For such weak adsorption, the amount adsorbed mainly correlates with the amount of volume available, even at low loadings. The correlations were tested for excess adsorption, and it was found that the amount adsorbed correlates well with the heat of adsorption again at low loading, but at the highest loadings, the excess adsorption correlates better with the surface area than the free volume.

The difference between absolute and excess adsorption is of great importance in understanding adsorption data. For example, IRMOF-1 adsorbs more hydrogen in an absolute sense than Cu-BTC does, but Cu-BTC shows a larger excess adsorption than IRMOF-1. This is due to the fact that IRMOF-1 has a substantially larger free volume. The difference between the absolute and excess amount adsorbed can be significant for some systems. Examining the density of hydrogen within the pore void volume (rather than per total volume of material) can be a useful way to think about and compare different sorbents.

Materials with larger pores generally show lower heats of adsorption. Choosing sorbents with smaller pores for their higher heats of adsorption, however, comes with a cost in free volume that may or may not be off-set. Based on a correlation between the density of hydrogen in the pore void volume and the heat of adsorption, we prepared a chart showing combinations of heat of adsorption and free volume that meet target gravimetric and volumetric storage amounts. The graph suggests that if new materials can achieve an isosteric heat of 10 to 15 kJ/mol with a free volume between 1.6 and 2.4 $cm^3/g$ gravimetric $H_2$ uptake of 6% could be achieved. Materials with free volumes less than 1.5 $cm^3/g$ or void fractions of less than 75% will need isosteric heats larger than 20 kJ/mol to achieve 6 wt. % and 30 $g/cm^3$ of $H_2$.

Our results for IRMOF-9 and IRMOF-10 suggest that catenation is not a promising option to increase the isosteric heat. For this pair of frameworks, the increase in isosteric heat gained through interpenetration (a type of catenation) does not off-set the loss in free volume, and so hydrogen uptake is larger in the non-catenated material. Thus, alternate methods of increasing the heat of adsorption should be investigated, such as open metal

sites and charged frameworks. Others concepts including dissociation/spillover[90,92] and MOFs using lighter framework metal atoms with unsaturated coordination sites[93] also appear promising in this regard. It is clear that increasing the interaction energy between hydrogen and the material, while maintaining sufficient void space, is a necessary synthetic goal for hydrogen storage by physisorption to become viable.

# Chapter 4: Quantum Chemical Study of Hydrogen Binding on Bipyridine

## *4.1: Introduction*

MOFs have been studied extensively for use in hydrogen storage applications. In chapter 3, it was determined that in order to significantly enhance hydrogen loading at room temperature, it is required that we increase heats of adsorption without sacrificing void space. It has been reported that a manganese based MOF has achieved 6.9 wt% hydrogen gas uptake through the use of unsaturated $Mn^{2+}$ corner unit as the primary binding sites at 77 K and 90 bar[82]. This is one MOF that can reach the DOE goal for hydrogen storage weight percent but at a temperature below the DOE goal[36]. Another promising technique reported that the addition of a platinum catalyst attached to an activated carbon support bridged to a MOF can allow dissociated hydrogen atoms to "spillover" onto the MOF structure, greatly enhancing hydrogen storage capabilities[90,92].

The purpose of the present study is to determine the feasibility of improving the capacity of MOFs for hydrogen storage. Specifically, it has been hypothesized that $H_2$ adsorption, especially at nonmetal pore sites such as the organic ligand, can be enhanced by doping the structure with an electron donor such as lithium. It is believed that doping an electron onto an organic linker will increase the induced dipole-induced dipole interactions between the linker and $H_2$. This increased polarization should enhance the MOF-$H_2$ interaction.

It has been reported recently by Han et al. in other theoretical work that Li does in fact enhance hydrogen uptake[94]. Their model doped several Li atoms above the center of the fused aromatic rings of the organic linker but disregarded the possibility of Li

adsorbing onto the MOF metal corners. MP2 calculations were used to find the diffuse interactions between H-C, H-O, and H-Zn to build a force field. The resultant force field was used in a grand canonical Monte Carlo simulation for the uptake of Li-doped MOFs. They reported that gravimetric uptake of 6 wt% $H_2$ could be achieved at $-30^0$C and 100 bar.

Recently Ma et al[18]. and Mulfort et al.[86] have produced MOF materials that have the potential to be reduced via Li doping. Mulfort et al.[86] showed that both $H_2$ and $N_2$ adsorption increases after Li doping. Three of the structures synthesized by Ma et al.[18] contain bipyridine as one of the organic ligands. This molecule is used as the test subject in this study.

### *4.2: Methods*

The interaction of $H_2$ and Li with bipyridine was studied using second order Møller-Plesset perturbation theory (MP2). Geometry optimizations and energy calculations were performed on various systems using Gaussian03[35]. Further, MP2 was also used to study the interaction of $H_2$ with Li and $H_2$ with $Li^+$ without an organic strut to examine the isolated effect of the presence of a lithium cation in the system on $H_2$ binding. The higher level theory of MP2 was used as it is well known that density functional methods have difficulties in accounting for dispersion interactions inherent in these systems[65]; MP2 has been a popular method in similar studies on the interaction of $H_2$ with organic molecules found in MOFs[57,64,65,95-99]. The MP2 calculations were performed with a modest basis set of 6-31++G** and a larger basis set of AUG-cc-pVTZ, which includes one diffuse and one polarization function on all atoms. The basis sets were chosen as

they seemed to provide accurate results without excessive computational expense. Electronic binding energies were calculated from the quantum results in accordance with the method outlined in Chapter 1, section 1.4.

### *4.3: Results and discussion*

#### *4.3.1: Interaction of $H_2$, Li, and bipyridine*

Several studies were performed on the interaction of $H_2$ with the bipyridine molecule. Geometry optimization and energy calculations were performed using MP2 with the 6-31++G** basis set on the bare bipyridine molecule, bipyridine with a surrounding $H_2$, and again on the two systems with a charge of $1e^-$ superficially added to the bipyridine molecule to determine the effect of charge on the binding energy of $H_2$. Further, a system containing bipyridine, $H_2$, and Li was studied to examine the donation of charge by the Li atom to bipyridine and its effect on $H_2$ binding.

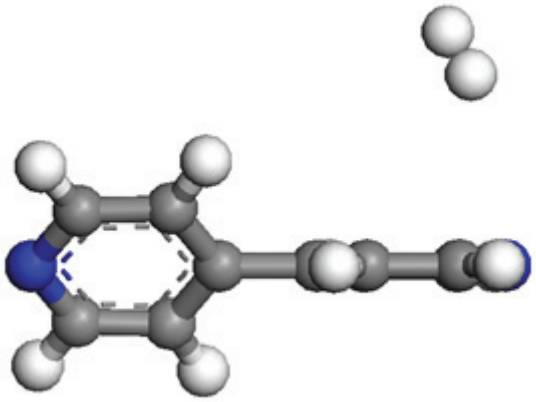

**Figure 4.1: Geometry of hydrogen interacting with the bipyridine molecule.**

The optimized geometry of the neutral bipyridine molecule with $H_2$ can be seen in *figure 4.1*. Initially the geometries were optimized using various DFT methods and then

single point MP2 energies were calculated on these optimized geometries. By comparing MP2 energies from geometries determined from different DFT methods and different $H_2$ starting positions, it was evident that the MP2 energy minimum was not being determined. Thus, geometry optimizations were eventually performed with MP2. Ultimately, two different $H_2$ starting positions both minimized to the configuration seen in *figure 4.1*.

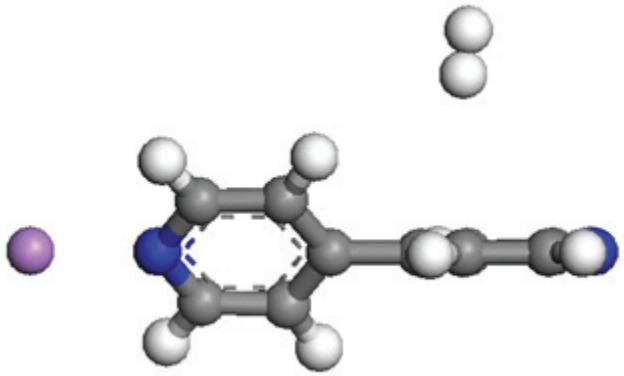

**Figure 4.2: The geometry of hydrogen and lithium interacting with the bipyridine molecule.**

A system with bipyridine, Li, and $H_2$ was also studied. The MP2 optimized geometry can be seen in *figure 4.2*. A summary of $H_2$ binding energies calculated using the 6-31++G** basis set and using an AUG-cc-pVTZ basis set from the same geometry can be seen in *table 4.1*.

**Table 4.1: Summary of electronic binding energies and geometry highlights. NOTE: all values were obtained from MP2 geometry optimizations using a 6-31++G** basis set.**

| System | 6-31++G** binding energy | AUG-cc-pVTZ binding energy | distance between $H_2$ and bipyridine (closest atom) |
|---|---|---|---|
| **$H_2$ and neutral bipyridine** | -4.49 kJ/mol | -5.03 kJ/mol | 2.91 Å |
| **$H_2$ and $1e^-$ charged bipyridine** | -6.46 kJ/mol | -6.80 kJ/mol | 2.94 Å |
| **$H_2$, Li, and bipyridine** | -5.30 kJ/mol | -5.78 kJ/mol | 2.98 Å |

*Figures 4.1 and 4.2* both display that a $H_2$ configuration perpendicular to the plane of the aromatic ring is preferred. This result has also been found in previous studies on the interaction of $H_2$ with aromatic systems[65]. The neutral system provides an electronic binding energy of -4.49 kJ/mol from the 6-31++G** results. This is in line with expectations. Hübner et al. found $H_2$ binding energies of 3.91 kJ/mol with $C_6H_6$ and 4.52 kJ/mol with $C_6H_5NH_2$ using MP2[65]. Similar energies have been reported by others[57,64,65,95,97]. The electronic binding energies are higher across the board when using the AUG-cc-pVTZ basis set. BSSE corrections (as described in Chapter 1, section 1.4) were estimated for the neutral system and found to be 2.6 kJ/mol. In theory, this value should be added to the electronic binding energies, which would make the AUG-cc-pVTZ results closer to those previously reported.

*Table 4.1* clearly indicates an increase in binding energy upon the addition of an electron to the system or Li doping. A 44 % increase in binding energy is found when an electron is superficially added to the bipyridine from the 6-31G** results, and a 37% increase from the AUG-cc-pVTZ results. The geometry for the $1e^-$ charged system (not shown) is nearly identical to what was found for the neutral system (*figure 4.1*) except that the bipyridine molecule is notably less twisted. This indicates that the addition of the

electron to bipyridine serves to flatten the molecule. Interestingly, the $H_2$ does not lie any closer to charged bipyridine although the interaction energy is enhanced. *Figure 4.2* shows the Li directly adjacent to one of the nitrogen atoms in bipyridine. This is an unrealistic configuration as the nitrogen would be coordinated to a metal post in the material. Further, the hydrogen is in a slightly different position over the ring as found in *figure 4.2*. Regardless, the effect of lithium's partial donation of an electron is shown as an 18% increase in binding energy using 6-31++G** and 15% increase using AUG-cc-pVTZ.

*4.3.2: Interaction of Li, $Li^+$, and $H_2$*

This study examines geometries and binding energies for a sole $H_2$ molecule surrounding various organic clusters. When these materials are exposed to $H_2$ at significant pressure multiple binding sites will be occupied. It is postulated that the $Li^+$ cation present in the system may also add a favorable binding location. To examine the isolated effect of the $Li^+$ cation, a system containing only Li and $H_2$ was investigated. Again MP2 with a basis set of 6-31++G** was used on these systems. When a $H_2$ was placed in the proximity (~ 2.5 Å) of a neutral Li atom, energy minimization separates the two species completely and the interaction energy is near 0 kJ/mol. However, when the Li atom is given a charge of +1, energy minimization places the $H_2$ 2.2 Å from the $Li^+$, and a binding energy of **-18.3 kJ/mol** is determined. This indicates that the presence of a positively charged Li ion will provide a favorable adsorption location inside the material framework and will also serve to increase the overall isosteric heat of adsorption.

### *4.4: Conclusion*

The quantum results from the interaction of $H_2$ and bipyridine in a neutral, charged, and Li doped state indicate that reducing a MOF certainly has the potential to increase the heat of adsorption and thereby hydrogen uptake. This is confirmed by the experimental studies performed by Mulfort et al.[86]

# Chapter 5: Understanding Inflections and Steps in Carbon-Dioxide Adsorption Isotherms in Metal-Organic Frameworks

The selective adsorption of carbon dioxide from gas mixtures is an important problem in many technical applications, and there is special interest recently due to concerns over greenhouse gas emissions. Metal-organic frameworks are permanently porous coordination polymers that have emerged as an important new class of porous materials that may have a big impact in adsorption separation technologies[1,8,9,16,17,20,42,47,82]. The ability to synthesize MOFs with various organic linkers and metal joints provides tremendous flexibility in tailoring the porous material to have specific physical characteristics and chemical functionalities. Information on host-guest interactions and adsorption mechanisms of molecules in MOFs is crucial for developing these novel materials for selective adsorption applications.

Recently, Millward and Yaghi[100,101] reported room temperature adsorption equilibrium data for $CO_2$ in a large variety of metal-organic frameworks. MOF-177 was shown to have a volumetric adsorption capacity for $CO_2$ that was substantially higher than that of commercial materials such as zeolite 13X and activated carbon powder. Several of the materials exhibited S-shaped isotherms, which were attributed to the very large pore sizes of the MOFs. Other groups[102-104] have reported $CO_2$ isotherms in MOFs with pronounced steps, which are ascribed to changes in the framework structures, such as a "breathing-type mechanism"[104] or a "gate effect."[102] These unusual isotherm shapes are not found for $CO_2$ adsorption in other microporous materials under similar conditions to the best of our knowledge.

In this work, we present experimental adsorption isotherms for $CO_2$ in IRMOF-1 (MOF-5) over a wide range of temperatures. With decreasing temperature, these isotherms exhibit dramatic steps with some similarities to those reported for $CO_2$ in other MOFs[102-104]. In addition, we present a molecular model that predicts the inflections and steps in very good agreement with experiment and helps explain the adsorption mechanisms that are responsible for this behavior. The molecular model assumes a *rigid* crystal structure and accounts for electrostatic interactions between $CO_2$ molecules by placing point charges on each atom. Similar models have been employed previously for calculating adsorption of $CO_2$ in other MOFs[105-110]. In this work, we show that the sorbate-sorbate electrostatic interactions are essential for predicting the inflections and steps in the adsorption isotherms in this class of MOFs. All modeling results were obtained from grand canonical Monte Carlo (GCMC) simulations using a consistent set of force field parameters with no adjustable parameters. Full details are given in the *appendix D*.

*Figure 5.1* shows the results from two models compared with experiment for $CO_2$ adsorption in IRMOF-1 at 298 K. In the first model, only Lennard-Jones interactions are considered, ignoring the quadrupole moment of $CO_2$. This model predicts saturation loadings that are noticeably lower than experiment. The predicted isotherm also does not possess the inflection point seen in the experimental isotherm. The second model includes both Lennard-Jones and Coulombic interactions. It predicts the saturation loading in better agreement with experiment, and more importantly, it captures the inflection behavior. It should be noted that the inflection is captured without invoking any changes in the MOF structure itself. *Figure 5.1* clearly shows the importance of

electrostatic interactions between $CO_2$ molecules in capturing the shape of the experimental adsorption isotherm.

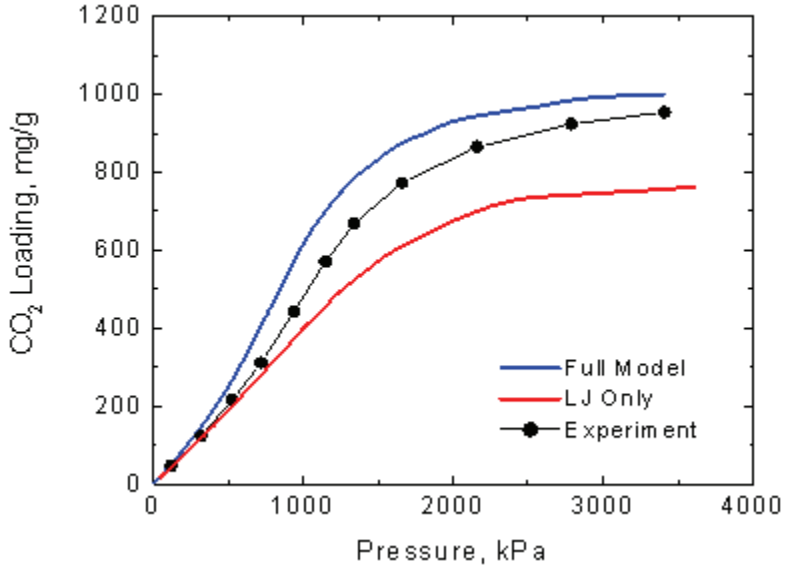


**Figure 5.1: Comparison of GCMC simulations and experimental adsorption isotherms for CO2 in IRMOF-1 at 298 K. The top curve was calculated from a model which included electrostatic effects. The bottom curve was calculated considering only the Lennard-Jones interactions.**

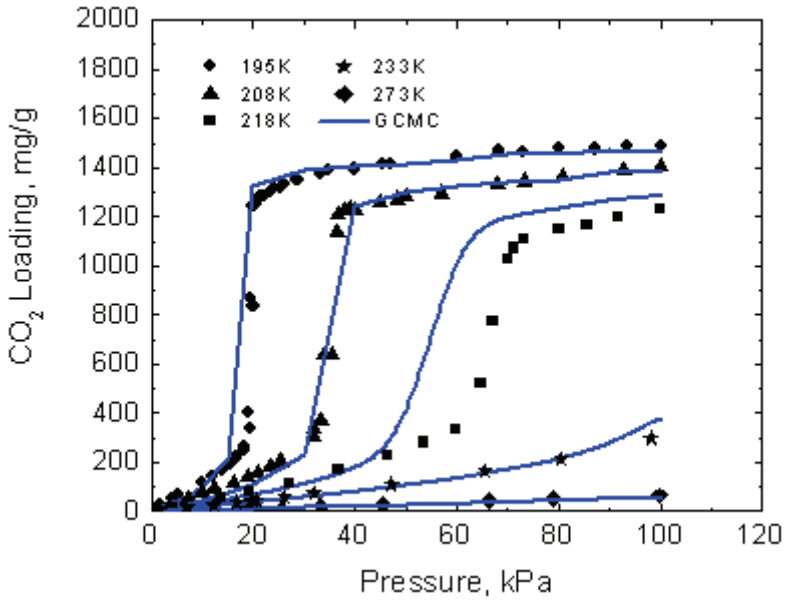


**Figure 5.2: Comparison of GCMC simulations and experimental adsorption isotherms for CO2 in IRMOF-1.**

Adsorption isotherms for $CO_2$ in IRMOF-1 over a wide range of temperatures are given in *Figure 5.2*[101]. The unusual inflection found in the room temperature isotherm (*figure 5.1*) grows into a very pronounced step at low temperature. Our molecular model provides excellent agreement with the experimental data. The model also works very well for predicting room temperature $CO_2$ adsorption in MOF-177 and IRMOF-3, as shown in *figure 5.3*. In agreement with experiments, the simulations show that the inflections in the isotherms become more defined with increasing effective pore size.

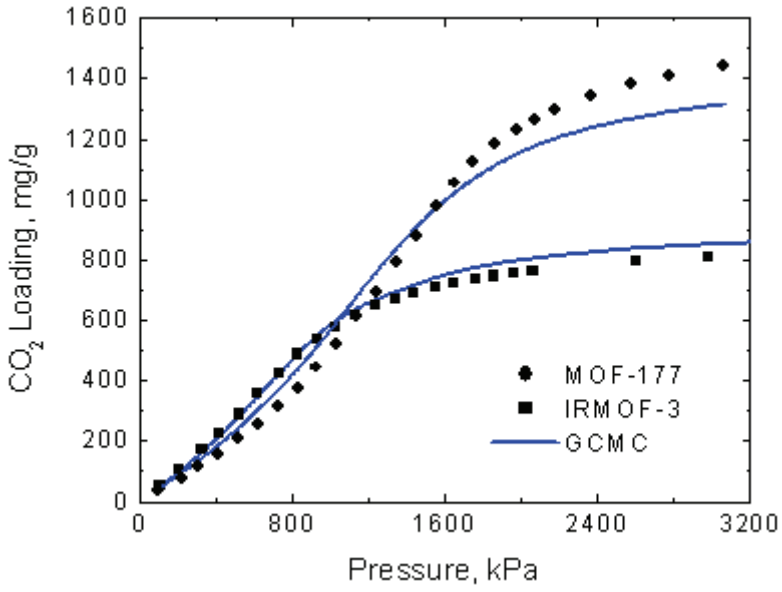


**Figure 5.3: Comparison of GCMC simulations and experimental adsorption isotherms for CO2 adsorption in MOF-177 and IRMOF-3 at 298 K.**

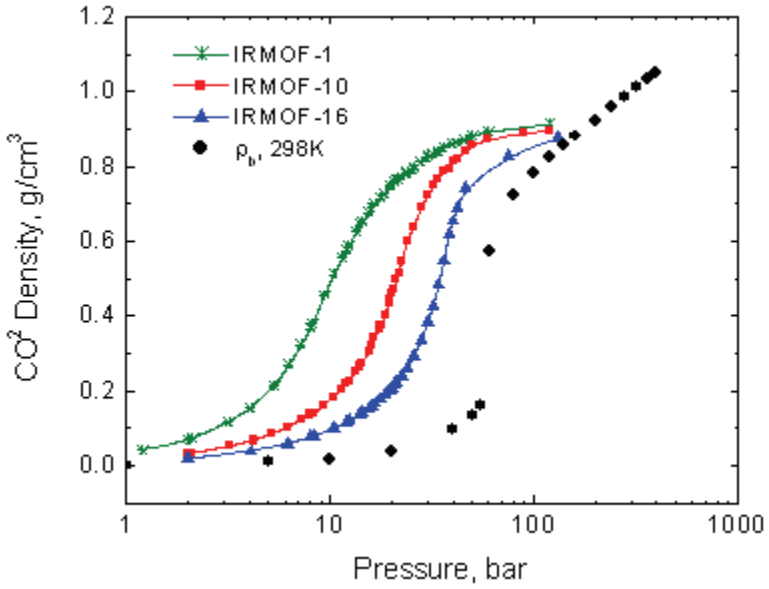


**Figure 5.4: Density of CO2 in IRMOF-1, -10, and -16 compared with bulk values at 298 K. The adsorbed-phase densities are calculated considering only the free volumes of the crystal structures.**

Analysis of the $CO_2$ positions reveals that below the sharp rise in the isotherms of *figure 5.2*, molecules are mostly adsorbed near the corners of the MOF cavities. With increasing pressure, the pores fill, leading to a type V isotherm[111]. Type V isotherms are relatively rare and are often accompanied by hysteresis[111]. However, neither the experiments nor the simulations display hysteresis. To shed more light on the pore filling, we plotted the density of $CO_2$ within the pore volume of IRMOFs-1, -10, and -16 at 298 K (*figure 5.4*). IRMOF-10 and IRMOF-16 possess approximately double and triple the pore volume per gram of IRMOF-1[17]. The bulk density of $CO_2$ as calculated from the Peng-Robinson equation is also shown in the figure. From these results, we find that the pressure of the pore filling shifts toward the bulk condensation pressure with increasing pore size (IRMOFs-1, -10, -16).

In summary, previously reported steps in the isotherms for $CO_2$ in MOFs were attributed to changes in the MOF crystal structure. However, for the MOFs of this study, we find that attractive electrostatic interactions between $CO_2$ molecules are responsible for the unusual shape of the adsorption isotherms. The isotherm shapes can be predicted by a molecular model using a rigid crystal structure. At 298 K, the pressure at which the pore filling occurs approaches the bulk condensation pressure with increasing pore size.

# Chapter 6: Carbon Dioxide Adsorption Behavior in Various Metal-Organic Frameworks

## *6.1: Introduction*

The adsorption of carbon dioxide within adsorbent materials has been under investigation for variety of reasons. Many studies focused on adsorption of $CO_2$ in order to characterize activated carbons and other carboneous materials[112-116]. Currently however, the attention has shifted to the use of adsorbents to capture $CO_2$ as well as in separation applications[100,108,117-121]. Metal-Organic Frameworks (MOFs) are a new and exciting class of porous materials that have great potential for separation technology including $CO_2$ separations and capture[9,100,104,107,108,120]. MOFs are crystalline materials with regular networks composed of organic molecules containing specific functionality that coordinate to metal or metal oxide corner units. The generic modular approach to synthesizing these materials allows for practically innumerable variations on the geometry and the chemical composition of these materials[1,8,16,20,47,82].

MOFs can be designed to have pore sizes over 2 nm and extremely large free volumes. This study elucidates how the large pore lengths and free volumes in these materials lead to interesting inflection behavior in the $CO_2$ adsorption isotherms that mimic the rapid density increase that is seen upon condensation of gaseous $CO_2$. The quick ramp resulting in the $CO_2$ density within these materials, specifically characterized as a Type V isotherm, has the potential to produce more efficient and effective separation technologies and materials with exceptional capacity at low pressures.

Numerous materials have been investigated for $CO_2$ adsorption, including a variety of zeolites, carbon fiber molecular sieves, activated carbons, metal oxide sorbents, and

Hydrotalcite-like compounds (HTlcs)[117-119]. In addition to these materials, Metal-Organic Frameworks (MOFs) have show great promise in $CO_2$ adsorption[100,104,108,120-122]. These materials displayed notably higher uptake of $CO_2$ adsorption than in previously studied materials as well as a deviation from the typical Type I shape of the isotherm. The fundamental difference between MOFs and the aforementioned materials are the large pore sizes and free volumes that can be manufactured with high consistency using the building block approach.

The exceptional uptake of $CO_2$ within these materials and unique isotherm shape (Type V) have been attributed to many aspects of the materials chemical and physical characteristics. While it is true that the presence of the material atoms (i.e. metal corners and organic linkers) provide strong interactions with the adsorbed $CO_2$ molecule, we believe the large void space within the material allows for the sharp increase (Type V) in $CO_2$ loading. Some groups have attributed interesting "step behavior" (which cannot be classified as Type V, as the isotherms display two inflection points) to framework changes, or a framework "breathing" mechanism[104,121,123]. In the material MIL-53 studied by Ferey et al.[104,121,123], it was found the structure changed from a narrow pore version, characterized by contorted pores due to hydrogen bonding, to a larger pore version, described as having more open porosity, as $CO_2$ loading is increased. In our previous work[124], it was determined that the large $CO_2$-$CO_2$ interactions are most likely the cause of the isotherms inflections. However, to allow for significant favorable sorbate-sorbate interactions, it is necessary to have sufficient void space within the material. In this work, numerous MOF materials with varying void volumes were investigated to support this hypothesis. In addition, simulations of $CO_2$ in hypothetical

MOFs, with extremely small void space, were performed. A number of the MOFs investigated can be seen in *figure 6.1*.

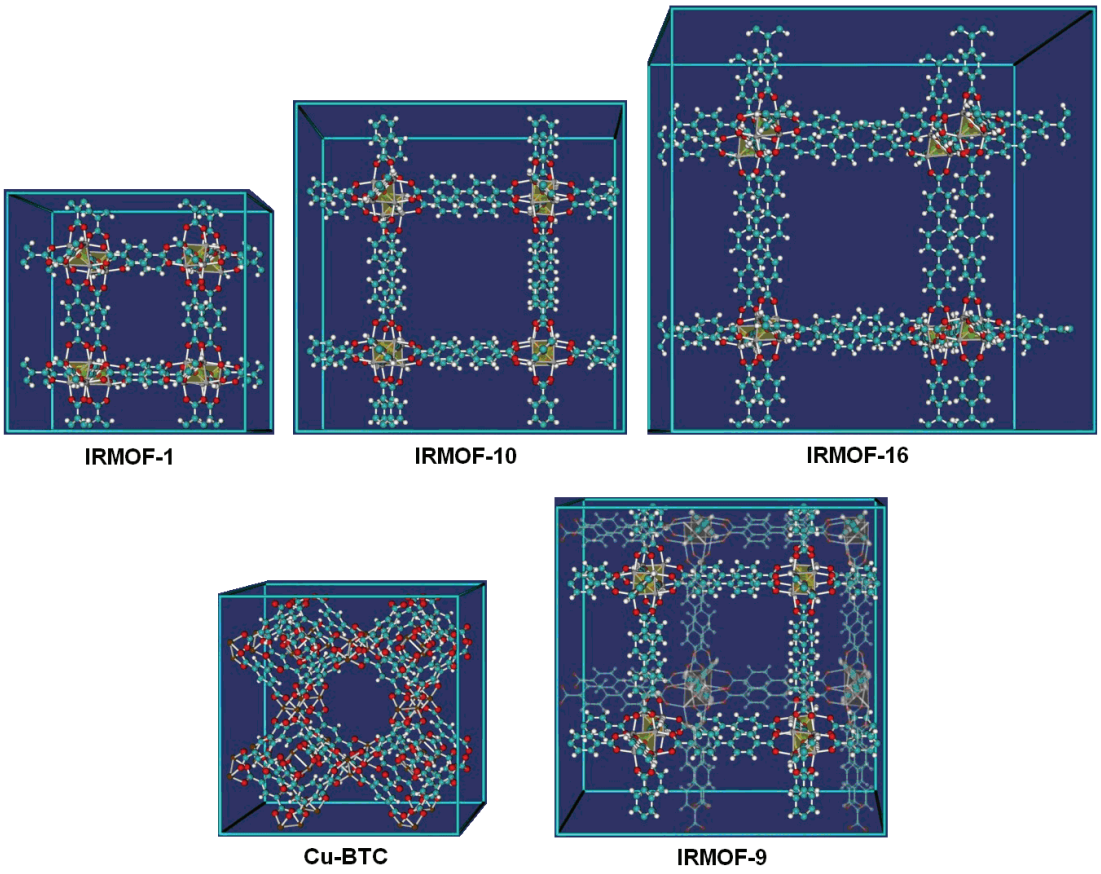


**Figure 6.1: IRMOF structures studied. Carbon atoms are shown as light blue, oxygen atoms are represented with red, hydrogen atoms are white, and zinc atoms are grey. The interpenetrated structure in IRMOF-9 has been made slightly transparent for easier viewing.**

The set of structures in *figure 6.1* has a large variety of pore sizes and free volumes. IRMOF-1 and 10 have two distinct pore sizes due to the "paddlewheel" arrangement of the organic linkers. More explicitly, the "paddlewheel" description refers to the alternating orientation of the phenyl ring plane, in one cage the phenyl rings point inward and in an adjacent cage they point outward. IRMOF-16 does not exhibit a "paddlewheel" type arrangement, and thus has only one pore size. Cu-BTC has a fundamentally

different structure as compared to the IRMOFs, because the organic linker has three coordinating functional groups (as opposed to two in the IRMOFs). All three carboxylate groups coordinate to $Cu^{+2}$ dimers, which serve as the metal corner units. This leads to a structure with two significantly different pore sizes, the main channels have a diameter of 9 Å, and these are surrounded by tetrahedral side pockets with diameters of 5 Å. Finally, IRMOF-9 is an interwoven form of IRMOF-10, where a second structure is catenated within the first. Since this structure has an alternating "paddlewheel" configuration, and the interwoven form is where the catenated structures are minimally displaced, IRMOF-9 contains four different pore sizes. The exact pore diameters are discussed further in the results section, and can be found in *table 6.1*.

To extend the range of free volumes, pore sizes, and geometries studied, 4 additional hypothetical structures were produced from the original IRMOF-10 and 16 structures seen in *figure 6.1*. The structure designated as IRMOF-10-2 is a two-fold interpenetrated form of the original. Much like IRMOF-9, which is the interwoven form of IRMOF-10, IRMOF-10-2 has a second structure catenation. The difference between the two catenated structures IRMOF-10-2 and IRMOF-9 is the structures are maximally displaced (this is referred to as interpenetrated) in IRMOF-10-2, as opposed to minimally displacement (referred to as interwoven) in IRMOF-9. IRMOF-10-3 has a third catenation where all three structures are maximally displaced (interpenetrated). Similarly IRMOF-16-2 is a structure with two-fold interpenetration and IRMOF-16-3 has three-fold interpenetration.

### *6.2: Simulation methods*

$CO_2$ adsorption within the MOF materials was simulated with GCMC[51,52] using our multipurpose simulation code Music[53]. Each step in the Monte Carlo routine consisted of the insertion of a new molecule, deletion of an existing molecule, translation, or rotation of an existing molecule. A total of 20 million steps were used, the first 75% for equilibration and the last 25% to calculate the ensemble averages. Gas-phase fugacities were calculated with the Peng-Robinson equation of state. The material was considered rigid with atoms positioned according to the crystallographic data[15-17,87]. The MOFs and carbon dioxide molecules were represented in atomistic detail. $CO_2$-$CO_2$ interactions were modeled using the TraPPE potential[125]. This model places a Lennard-Jones center on each carbon and oxygen atom, a point charge of +0.70 on the center of mass of the carbon atom, and a charge of -0.35 on each oxygen atom to simulate the molecule's quadrupole moment. The C-O bond length is 1.16 Å, and the bond angle is 180º. The Lennard-Jones parameters for the framework atoms were taken from the DREIDING force field[56], except for the copper atom which was taken from the Universal Force Field (UFF)[89]. Lorentz-Berthelot mixing rules were employed to calculate sorbate/framework parameters. Lennard-Jones interactions beyond 12.8 Å were neglected. This method was used successfully in our previous work[124].

Electrostatic charges for the MOF framework atoms were calculated using the quantum chemical package Gaussian03[35]. DFT was employed for the model chemstry, specifically the exchange and correlation functional by Perdew, Burke, and Ernzerhof[126,127]. An adequate modest basis set of 6-31+g* was used, which includes one diffuse and one polarization function on atoms heavier than He. The CHelpG method[128]

was used to calculate charges from the DFT results and atomic radii were obtained from Bondi[129]. Similar methods have been employed to estimate charges and study binding energies in MOFs[57,70,107,108,130,131]. Representative clusters were chosen for each material. This cluster consisted on one of the organic linker molecules coordinated to the metal oxide unit on both sides. The metal oxide was terminated with methyl groups where the other organic linkers would normally exist. An example (IRMOF-1), can be seen in *figure 6.2* below. The clusters were used to provide atomic charges for both the organic unit, as well as the metal corner.

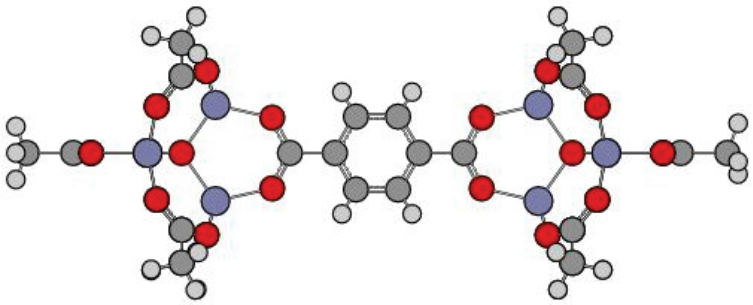

**Figure 6.2: Representative cluster for charge calculation for IRMOF-1.**

Free volumes or void fractions were calculated in the same method used in our previous study of hydrogen adsorption[79]. Pore diameters were determined from the crystal structure using the method discussed by Duren et al.[42]

## *6.3: Results and discussion*

### *6.3.1: Comparison with experiment and effect of framework charges*

The purpose of this study is to evaluate the behavior of $CO_2$ adsorption in a variety of materials. A number of previously studied sorbents exhibit standard Type I isotherm behavior with $CO_2$ adsorption. Many MOF materials however show the presence of an

inflection in the isotherm, leading to a sharp increase in the uptake as pressure increases. $CO_2$ adsorption at 298K in several MOF materials covering a wide range of free volumes and pore diameters were investigated.

The model used in simulating $CO_2$ adsorption provided excellent agreement with a variety of MOF materials over a range of temperatures in our previous study[124]. In this study however, we added the effect of MOF framework charges. These charges were calculated as per the method mentioned previously, and the charge results are presented following the adsorption results. A comparison between experimental $CO_2$ adsorption in IRMOF-1 at 298K from Millward[101], and two sets of simulation results can be seen in *figure 6.3* below. The solid curve displays the isotherm resulting from simulations where MOF-$CO_2$ electrostatic interactions were included (i.e. MOF atomic charges were used). The dashed curve shows the results without including MOF-$CO_2$ electrostatic interactions (these results were reported in our previous study[124]). *Figure 6.3a* displays that at low pressures the model including MOF-$CO_2$ electrostatic interactions agree better with the experimental data. However, in *figure 6.3b* it is evident that these electrostatic charges make little difference as the $CO_2$ uptake is only slightly higher. Yang et al.[108] describe the importance of MOF electrostatic effects in selectivity in their studies of carbon dioxide and methane mixtures.

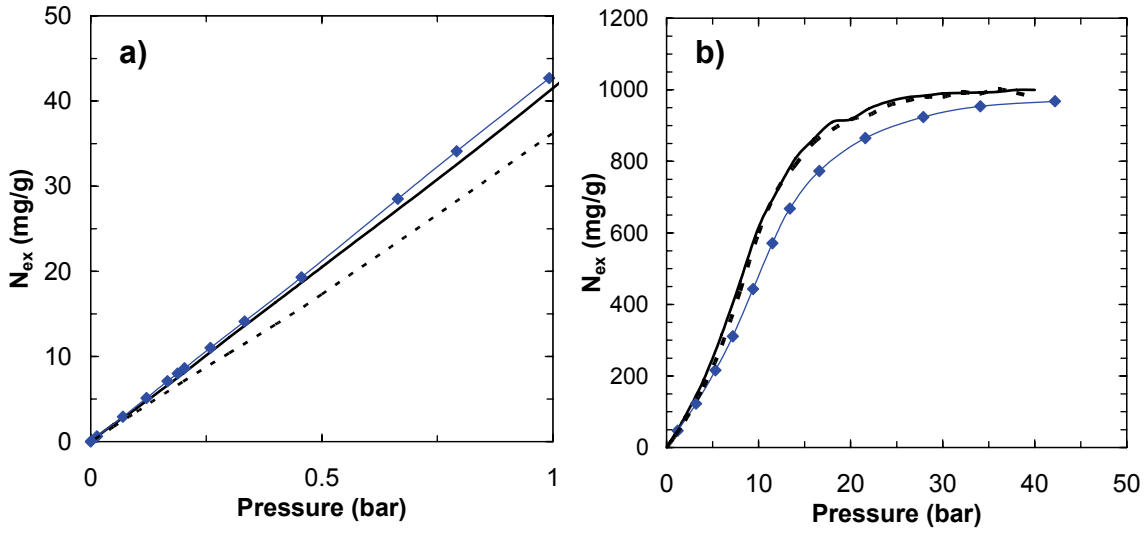


**Figure 6.3: Experimental and simulated $CO_2$ isotherms in IRMOF-1 at 298K. Solid curve – simulations including MOF-$CO_2$ electrostatic interactions; dashed curve – simulations without MOF-$CO_2$ electrostatic interactions; ◆ - experimental data.**

*6.3.2: Effect of pore geometry on inflections*

In addition to IRMOF-1, we simulated $CO_2$ isotherms in IRMOF-9, 10, 16, and Cu-BTC. We also investigated four hypothetical materials, IRMOF-10-2, 10-3, 16-2, and 16-3, which were described in detail in the introduction. We created IRMOF-10-2 a doubly interpenetrated form of IRMOF-10, to compare $CO_2$ adsorption behavior to that found in the doubly interwoven form IRMOF-9. The triply interpenetrated IRMOF-10-3 was investigated to observe $CO_2$ adsorption behavior in a material with extremely restrictive pore sizes and a comparably low void fraction. IRMOF-16-2 and 16-3 were created to provide a range of pore sizes in a material which does not have an alternating, "paddlewheel" configuration. The resulting isotherms (absolute adsorption in a gravimetric basis), can be seen in *figure 6.4*.

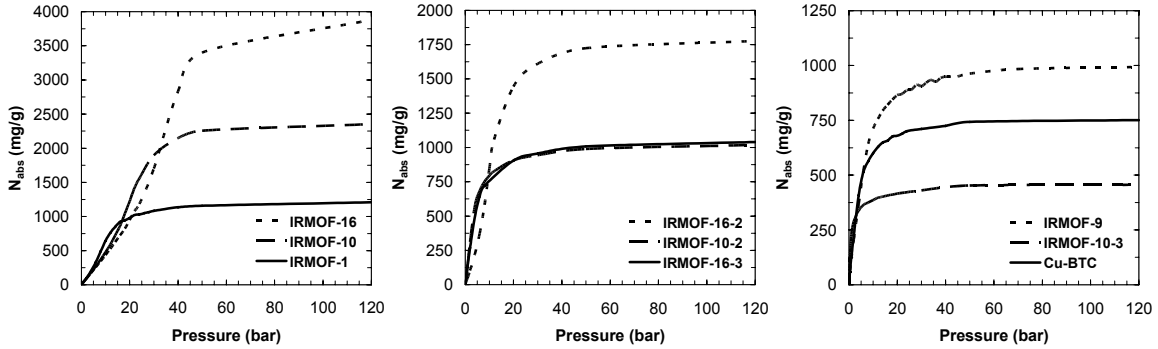


**Figure 6.4: $CO_2$ adsorption isotherms at 298K in nine previously synthesized and hypothetical materials.**

It is evident that inflections exist in the isotherms from IRMOF-1, 10, 16, and 16-2. An inflection point also exists in IRMOF-10-2 and 16-3, however at such low pressures they are difficult to visualize. There is no inflection behavior apparent in Cu-BTC, IRMOF-9, and IRMOF-10-3. Rather, the isotherms represent standard Type I behavior. *table 6.1* below lists the materials along with the corresponding pressure and percent of loading the inflection takes place (i.e. the point at which the 1st derivative begins to decrease). Material properties including void fraction and pore diameters are also listed.

**Table 6.1: Pressure and loading at which the inflection point takes place in CO2 isotherms in nine materials.**

| Material | Pressure (bar) | % Loading | Void Fraction | Pore Diameter 1 (Å) | Pore Diameter 2 (Å) | Pore Diameter 3 (Å) | Pore Diameter 4 (Å) | Average Pore Diameter (Å) |
|---|---|---|---|---|---|---|---|---|
| **IRMOF-16** | **40** | **0.73** | **0.90** | 23.3 | n/a | n/a | n/a | **23.3** |
| **IRMOF-10** | **22** | **0.66** | **0.86** | 16.7 | 20.2 | n/a | n/a | **18.5** |
| **IRMOF-1** | **10** | **0.53** | **0.78** | 10.9 | 14.3 | n/a | n/a | **12.6** |
| **IRMOF-16-2** | **10** | **0.59** | **0.81** | 4.3 | 7.3 | 9.1 | 10.9 | **7.9** |
| **IRMOF-10-2** | **2** | **0.33** | **0.72** | 4 | 5.1 | 5.9 | 7.9 | **5.7** |
| **IRMOF-16-3** | **0.2** | **0.03** | **0.71** | 3.7 | 4.7 | 5.7 | 7.7 | **5.5** |
| **IRMOF-9** | no inflection | no inflection | **0.72** | 4.5 | 6.3 | 8.1 | 10.7 | **7.4** |
| **IRMOF-10-3** | no inflection | no inflection | **0.58** | 3.1 | 5.3 | n/a | n/a | **4.2** |
| **CuBTC** | no inflection | no inflection | **0.70** | 9 | 5 | n/a | n/a | **7.0** |

*** Percent loading was calculated as the percent of loading at max pressure (120 bar)**

This table clearly indicates that the pressure (and also the % loading) at which the inflection in the isotherm takes place is dependent on the void fraction of the material.

The dependency on pore diameter is also evident; however the trend is less consistent. This is most likely due to the various geometries within the materials. The three materials that do not show inflection behavior all have void fractions of less than 0.72. While IRMOF-10-2 and 16-3 have void fractions of 0.72 and 0.71 respectively, there inflections take place at extremely low pressure.

The comparison between IRMOF-9 and 10-2 is of special interest as these materials are nearly identical except for the position of the catenated structure. IRMOF-9 is an interwoven material, while IRMOF-10-2 is an interpenetrated structure. Interestingly, IRMOF-9 does not exhibit inflection behavior in the $CO_2$ isotherm but IRMOF-10-2 does. Both materials have identical void fractions, clearly indicating that the occurrence of an inflection is due to the specific geometry of the material as well as the availability of void space. An important difference between the two materials is in IRMOF-9 the phenyl rings of the two catenated structures are perpendicular to one another, while in IRMOF-10 they are parallel.

Concentrating on the average pore diameters, *table 6.1*, also indicates that a material with an average pore diameter of greater than 8Å produces an inflection in $CO_2$ adsorption behavior. However, materials with average pore diameters as small as 5.5Å also produced inflection containing isotherms, and some materials with pore diameters of 7Å failed to display inflection behavior. Again, this clearly indicates that while void fraction and average pore diameter are important characteristics to produce inflections, other specific geometric issues are also important.

$CO_2$ in many other materials have been studied, nearly all do not exhibit inflection behavior in their $CO_2$ isotherms. Zeolite 13X and Zeocarbon, as reported in Lee et al.[119],

both show typical type I $CO_2$ adsorption behavior, at a variety of temperatures around 298K. Zeolite 13X is reported to have a void fraction of 0.17 ; the Zeocarbon material is reported with a void fraction of 0.10. The absent of inflection behavior in these materials with low void fractions is consistent with our results.

Various activated carbons, carbon fibers, and carbon molecular sieves studied by Cazorla-Amorós el al.[113,114] also exhibit type I behavior. In a review by Yong et. al[117], numerous activated carbons, commercially available MAXSORB materials, carbon fiber molecular sieves, metal oxide sorbents, and Hydrotalcite-like compounds (HTlcs) all were shown to have type I behavior. Macario et al.[132] tested various mesoporous material sieves in pure silica form with differing pore sizes to again find the presence of Type I adsorption behavior. The $CO_2$ results in the material MCM-41, also mesoporous, indicate that inflection behavior will not be observed.[133]

It is postulated that the absence of inflection behavior in many of these materials is due to the lack of void space, as materials with large void volumes allows for the substantial $CO_2$-$CO_2$ interactions which are beneficial for $CO_2$ uptake. One interesting study on micropore size distribution displays $CO_2$ adsorption in slit pores of various widths, slit pores larger than 1.05nm do in fact exhibit an inflection, while smaller width pores do not[115]. While this conclusion is not mentioned in the study, it is further confirmation that materials with larger space between adsorbent walls allow for increased favorable sorbate-sorbate interactions which was attributed to the inflection behavior in our previous study[124].

However, this explanation doesn't work for the mesoporous materials mentioned that also were reported to show Type I behavior in $CO_2$ adsorption. One possibility for the

absence of inflection in these, often more disordered materials is the wide distribution of pore sizes. This potentially could create an effect where rapid increases in $CO_2$ uptake in some regions of the material are "averaged-out" by slower uptake in other regions of the material.

### *6.3.3: Investigation of $CO_2$ density within MOFs and the system interaction energies*

Several MOF materials provide $CO_2$ isotherms that show a sharp increase (and inflection behavior) in $CO_2$ density adsorbed within the material. This sharp increase in density is quite similar to pure $CO_2$ gaseous behavior as $CO_2$ liquefies, which occurs at 64.3 bar at a temperature of 298K[134]. In *figure 6.5* we have plotted the density of $CO_2$ adsorbed vs. pressure for a selection of the MOFs studied. Please note that the pressure is plotted on a log scale, and the materials IRMOF-10-3, IRMOF-9, and Cu-BTC which do not exhibit inflection behavior on a normal scale, appear with an "s-shape" in this plot due to the log scale.

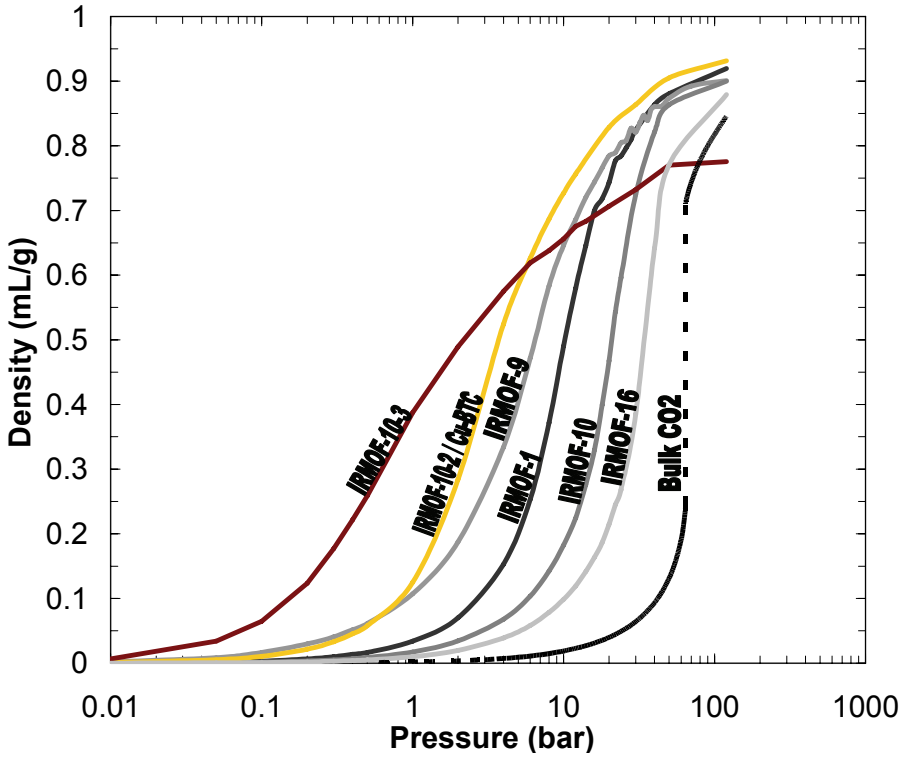


**Figure 6.5: Density of CO2 within various MOF materials (NOTE: pressure in log scale). **IRMOF-10-2 and Cu-BTC had nearly identical curves as plotted on this scale.**

*Figure 6.5* clearly shows that $CO_2$ density within the pores of all the materials reach the magnitude of bulk liquid $CO_2$ at 298K and 64.3 bar, which is 0.75 g/mL[134]. Further, $CO_2$ within these materials reach the liquid density at much lower pressures. At higher pressures, the density of $CO_2$ within the materials even exceeds bulk $CO_2$ density[134]. Further, the materials that do not exhibit inflection behavior in *figure 6.2*, also reach liquid like densities within the pore volume. Thus, the inflection behavior is not necessary for high $CO_2$ adsorbed densities, but it does alter the sensitivity of $CO_2$ loading as a function of pressure which may have significant importance if these materials are to be used in separation processes.

*Figure 6.6* displays the potential energy contributions from $CO_2$-$CO_2$ interactions and $CO_2$-MOF interactions. These have also been separated into the Lennard-Jones and Coulombic contributions.

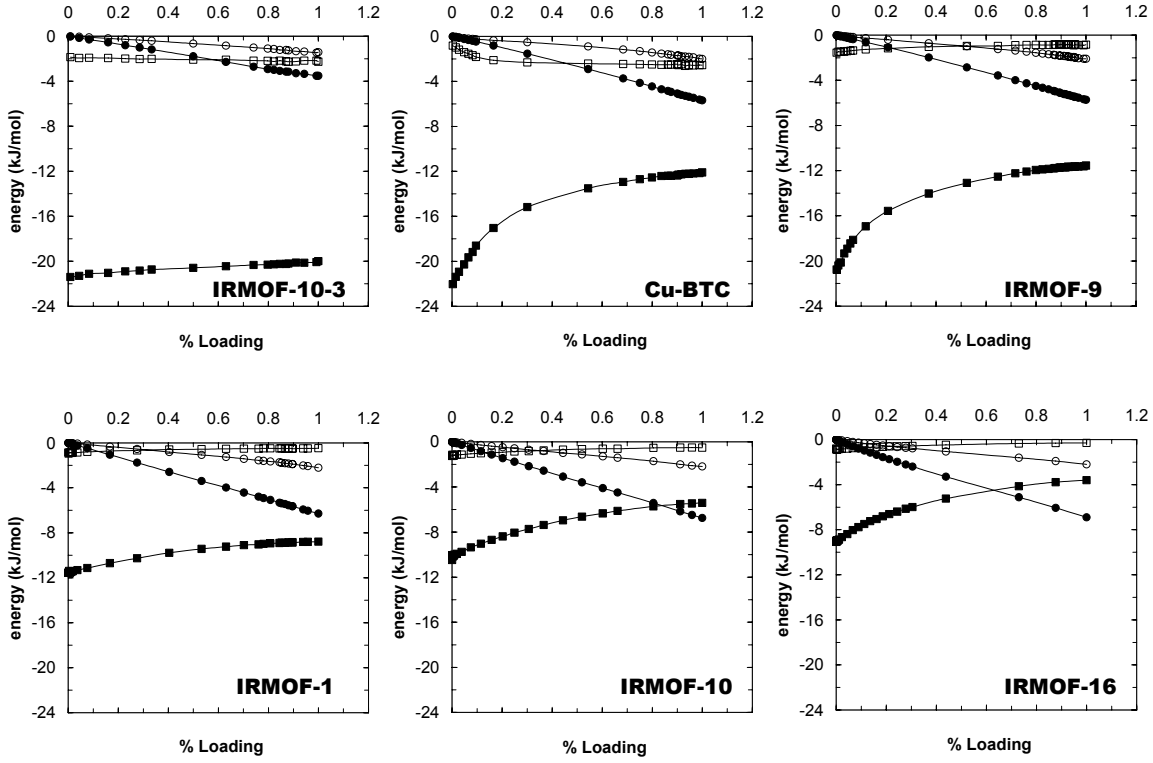


**Figure 6.6: Potential energy contributions for adsorption in six MOFs vs. extent of loading. ● - $CO_2$-$CO_2$ interaction energy (Lennard-Jones); ■ - $CO_2$-MOF interaction energy (Lennard-Jones); ○ - $CO_2$-$CO_2$ interaction energy (Coulombic); □ - $CO_2$-MOF interaction energy (Coulombic).**

*Figure 6.6* clearly indicates that as the pore size decreases and free volume is limited, the $CO_2$-MOF interaction from both the Lennard-Jones and Coulombic contributions is greatly increased, as expected. In IRMOF-10-3 and Cu-BTC the $CO_2$-MOF Coulombic contributions is greater than the $CO_2$-$CO_2$ Coulombic contribution over the entire range of loading. This highlights the importance of including these interactions. In the other materials the $CO_2$-MOF Coulombic contribution is important at low loadings, but ultimately the $CO_2$-$CO_2$ Coulombic interactions provide a greater energetic contribution

(this is easily seen from the crossing of the two curves following the Coulombic interactions, the open symbols).

The $CO_2$-$CO_2$ Lennard-Jones energies are also of particular interest. It is evident that this contribution is larger in IRMOF-1, 10, and 16, three materials that display inflections in the isotherms, than in IRMOF-10-3, Cu-BTC, or IRMOF-9, three materials that do not display inflections in the isotherms. The $CO_2$-$CO_2$ Lennard-Jones energies are in fact larger than the $CO_2$-MOF Lennard-Jones contribution at high loadings in IRMOF-10 and 16 (this can be seen from the crossing of the two curves following the Lennard-Jones interactions, the solid symbols). These graphs display that the smaller pore sizes and void volumes in these materials inhibit the extent of the $CO_2$-$CO_2$ interactions energies. The lack of inflection behavior here can be directly attributed to the lower $CO_2$-$CO_2$ interaction energies caused by the restrictive pore volumes.

### *6.3.4: Development of a generic set of MOF charges*

Charges for MOF framework atoms were calculated using the aforementioned method for a variety of materials including IRMOF-1, 2, 3, 4, 5, 6, 7, 8, 9/10, 11/12, 13/14, 15/16, and Anthracene. Charges were also calculated for MOF-177 and Cu-BTC. The raw results for the charges, along with the corresponding structures, can be found in *appendix E*.

*Figure 6.7* and *table 6.2* displays the charges that were employed for Cu-BTC. Since the quantum calculations were performed on finite clusters, these charges were slightly altered from the raw data to ensure neutrality in the entire unit cell of the material. Similar charges for Cu-BTC were reported by Yang et al.[107]

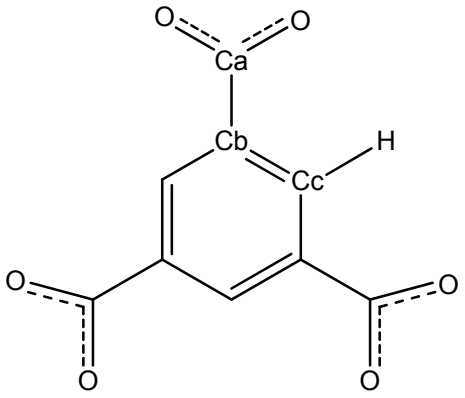


**Figure 6.7: Key for Cu-BTC charges.**

**Table 6.2: Atomic charges used for Cu-BTC.**

| Atom | Cu-BTC atom charges |
|---|---|
| Cu | 1 |
| O | -0.6 |
| Ca | 0.7 |
| Cb | 0 |
| Cc | 0.15 |
| H | -0.15 |

*Figure 6.8* displays a key for the generic charge set, using 1,4-benzenedicarboxylic acid as the template molecule. The corresponding charges can be seen in *table 6.3*. Similar charges were reported by Yang et al.[107] and Sagara et al.[57] for IRMOF-1. These charges were found to be relatively consistent for similar atoms in all other IRMOF materials investigated. The error listed in *table 6.3* is the standard deviation of the charges found for analogous atoms in the various IRMOFs studied (again raw data for other materials can be found in *appendix E*). We believe that these charges can be used generically for atoms in chemically similar environments in the $Zn_4O$ based IRMOF materials. For example, the Zn and Oa atomic charge can be used for the $Zn_4O$ tetrahedral corner unit in any IRMOF. Further, the charge listed for the oxygen atom Ob,

can be used for a carboxylate oxygen in any IRMOF material. Similarly the charge on the carbon atom, Ca, can be used for a carboxylate carbon generically in IRMOF materials. The atom Cb, can be used generically for the phenyl ring carbon attached to the carboxylate anion. It is somewhat more difficult to assign a generic charge to any phenylic carbon, such as Cc. It is evident from *table 6.3* that in comparing similar atoms across the range of materials, the error or standard deviation is large. However, the bulk of the electrostatic charge of the materials is found on the metal corners and the carboxylate anion that coordinates to these corners. The remaining organic atoms are much less polarized.

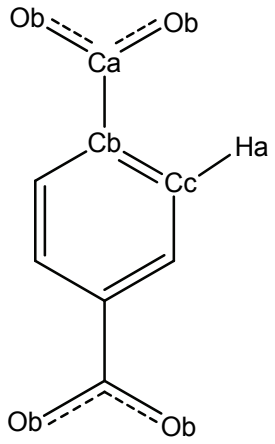


**Figure 6.8: Key for generic charges using 1,4-benzenedicarboxylic acid as a template molecule.**

**Table 6.3: Atomic charges proposed for generic Zn4O MOFs.**

| Atom | Generic MOF atom charges | error |
|---|---|---|
| **Zn** | **1.3** | +/- 0.1 |
| **Oa** | **-1.6** | +/- 0.1 |
| **Ob** | **-0.6** | +/- 0.1 |
| **Ca** | **0.5** | +/- 0.2 |
| **Cb** | **0.1** | +/- 0.2 |
| **Cc** | **-0.15** | +/- 0.3 |
| **Ha** | **0.15** | +/- 0.1 |

### *6.4: Conclusion*

Interesting inflection behavior is observed in $CO_2$ isotherms at 298K in a number of MOF materials. The inflection behavior, attributed to the extensive $CO_2$-$CO_2$ interactions, is more prominent in materials with larger void fractions and free volumes. In fact, materials with tight geometries (small pores and void spaces), do not exhibit any inflection behavior, as the $CO_2$-$CO_2$ interactions are not prominent enough to produce the sharp increase in adsorption loading. A quick review of $CO_2$ adsorption in a variety of other materials, as well as energy analysis in the materials investigated in this study, supports this hypothesis.

The density of $CO_2$ with MOFs is able to reach and exceed bulk liquid $CO_2$ density at 298K, and at pressure lower than 64.8 bar (where bulk $CO_2$ condenses). The pressure at which $CO_2$ density within the materials reaches liquid like levels is dependent on material geometry.

MOF charges were calculated for a variety of materials, and it was determined that many atoms in chemically analogous environments were quite consistent; this led to the determination of a generic set of charges for a select group of MOF atoms.

The inflection behavior and large density of $CO_2$ within MOF materials at low pressure lends the materials to light gas separation processes. More studies should be done to evaluate the possibility of using these materials in adsorptive separation applications

# Chapter 7: Carbon Dioxide and Methane Mixtures in a Paddlewheel MOF

## *7.1: Introduction*

The interest in $CO_2$ adsorption in Metal-Organic Frameworks is two-fold. The high density of $CO_2$ found to absorb within these materials at relatively low pressures potentially could be utilized in $CO_2$ capture applications, as well as in separation applications where the removal of $CO_2$ from mixtures of products such as methane is necessary to produce a high quality and pure fuel product. In this study we examine the ability of one MOF, namely $Zn_2$(2,6-naphthalenedicarboxylic acid)( N,N'-di(4-pyridyl)-1,4,5,8-naphthalenetetracarboxydiimide) or more simply "Hupp-4," to separate $CO_2$ and $CH_4$ mixtures[18].

The material investigated in this study, Hupp-4, is one of a series of mixed-ligand pillared paddlewheel MOFs synthesized by Hupp et al.[18,86] The description elucidates the fact that two different organic ligands are utilized in the framework. These ligands are coordinated to Zn(II) dimers that serve as the corners of the framework. In Hupp-4, which can be seen in *figure 7.1*, the N,N'-di(4-pyridyl)-1,4,5,8-naphthalenetetracarboxydiimide ligands serve as the "pillars" of the structure and are in between "sheets" of the 2,6-naphthalenedicarboxylic acid ligands.

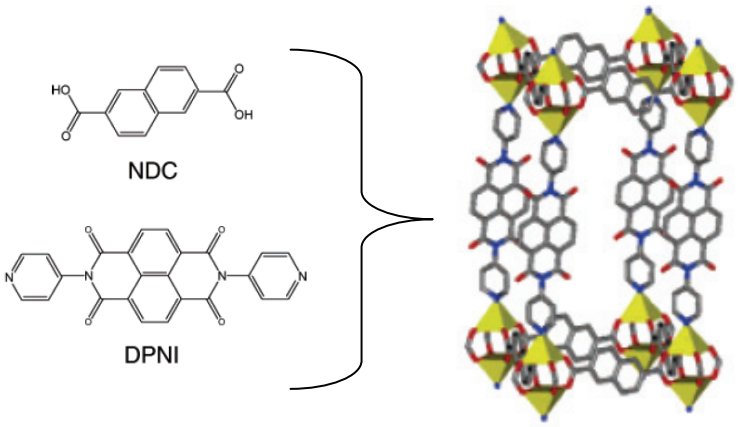


**Figure 7.1: The ligands and framework structure of Hupp-4.**

### *7.2: Simulation methods and Ideal Adsorbed Solution Theory (IAST)*

Carbon dioxide and methane adsorption was modeled in the material using GCMC[51,52] and our multipurpose simulation code Music[53]. The material was considered rigid with coordinates from Ma et al.[18] We modeled dispersion interactions using the Lennard-Jones equation (eq. 3.3). The Lennard-Jones parameters for the framework atoms are from the DREIDING force field[56], the $CO_2$ parameters came from the TraPPE potential[125], and the methane parameters are from Goodbody et al.[135] The rigid framework and the mobile $CO_2$ molecules were modeled atomistically, while the methane molecules were considered as united atoms. The Lorentz-Berthelot mixing rules were employed for all mixed parameters. In addition to the Lennard-Jones potential, we also modeled $CO_2$-$CO_2$ Coloumbic interactions using partial charges on the atoms to mimic the quadrupole moment on $CO_2$, these values are also from TraPPE[125]. No charges were given to the framework atoms in this study.

Simulations were done for both single component adsorption of $CO_2$ and $CH_4$ separately, as well as for a variety of mixtures. GCMC uses the grand canonical

ensemble to represent the system, thus we have a fixed chemical potential (μ), volume (V), and temperature (T). To determine the isotherms or the adsorption loadings at various pressures, the corresponding bulk phase fugacities (or chemical potentials via the standard thermodynamic relationship) are required. The pure component and mixture fugacities were calculated using the Peng-Robinson equation of state.

Experimental adsorption isotherms were also measured. This was done using a volumetric system developed in the group that measures small pressure differences to determine the amount adsorbed once a known amount of gas is exposed to the absorbent material. The experiments were carried out by Yong-Sang Bae.

The study enabled testing of the applicability of the Ideal Adsorbed Solution Theory (IAST), by comparing the predicted mixture isotherms using the pure component simulations and IAST with the isotherms determined in the mixture simulations.

The IAST is a simplified case in a treatment of the concept by Myers and Prausnitz[136] that considers a mixed adsorbate as a solution in equilibrium with the gas phase[27,30]. This theory allows for the determination of mixture isotherms from the pure component isotherms. A rigorous outline of the theory can be found in[27,30]. However, ultimately using the ideal assumption allows for activity coefficients to be unity, and the spreading pressure being identical for both species and the mixture. Once the spreading pressure is determined via the integration of the single component isotherms, adsorption loadings that would be found in an ideal mixture can be obtained.

In order to integrate the single component isotherms, an isotherm model such as Langmuir's can be fit to the numerical data obtained via simulations or experiments. Alternatively, one can numerically integrate this data. In this study the TOTH isotherm

equation was used as it provided the best fit to both simulation and experimental data. The TOTH equation[137] is:

$$N = N_{sat} \frac{bP}{(1 + bP^t)^{1/t}} \tag{7.1}$$

where N is the adsorption loading or concentration in arbitrary units (the same units that are used for $N_{sat}$, the saturation or max loading), b and t are parameters specific to the adsorbate-adsorbent pair, but t is usually less than unity and is said to characterize the system heterogeneity (as it deviates from unity, it indicates a greater degree of heterogeneity). Personally, I think it's just another equation with 3 degrees of freedom that fits isotherm behavior well, truly providing little insight into adsorption behavior.

### *7.3: Results and Discussion*

The results from simulated and experimental pure component $CO_2$ and $CH_4$ isotherms can be seen in *figure 7.2* below.

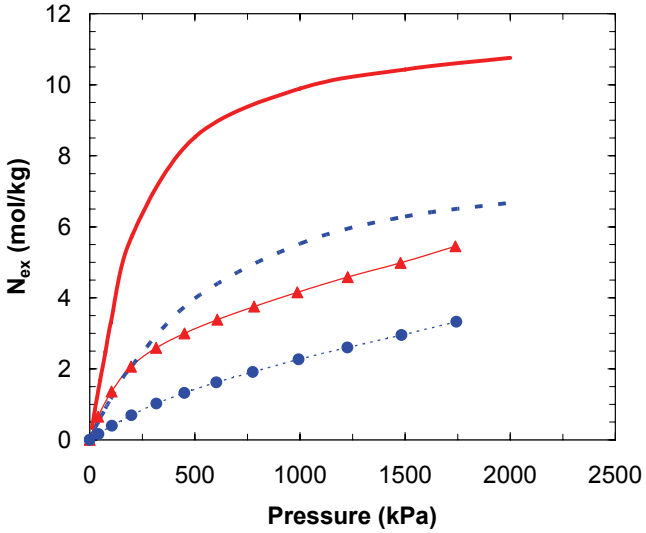


**Figure 7.2: Comparison of simulated and experimental pure component CO2 and CH4 isotherms in Hupp-4 at 298K. ▲-$CO_2$ experiment; ●-$CH_4$ experiment; solid curve-$CO_2$ simulation; dashed curve-$CH_4$ simulation.**

The simulation results show significantly more uptake for both $CO_2$ and $CH_4$. While it is possible that the model used is in error, it seems unlikely, as the same model very accurately predicted $CO_2$ adsorption in a variety of MOF materials at the same temperature in Chapters 5 and 6 of this document. Further, the model used for methane adsorption was successfully used in Düren et al.[42] Therefore, we believe the error to be on the experimental end. More specifically, it is thought that the material sample used in the experiments do not match the perfect crystal structure that is used in the simulation.

To test this theory we attempted altering the simulation to try and match experiment. First, a new hypothetical structure was derived from the original coordinates. The original structure from XRD was found to be doubly interwoven (thus the *figure 7.1* is not the exact crystal structure determined experimentally, it has a second identical structure interwoven). We created additional catenation within the original to create a hypothetical triply catenated material. It was possible the material studied experimentally was not purely the doubly interwoven form, but rather a material with a greater extent of catenation. Increasing catenation essentially decreased the free volume per mass of the material by increasing the density of framework atoms, and this should lower the magnitude of the isotherms. The simulation results of adsorption within this new structured as compared to the originally used experimental data can be seen in *figure 7.3*.

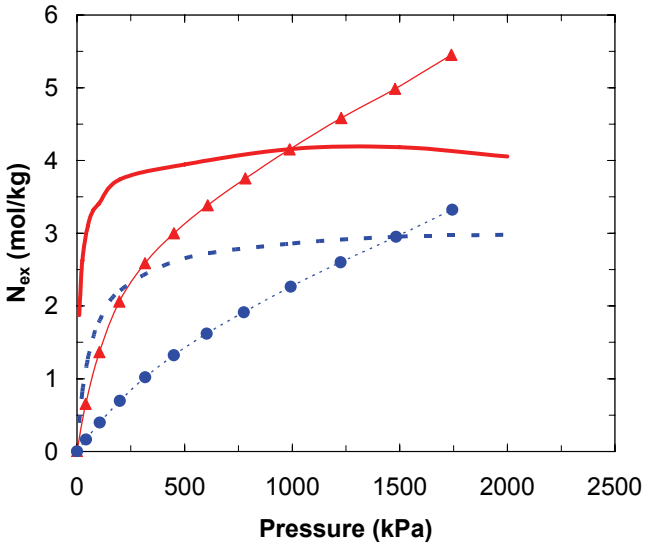


**Figure 7.3: Comparison of simulated and experimental pure component CO2 and CH4 isotherms in the hypothetical triply catenated Hupp-4 structure at 298K. ▲-$CO_2$ experiment; ●-$CH_4$ experiment; solid curve-$CO_2$ simulation; dashed curve-$CH_4$ simulation.**

While the magnitudes of the simulated and experimental isotherms are similar for this structure, the shapes of the isotherms are very different. The simulation data show a much sharper increase in adsorption density at low pressures. This is due to the enhanced interaction energy or heat of adsorption created by adding additional adsorption surfaces in the simulated structure.

This lead to an alternate idea that the Hupp-4 material used in the experiments had solvent blocking pore volume or adsorption sites as opposed to having a fundamentally different structure. This solvent would block adsorption sites, decreasing free volume, but not increase the interaction energy between the material and adsorbate as was seen in the triply catenated structure. To test this theory we simply scaled the original simulated isotherm by the ratio of free volume that was determined experimentally (0.34 $cm^3/g$) via the Dubnin-Radushkevich equation[30] (see Chapter 1, Section 1.2.3 for a short discussion) to the free volume calculated from the perfect crystal structure (0.878 $cm^3/g$). The results

of the scaled simulated data as compared to the original experimental data can be seen in *figure 7.4*.

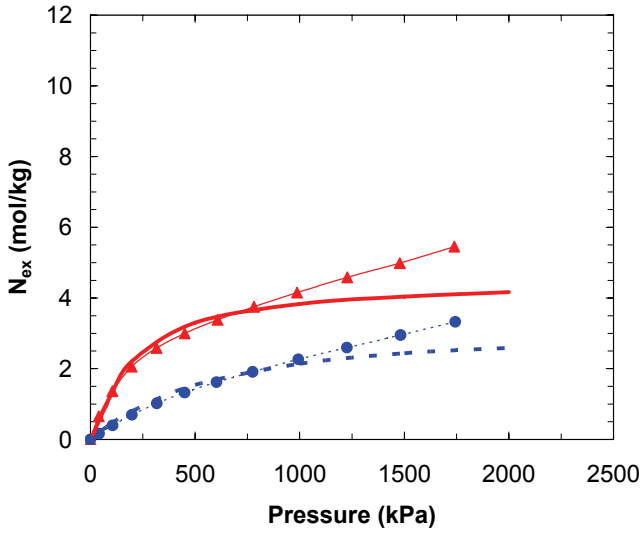


**Figure 7.4: Comparison of *scaled* simulated and experimental pure component CO2 and CH4 isotherms in Hupp-4 at 298K. ▲-$CO_2$ experiment; ●-$CH_4$ experiment; solid curve-$CO_2$ simulation; dashed curve-$CH_4$ simulation.**

As mentioned we also performed simulations of various mixtures and compared them to IAST predictions from the simulated pure component isotherms. The comparison between mixture simulations and IAST predicted isotherms can be seen for two different mixtures in *figure 7.5*. The selectivities were calculated as:

$$Selectivity = \frac{(y_{CO2} / y_{CH4})}{(x_{CO2} / x_{CH4})} \tag{7.2}$$

where $y$ is the mole fraction of the species in the adsorbed phase, and $x$ is the mole fraction of the species in the bulk phase.

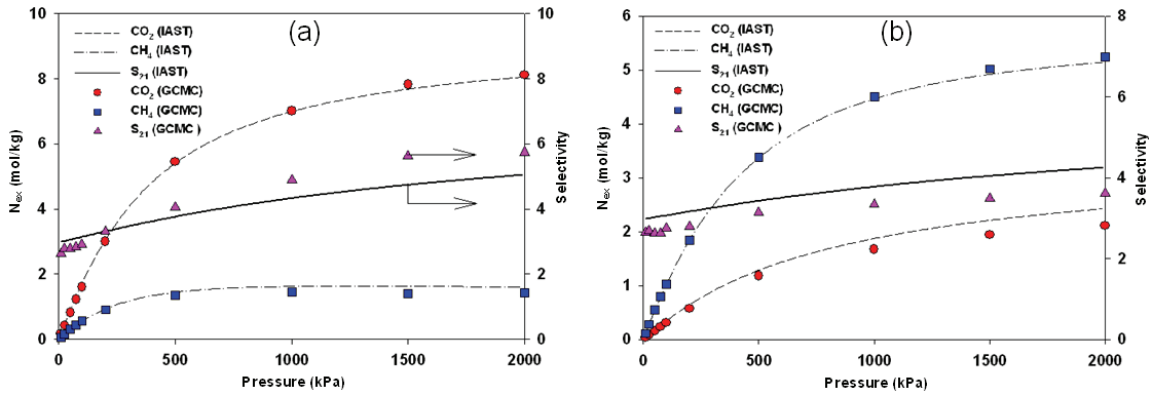


**Figure 7.5: Comparison of simulated mixture isotherms and selectivity to IAST predicted isotherms and selectivity from pure component simulations for two different mixtures.**
**a) 10% $CO_2$/90% $CH_4$ mixture; b) 50% $CO_2$/50% $CH_4$ mixture. (NOTE: Selectivity is on a secondary y-axis to the right)**

The curves in *figure 7.5* are the IAST predictions using TOTH isotherm fitting to the pure component simulations (TOTH isotherm fits not shown). There is excellent agreement between the predicted mixture isotherms and the mixture simulations. The selectivities also agree fairly well. It is important to verify the validity of IAST in the system, as the experimental method used allows only for pure, single component measurements.

More simulated mixture isotherms and selectivities can be seen in *figure 7.6*. The four mixture compositions investigated indicate that $CO_2$ could be extracted to a mole fraction of 96% from an initial composition of 10% $CO_2$, 90% $CH_4$ in four stages. This rough conclusion is determined by noticing the mole fraction of $CO_2$ at 2000 kPa (20 bar) from the four starting compositions (this is indicated on the individual graphs in *figure 7.6*). The mole fractions of $CO_2$ at 2000 kPa approximately follow the starting compositions in the four mixtures studied. It should also be noted that a selectivity of almost 8 is obtained in the 75% $CO_2$, 25% $CH_4$ mixture which is fairly good for a mixture of two light gasses.

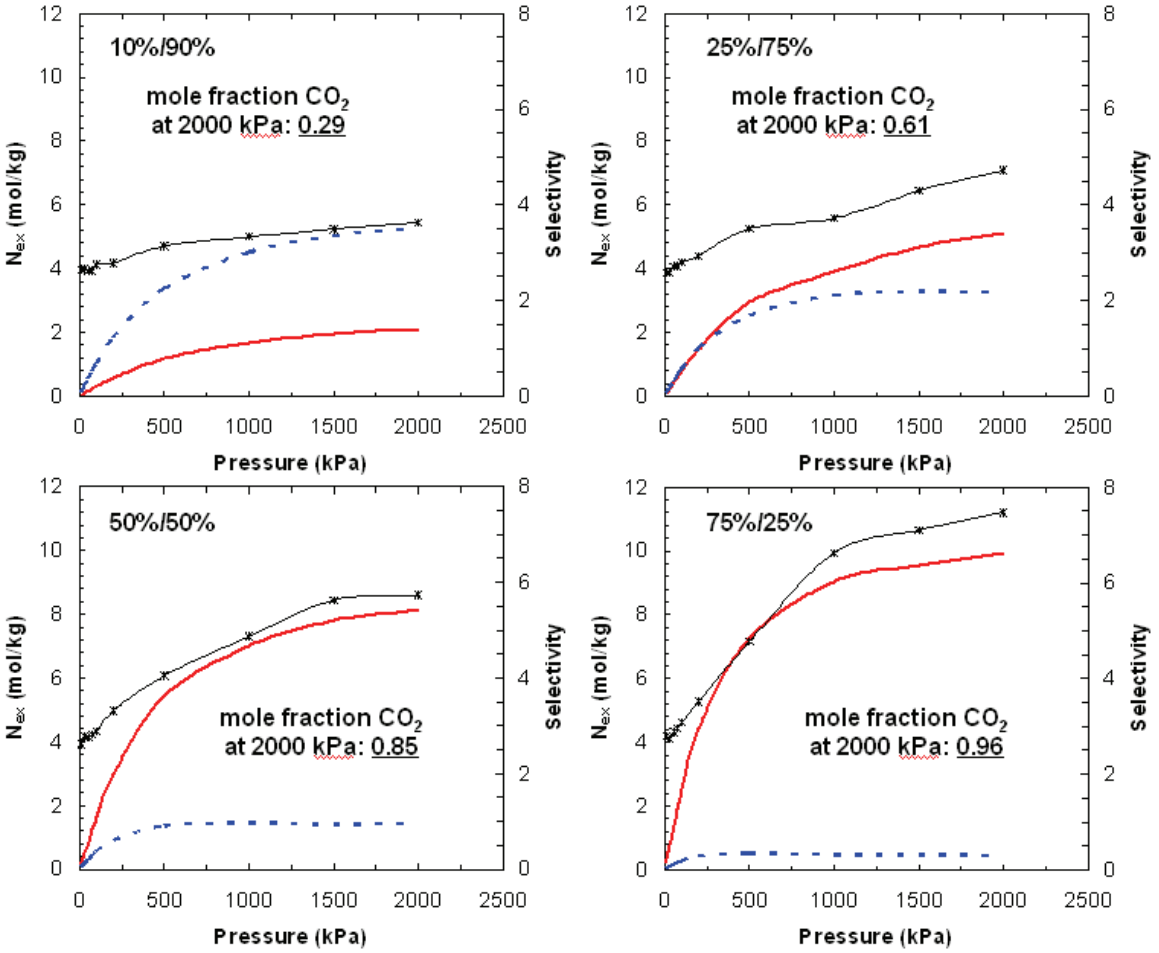


**Figure 7.6: $CO_2/CH_4$ mixture simulations at 298K for several bulk phase compositions. The bulk phase $CO_2/CH_4$ mole ratio can be seen in the upper left corner of the graphs. Solid line - $CO_2$; dashed line - $CH_4$; ∗ - selectivity. The mole fraction of $CO_2$ in the adsorbed phase at 2000 kPa is also given in each graph.**

### *7.4: Conclusion*

This study briefly investigates the possible use of a paddlewheel MOF for separating $CO_2$ and $CH_4$. In comparing the simulations of the single component adsorption isotherms of these gasses with those found experimentally in the material referred to as Hupp-4, potential issues with the synthesized material were exposed. Specifically, the simulations point to higher adsorption loadings indicating that there may be residual solvent within the material or potential framework degradation. The use of IAST for this

adsorption system was determined to be sufficient for estimating dual-component isotherms from single component data. Finally, various $CO_2/CH_4$ mixtures were investigated to evaluate the performance of the material over a range of starting compositions.

# Chapter 8: Molecular Simulation of Carbon Dioxide and Nitrogen Adsorption Sites in the Metal-Organic Framework IRMOF-1

## *8.1: Introduction*

The framework structures of MOFs are known from x-ray crystallography. However, information about the adsorption sites within this framework structure is also important. Only when both are known can one devise a strategy to design and tailor the pore size and organic linkers. For example, the IRMOF materials differ in linker molecule, but all have the same corner cluster in a cubic arrangement. Clearly, if the $Zn_4O$ would be the dominant adsorption site, an effect of a change in linker molecule would only show up at higher loadings.

Rowsell et al. performed a detailed x-ray diffraction study on the gas adsorption sites of argon and nitrogen in IRMOF-1[138]. The refinement of data collected between 30 and 293 K revealed a total of eight symmetry independent adsorption sites for argon. Five of these sites were found near the $Zn_4O$ cluster and the linker molecules; the remaining three sites form a second layer in the pores. For nitrogen at 30 K, three independent sites were partially occupied. The low rotational disorder at 30 K allowed for refinement as a single orientation, while at higher temperatures much more rotational disorder was found. At 120 K three possible orientations on the primary site were found. In IRMOF-1 the linkage of the zinc-oxygen complexes is forced to be alternating between linkers pointing outward and inward. This results in a structure that contains two alternating cavities of about 10.9 Å and 14.3 Å in diameter. The experimental results of Rowsell et al. suggest that the resulting adsorption sites in the large and small cages are not equivalent[138]. For argon at 30 K and half saturation loading, site I (the large cage) is filled 98%, while site II

in the smaller cage is only 29% occupied. A deuterium NMR study combined with modeling by Gonzales et al. showed site I to be the preferred site for benzene[139]. Amirjalayer et al. also found, using classical simulations, a preference for site I: at a loading of 10 benzenes per unit cell and 300K on average 92.4% reside in the large cage, and only 7.6% of the benzenes are found in the smaller cage[140]. Walton and Snurr studied the pore-filling mechanism of nitrogen in IRMOF-1, IRMOF-10, and IRMOF-16[141]. At low coverage, $N_2$ molecules populated the corner region site I where the interaction energy with the framework is strongest. As loading increases, a gradual layering of adsorbed $N_2$ and a clear formulation of a full monolayer was observed for IRMOF-16. For the smaller IRMOF-1 the adsorption and pore filling did not occur in well-defined layers.

Molecular simulations of adsorption isotherms in MOFs have generally shown good agreement with experiments[42,58,59,108]. In addition to predicting macroscopic observables, simulations can also provide useful molecular level insights. One of the main goals here is to show that besides good agreement of the adsorption isotherms, classical simulations are also able to capture the location and occupation of the adsorption sites well. In this study, we investigate the location of the adsorption sites and the positions of $N_2$ and $CO_2$ within these sites by performing Monte Carlo simulations and quantum chemical calculations.

### *8.2: Review of experimental work and identification of adsorption sites*

Rowsell et al.[138] found eight individual sites for adsorption of argon in IRMOF-1 at 30 K. Five of these sites can be directly related to positions relative to the framework and

are shown in *figure 8.1a*. The picture shows three axes in blue using the central corner oxygen as the origin. Four zinc atoms surround the oxygen to form a Zn4O cluster displayed in a (yellow) tetrahedral arrangement. Note that all structures based on tetrahedral corner clusters have an alternating sequence of linker molecules, where one is pointing "outward" and the next is pointing "inward". This results in two types of cages. Site I is located exactly above the central oxygen (on the corner–corner diagonal of the large cage). The location is in the bigger cage with the linkers pointing outward. Site II is located in the small cage where the linkers point inward. The site lies on the line drawn from the central oxygen through the zinc. Both site I and II occur 32 times per unit cell volume. A unit cell contains 8 $Zn_4O$ clusters; there are also 8 cavities, 4 small and 4 large ones; there are 24 linker molecules. Site III (green) is found exactly in the three planes drawn as transparent blue. The three-fold symmetry leads to 96 such sites per unit cell, and their positions are on the planes separating the small and large cages. Site IV is located above and beneath the center of the phenyl ring, and site V is on the edges of the phenyl ring. There are 48 of these sites per unit cell. Rowsell et al.[138] found a total of eight sites; two additional sites form a layer above site IV, and the remaining site is located at the center of the small cage surrounded by site V.

Three independent sites were partially occupied by $N_2$ molecules at 30 K, corresponding to argon sites I, III, and V, as shown in *figure 8.1b*. The number of sites is 32, 96, and 48, for site I, III, and V, respectively. Site II was not found at 30 K, but the site was occupied at higher temperature. Rowsell et al.[138] state that the distance between site II and III is too small to allow simultaneous occupation by nitrogen. The refinement of nitrogen showed some rotational disorder at 120 and 90 K. At 30K however, only a

single orientation at site I was found. The distances between the two nitrogen atoms are 1.036, 1.10, and 1.094 Å , for sites I, III, and V, respectively. The value for gas-phase nitrogen is 1.0976 Å. The experiments were performed by mounting the crystal specimens in capillaries connected to a gas manifold for evacuation before being backfilled with argon or nitrogen and flame-sealed. The amount of gas in the capillary available for adsorption was estimated to be about 40–80 molecules per unit cell, which is less than half the saturation uptake for IRMOF-1. As a consequence of this experimental procedure, a decrease in temperature is accompanied by an increase in loading.

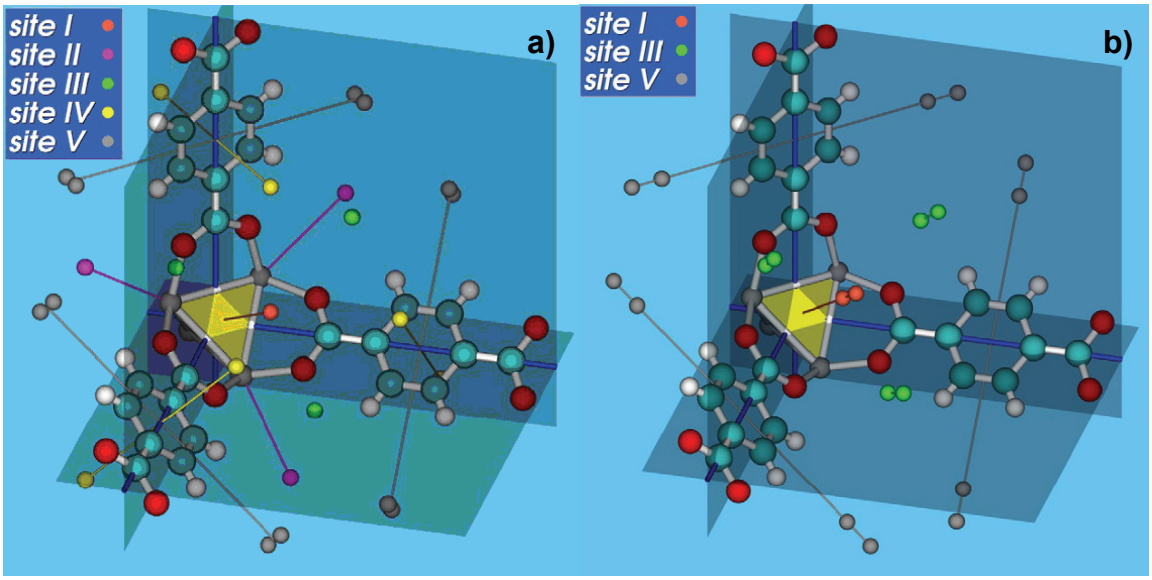


**Figure 8.1: a) Adsorption sites of argon near the framework in IRMOF-1 at 30K as found in the experiments of Rowsell et al. [138] b) Adsorption sites of nitrogen in IRMOF-1 at 30K as found in the experiments of Rowsell et al.[138].**

### *8.3: Simulation methods*

The classical simulations model dispersion and repulsion using Lennard-Jones potentials and charge interactions with a Coulomb potential. The framework was

considered rigid with parameters from Dubbeldam, et al.[142] Nitrogen and carbon dioxide are simulated as small rigid molecules with a charge distribution placed to mimic the proper quadrupole moment. For nitrogen the charges q are placed at the nuclei of both atoms with a compensating charge −2q placed at the center of mass. The nitrogen Lennard-Jones interaction is with both nitrogen atoms[125]. The carbon dioxide model has charges and Lennard-Jones interactions operating on the positions of the three nuclei[143].

### *8.4: Discussion and results*

#### *8.4.1: Classical studies of $N_2$ and $CO_2$ adsorption sites*

Carbon dioxide and nitrogen prefer site I near the $Zn_4O$ cluster of the big cage where the linkers point outward. The site is preferred over site II near the $Zn_4O$ cluster of the smaller cage where the linkers point inward. Site IV above and beneath the phenyl ring of the linker is even smaller in energy. Sometimes several different energies are found for these positions, e.g. $CO_2$ has two different orientations at the phenyl ring: both are parallel with the phenyl ring, but one is aligned along the linker axis, the other one orthogonal to it. For some molecules the adsorption site II does not exist at infinite dilution, e.g. $CO_2$. In contrast to $N_2$, $CO_2$ is too long to be in a potential well near the corners in the smaller cages. All minimized $CO_2$ starting at site II ended up at site I. At low loading, $CO_2$ is exclusively found at site I and at site V above and beneath the phenyl ring of the linker in two possible orientations. This suggests that the filling of site II is very sensitive to the shape and size of the molecule.

#### *8.4.2: Orientation of carbon dioxide (classical and quantum)*

To investigate the effect of orientation we compared the orientation of $CO_2$ obtained from the classical simulations with quantum simulations. The quantum mechanical results were obtained with Gaussian03[35] using the PBEPBE density functional. This uses the Perdew, Burke, and Ernzerhof functional for both exchange and correlation[126,127]. A 6-31g* basis set was used. This includes one polarization function (*) on the heavy atoms, i.e. not on hydrogen. The cluster we used is depicted in *figure 8.2*.

Both the classical and the quantum simulations point to the same minimum energy configuration, a planar orientation pointing towards the zinc atom. *Figure 8.3* shows the relative energies when the angle of orientation is varied with respect to the angle of the minimum energy configuration. The energy difference is an upper bound because a relaxed structure with that angle would have a lower energy. The $CO_2$ molecule has a minimum energy around $240^o$, a higher energy value at angles around $180^o$, and for the classical simulations again a slightly lower energy around $130^o$. The energy maximum is less pronounced for the quantum simulations. Note that the classical potentials contain dispersion forces while dispersion is absent in the quantum DFT computations. Potentially even better agreement could be obtained by adding dispersion to the quantum simulations. It could increase the energy penalty at $180^o$ because dispersion usually leads to stronger adsorption to a surface and hence a more planar orientation of $CO_2$. However, dispersion is notoriously difficult to describe using quantum chemical calculations.

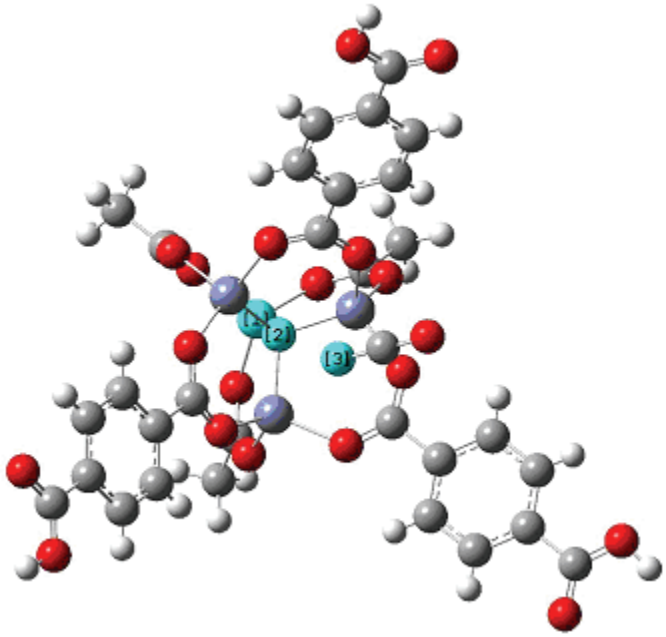


**Figure 8.2: The preferred orientation of carbon dioxide at 0K obtained by quantum mechanics (PBEPBE functional, 6-31g* basis set). The closest oxygen of the carbon dioxide (labeled '[3]') is near the diagonal formed by the central oxygen (labeled '[2]') and a zinc atom labeled '[1]').**

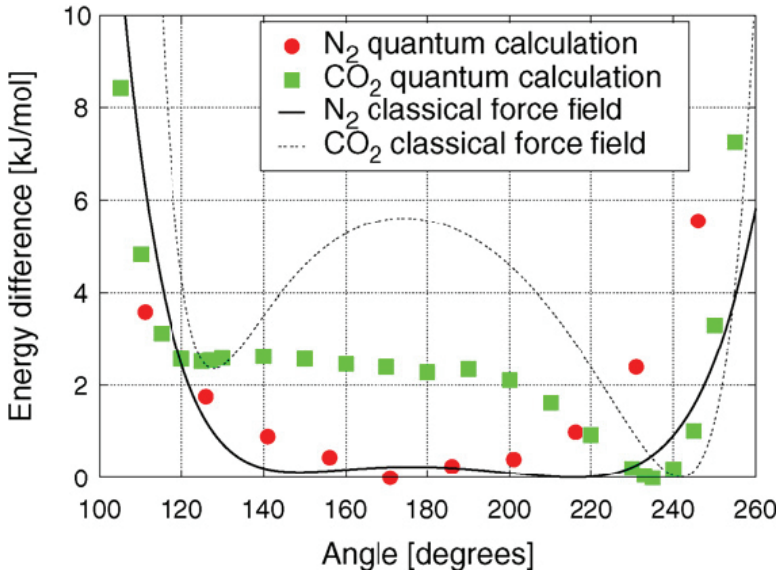


**Figure 8.3: Relative energies computed for a change in Oa–N–N angle from the minimum energy position. The angles of reference are 171° for the DFT calculations, and 215.8° for the classical simulations. The closest atom of the adsorbate remains fixed, the direction of angles lower than 180° is toward the linker, higher than 180° is directed toward the zinc, and 180° means that the nitrogen molecules is coinciding with the diagonal.**

### *8.4.3: Orientation of nitrogen (classical and quantum)*

*Figure 8.4* shows the two possible minimum energy positions for a single nitrogen molecule at site I, obtained from minimization using the classical force field. In *figure 8.4a* the experimental position is shown lying on the diagonal of the large cage. When viewed from the diagonal (*figure 8.4b)*, we observe two orientations: 1) the closest nitrogen atom is directly 3.97 Å above the central oxygen, the second atom pointing toward a zinc, and 2) the closest nitrogen atom is directly above the zinc, the other atom above the oxygen of a carboxylate group of a neighboring linker molecule. Position 1 is more favorable than position 2. Position 1 at site I is close to the experimental one, but tilted in three possible orientations. Interestingly, the averaged result matches the experiment, and could possibly explain the somewhat shorter N-N distance of the two sites found experimentally at 30K (1.03 Å vs. 1.10 Å for the gas-phase). The average bond length of a nitrogen molecule with one atom on the diagonal and an off-diagonal, three fold symmetry position for the second atom projected onto the diagonal, would lead to a shorter length. We note that in the experiment a threefold orientation is found at 120K. However, the classical orientation points toward the zinc atom, while the nitrogen in experiments is aligned toward the carboxylate group of the linker.

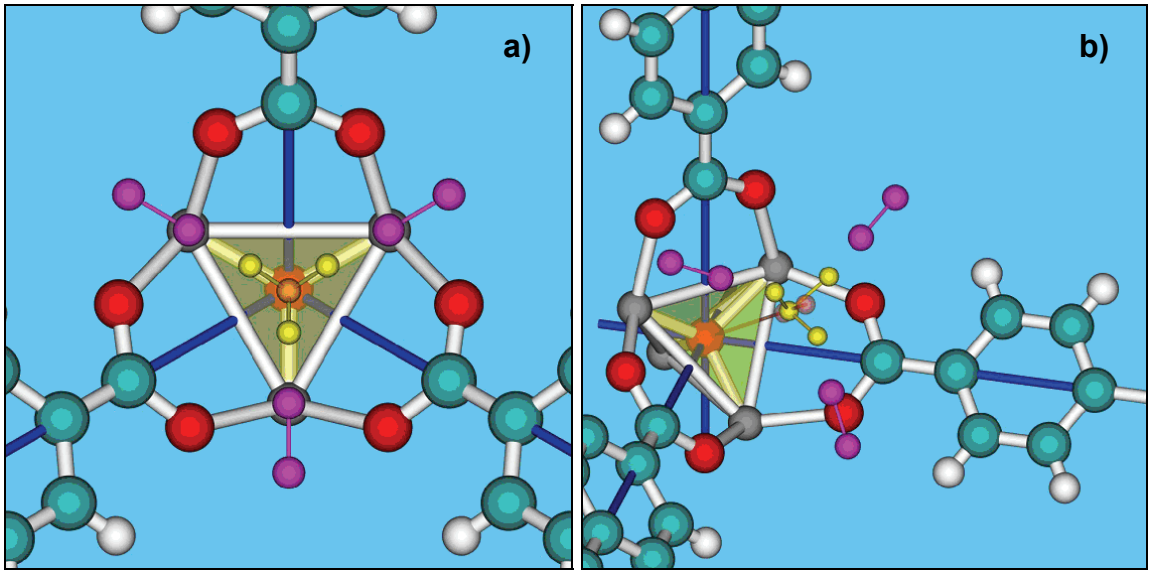


**Figure 8.4: Top (a) and side view (b) of the two minimum energy positions of the nitrogen molecule computed with classical simulations, compared to the experimentally found position. The most stable configuration is drawn in yellow (three possible positions), the experimental position is drawn transparent at the same position (one orientation). Slightly higher in energy is the second position adsorbed directly above the zinc**

To solve the apparent discrepancy for the orientation we performed many quantum mechanical minimizations using different starting positions. Several local minima were found, but after tightening the convergence criteria most of the starting positions converged to an orientation slightly tilted with respect to the experimental orientation. The experimental distance at 30K from the central oxygen to the closest nitrogen atom is 3.754 Å. Quantum mechanical calculations give 3.819 Å. Also the classical position 1 was identified as a local minimum using DFT. The cluster we used and the orientation with the lowest energy are shown in *figure 8.5*, along with an iso-contour of the electrostatic potential surface. The different results with and without tightening the convergence criteria suggested a flat and shallow energy landscape. *Figure 8.3* shows the relative energies when the angle of orientation is varied with respect to the angle of the minimum energy configuration. The energy difference is an upper bound because a relaxed structure with that angle would have a lower energy. The orientation found by

classical simulation (215.8$^{o}$), by experiment (180$^{o}$ at 30K), and by quantum calculations (171$^{o}$) are all within 1 kJ/mol of each other. Even the experimental result at 120K (136$^{o}$) can be considered close in energy. We conclude that all our data point to an adsorption mechanism for small molecules where one of the atoms is directly above the central corner oxygen while the orientation of the molecule is likely to be found in a wide range of angles. *Figure 8.5* shows that the electrostatic potential around nitrogen is almost spherical.

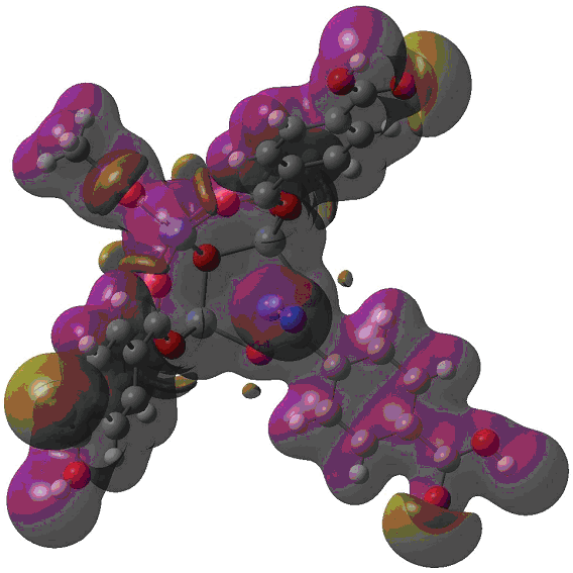

**Figure 8.5: The preferred orientation of nitrogen at 0K obtained by quantum mechanics (PBEPBE functional, 6-31g* basis set). We show the iso contour surface of the electrostatic potential surface at 0.04 Hartree. The distance of the closest nitrogen with the central oxygen is 3.819 Å.**

### *8.5: Conclusions*

Pore filling inside IRMOF-1 at low temperature occurs in well-defined sites. The dominant adsorption site for small molecules is site I near the $Zn_4O$ cluster of the big cage where the linkers point outward. At 30 K the molecules are localized around their crystallographic sites, while at room temperature the molecules are found throughout the

pores. Small gas molecules adsorb preferentially above the central corner oxygen, but their orientation is relatively free. Longer molecules align more toward the linkers which provides favorable dispersion interactions.

# Chapter 9: Conclusion

A number of adsorption studies were performed on a variety of metal-organic frameworks. In chapters 2 and 3, the dependence of hydrogen adsorption on three important material characteristics was determined and discussed. We also evaluated the feasibility of using these materials in hydrogen storage applications. Our results indicate that if the heat of adsorption can be increased to 10-15 kJ/mol while maintaining a significant free volume, then reasonable storage densities can be obtained. In chapter 4 we investigated the effect of reducing an organic ligand on the electronic binding energy of hydrogen with the ligand; an increase in binding energy was seen upon simulated reduction. Chapters 5 and 6 reviewed carbon dioxide adsorption behavior in metal-orgaic frameworks and explained the interesting inflection behavior in a number of MOF materials. It was also shown that carbon dioxide can reach liquid densities within MOF pores at relatively low pressures. In chapter 7, adsorption of carbon dioxide/methane mixtures was investigated, and it was shown that adsorption of these mixtures in MOFs is selective for carbon dioxide at a variety of mixture ratios. Finally, in chapter 8 we reviewed adsorption sites within metal-organic frameworks. This work as a whole uncovered some fundamentals of hydrogen and carbon dioxide adsorption behavior in these new materials.

## *9.1: Future Perspective and Outlook*

Many of the concepts in this document concerning material characteristics and their effect on hydrogen adsorption within microporous materials most likely pertain to the

adsorption of light gasses in general. The next logical step for the concepts in chapters 2 and 3 would be to extend these principles to the adsorption of other species of interest. In chapter 4, the effect of reducing a MOF framework on hydrogen binding energy is investigated using quantum techniques. A logical extension to this study would be to use quantum calculations to determine a force-field that could be used in classical simulations, in which the adsorption loading of hydrogen could be determined. The study of $CO_2$ adsorption in MOFs in chapters 5, 6, and 7 barely begin to explore the potential of these materials for use in separation applications. More detailed studies on a variety of $CO_2$ containing mixtures are necessary, as well as a more in depth analysis of optimizing a material for use in pressure swing adsorption. Numerous questions still need to be answered regarding the optimal pressure range over which the pressure swing adsorption should take place, as well as the optimal gravimetric or volumetric loading that should exist between the pressure range.

Finally, It is the author's belief that though only a select few applications have been investigated in this study, metal-organic frameworks have untold potential in a number of additional commercial applications. The separation of liquid hydrocarbon mixtures for example could be of interest, perhaps in increasing the octane value in gasoline or in selecting desired linear alpha olefin carbon numbers for producing plastics. Designing these materials as catalysts for specific applications is also of great interest. The possibility of using these materials as more selective Fischer-Tropsch catalysts is especially exciting, as F-T synthesis generally yields a large variety of products. Truly, we have just begun to scratch the surface of the possible uses for this exciting group of materials.

**References**

(1) Yaghi, O. M.; O'Keeffe, M.; Ockwig, N. W.; Chae, H. K.; Eddaoudi, M.; Kim, J. *Nature* 2003, *423*, 705.

(2) Rowsell, J. L. C.; Yaghi, O. M. *Microporous and Mesoporous Materials* 2004, *73*, 3.

(3) Rosseinsky, M. J. *Microporous and Mesoporous Materials* 2004, *73*, 15.

(4) Li, H.; Eddaoudi, M.; Groy, T. L.; Yaghi, O. M. *Journal of the American Chemical Society* 1998, *120*, 8571.

(5) James, S. L. *Chemical Society Reviews* 2003, *32*, 276.

(6) Eddaoudi, M.; Li, H. L.; Yaghi, O. M. *Journal of the American Chemical Society* 2000, *122*, 1391.

(7) Janiak, C. *Dalton Transactions* 2003, 2781.

(8) Kitagawa, S.; Kitaura, R.; Noro, S. *Angewandte Chemie-International Edition* 2004, *43*, 2334.

(9) Snurr, R. Q.; Hupp, J. T.; Nguyen, S. T. *Aiche Journal* 2004, *50*, 1090.

(10) Yaghi, O. M.; Li, H. L.; Davis, C.; Richardson, D.; Groy, T. L. *Accounts of Chemical Research* 1998, *31*, 474.

(11) Matsuda, R.; Kitaura, R.; Kitagawa, S.; Kubota, Y.; Belosludov, R. V.; Kobayashi, T. C.; Sakamoto, H.; Chiba, T.; Takata, M.; Kawazoe, Y.; Mita, Y. *Nature* 2005, *436*, 238.

(12) Pan, L.; Sander, M. B.; Huang, X. Y.; Li, J.; Smith, M.; Bittner, E.; Bockrath, B.; Johnson, J. K. *Journal of the American Chemical Society* 2004, *126*, 1308.

(13) Kesanli, B.; Cui, Y.; Smith, M. R.; Bittner, E. W.; Bockrath, B. C.; Lin, W. B. *Angewandte Chemie-International Edition* 2005, *44*, 72.

(14) Chen, B. L.; Eddaoudi, M.; Hyde, S. T.; O'Keeffe, M.; Yaghi, O. M. *Science* 2001, *291*, 1021.

(15) Rowsell, J. L. C.; Millward, A. R.; Park, K. S.; Yaghi, O. M. *Journal of the American Chemical Society* 2004, *126*, 5666.

(16) Li, H.; Eddaoudi, M.; O'Keeffe, M.; Yaghi, O. M. *Nature* 1999, *402*, 276.

(17) Eddaoudi, M.; Kim, J.; Rosi, N.; Vodak, D.; Wachter, J.; O'Keefe, M.; Yaghi, O. M. *Science* 2002, *295*, 469.

(18) Ma, B. Q.; Mulfort, K. L.; Hupp, J. T. *Inorganic Chemistry* 2005, *44*, 4912.

(19) Erxleben, A. *Coordination Chemistry Reviews* 2003, *246*, 203.

(20) Ockwig, N. W.; Delgado-Friedrichs, O.; O'Keeffe, M.; Yaghi, O. M. *Accounts of Chemical Research* 2005, *38*, 176.

(21) Young, D. M.; Crowell, A. D. *Physical Adsorption of Gases*; Butterworths: London, England, 1962.

(22) Vuong, T.; Monson, P. A. *Langmuir* 1996, *12*, 5425.

(23) Myers, A. L.; Monson, P. A. *Langmuir* 2002, *18*, 10261.

(24) Valenzuela, D. P.; Myers, A. L. *Adsorption Equilibrium Data Handbook*; Prentice Hall: Englewood Cliffs, New Jersey, 1989.

(25) Smith, J. M.; Van Ness, H. C.; Abbott, M. M. *Introduction to Chemical Engineering Thermodynamics*, 6th ed.; Mc Graw Hill: New York, NY, 2001.

(26) Snurr, R. Q.; Bell, A. T.; Theodorou, D. N. *Journal of Physical Chemistry* 1993, *97*, 13742.

(27) Ruthven, D. M. *Principles of Adsorption and Adsorption Processes*; John Wiley & Sons: New York, 1984.

(28) Brunauer, S. *The Adsorption of Gases and Vapors*; Princeton University Press: Princeton, NJ, 1945; Vol. 1.

(29) Connolly, M. *Science* 1983, *221*, 709.

(30) Yang, R. T. *Gas Separation by Adsorption Processes*; Butterworth Publishers: Stoneham, MA, 1987.

(31) Rowsell, J. L. C.; Yaghi, O. M. *Journal of the American Chemical Society* 2006, *128*, 1304.

(32) Sudik, A. C.; Millward, A. R.; Ockwig, N. W.; Cote, A. P.; Kim, J.; Yaghi, O. M. *Journal of the American Chemical Society* 2005, *127*, 7110.

(33) Jagiello, J.; Anson, A.; Martinez, M. T. *Journal of Physical Chemistry B* 2006, *110*, 4531.

(34) Leach, A. R. *Molecular Modelling: Principles and Applications*, 2nd ed.; Pearson/Prentice Hall: Harlow, England, 2001.

(35) M. J. Frisch, G. W. T., H. B. Schlegel, G. E. Scuseria, M. A. Robb, J. R. Cheeseman, J. A. Montgomery, Jr., T. Vreven, K. N. Kudin, J. C. Burant, J. M. Millam, S. S. Iyengar, J. Tomasi, V. Barone, B. Mennucci, M. Cossi, G. Scalmani, N. Rega, G. A. Petersson, H. Nakatsuji, M. Hada, M. Ehara, K. Toyota, R. Fukuda, J. Hasegawa, M. Ishida, T. Nakajima, Y. Honda, O. Kitao, H. Nakai, M. Klene, X. Li, J. E. Knox, H. P. Hratchian, J. B. Cross, C. Adamo, J. Jaramillo, R. Gomperts, R. E. Stratmann, O. Yazyev, A. J. Austin, R. Cammi, C. Pomelli, J. W. Ochterski, P. Y. Ayala, K. Morokuma, G. A. Voth, P. Salvador, J. J. Dannenberg, V. G. Zakrzewski, S. Dapprich, A. D. Daniels, M. C. Strain, O. Farkas, D. K. Malick, A. D. Rabuck, K. Raghavachari, J. B. Foresman, J. V. Ortiz, Q. Cui, A. G. Baboul, S. Clifford, J. Cioslowski, B. B. Stefanov, G. Liu, A. Liashenko, P. Piskorz, I. Komaromi, R. L. Martin, D. J. Fox, T. Keith, M. A. Al-Laham, C. Y. Peng, A. Nanayakkara, M. Challacombe, P. M. W. Gill, B. Johnson, W. Chen, M. W. Wong, C. Gonzalez, and J. A. Pople. Gaussian 03, Revision C.02; Gaussian, Inc.: Wallingford CT, 2004.

(36) DOE “Hydrogen, Fuel Cells and Infrastructure Technologies Program: Multi-Year Research, Development and Demonstration Plan,”, 2005.

(37) Zuttel, A. *Materials Today* 2003, *6*, 24.

(38) Furukawa, H.; Miller, M. A.; Yaghi, O. M. *Journal of Materials Chemistry* 2007, *17*, 3197.

(39) Fichtner, M. *Advanced Engineering Materials* 2005, *7*, 443.

(40) Schlapbach, L.; Zuttel, A. *Nature* 2001, *414*, 353.

(41) Nijkamp, M. G.; Raaymakers, J.; van Dillen, A. J.; de Jong, K. P. *Applied Physics A-Materials Science & Processing* 2001, *72*, 619.

(42) Duren, T.; Sarkisov, L.; Yaghi, O. M.; Snurr, R. Q. *Langmuir* 2004, *20*, 2683.

(43) Seki, K. *Chemical Communications* 2001, 1496.

(44) Rowsell, J. L. C.; Yaghi, O. M. *Angewandte Chemie-International Edition* 2005, *44*, 4670.

(45) Chun, H.; Dybtsev, D. N.; Kim, H.; Kim, K. *Chemistry-a European Journal* 2005, *11*, 3521.

(46) Ferey, G.; Latroche, M.; Serre, C.; Millange, F.; Loiseau, T.; Percheron-Guegan, A. *Chemical Communications* 2003, 2976.

(47) Chae, H. K.; Siberio-Perez, D. Y.; Kim, J.; Go, Y.; Eddaoudi, M.; Matzger, A. J.; O'Keeffe, M.; Yaghi, O. M. *Nature* 2004, *427*, 523.

(48) Langmi, H. W.; Walton, A.; Al-Mamouri, M. M.; Johnson, S. R.; Book, D.; Speight, J. D.; Edwards, P. P.; Gameson, I.; Anderson, P. A.; Harris, I. R. *Journal Of Alloys And Compounds* 2003, *356*, 710.

(49) Menon, V. C.; Komarneni, S. *Journal of Porous Materials* 1998, *5*, 43.

(50) Texier-Mandoki, N.; Dentzer, J.; Piquero, T.; Saadallah, S.; David, P.; Vix-Guterl, C. *Carbon* 2004, *42*, 2744.

(51) Allen, M. P.; Tildesley, D. J. *Computer Simulations of Liquids*; Clarendon Press: Oxford, 1987.

(52) Frenkel, D.; Smit, B. *Understanding of Molecular Simulations: from Algorithms to Applications*, 2nd ed.; Academic Press: San Diego, 2002.

(53) Gupta, A.; Chempath, S.; Sanborn, M. J.; Clark, L. A.; Snurr, R. Q. *Molecular Simulation* 2003, *29*, 29.

(54) Michels, A.; Degraaff, W.; Tenseldam, C. A. *Physica* 1960, *26*, 393.

(55) Darkrim, F.; Aoufi, A.; Malbrunot, P.; Levesque, D. *Journal of Chemical Physics* 2000, *112*, 5991.

(56) Mayo, S. L.; Olafson, B. D.; Goddard, W. A. *Journal of Physical Chemistry* 1990, *94*, 8897.

(57) Sagara, T.; Klassen, J.; Ganz, E. *Journal of Chemical Physics* 2004, *121*, 12543.

(58) Yang, Q. Y.; Zhong, C. L. *Journal of Physical Chemistry B* 2005, *109*, 11862.

(59) Garberoglio, G.; Skoulidas, A. I.; Johnson, J. K. *Journal of Physical Chemistry B* 2005, *109*, 13094.

(60) After this chapter was published, three experimental papers appeared reporting adsorption isotherms for hydrogen in IRMOFs at 77 K and pressures up to 80 bar[61-63]. Simulations and experiments show similar values for the saturation pressures, but there is some discrepancy in the loading (also among the experimental reports). Further work is needed to uncover the reasons for these discrepancies, but the conclusions of this paper should not be affected.

(61) Dailly, A.; Vajo, J. J.; Ahn, C. C. *Journal of Physical Chemistry B* 2006, *110*, 1099.

(62) Wong-Foy, A. G.; Matzger, A. J.; Yaghi, O. M. *Journal of Americal Chemical Society* 2006, *ASAP Publication*, Web.

(63) Panella, B.; Hirscher, M.; Putter, H.; Muller, U. *Advanced Functional Materials* 2006, *16*, 520.

(64) Sagara, T.; Klassen, J.; Ortony, J.; Ganz, E. *Journal of Chemical Physics* 2005, *123*.

(65) Hubner, O.; Gloss, A.; Fichtner, M.; Klopper, W. *Journal of Physical Chemistry A* 2004, *108*, 3019.

(66) Gregg, S. J.; Sing, K. S. W. *Adsorption, Surface Area, and Porosity*; Academic Press: New York, 1967.

(67) Heuchel, M. *Langmuir* 1997, *13*, 1150.

(68) Bojan, M. J.; Vernov, A. V.; Steele, W. A. *Langmuir* 1992, *8*, 901.

(69) Montgomery, D. C.; Runger, G. C.; Hubele, N. F. *Engineering Statistics*, 2nd ed.; Wiley: New York, 2001.

(70) Mueller, T.; Ceder, G. *Journal of Physical Chemistry B* 2005, *109*, 17974.

(71) Rosi, N. L.; Eckert, J.; Eddaoudi, M.; Vodak, D. T.; Kim, J.; O'Keeffe, M.; Yaghi, O. M. *Science* 2003, *300*, 1127.

(72) Duren, T.; Snurr, R. Q. 7th International Symposium on the Characterization of Porous Solids, 2005.

(73) Hinrichsen, E. L.; Feder, J.; Jossang, T. *Physical Review A* 1990, *41*, 4199.

(74) It should be noted that the random monolayer packing of 0.55 coverage corresponds to a density of hydrogen of 91 g/L and the hexagonal monolayer packing of 0.91 coverage corresponds to a density of hydrogen of 151 g/L if the height of one

hydrogen molecule is used to determine the volume of the monolayer. This is the primary reason that the potential uptake values are generally higher assuming monolayer coverage than when assuming the density of liquid or solid hydrogen within the free volume.

(75) Braker, W.; Mossman, A. L. *Matheson Gas Data Book*, 6th ed.; Matheson: Secaucus, NJ, 1980.

(76) Pauling, L. *College Chemistry: An Introductory Textbook of General Chemistry*, 2nd ed.; W. H. Freeman & Company: San Francisco, CA, 1955.

(77) Hirscher, M.; Panella, B. *Scripta Materialia* 2007, *56*, 809.

(78) Vitillo, J. G.; Ricchiardi, G.; Spoto, G.; Zecchina, A. *Physical Chemistry Chemical Physics* 2005, *7*, 3948.

(79) Frost, H.; Duren, T.; Snurr, R. Q. *Journal of Physical Chemistry B* 2006, *110*, 9565.

(80) Bhatia, S. K.; Myers, A. L. *Langmuir* 2006, *22*, 1688.

(81) Jung, D. H.; Kim, D.; Lee, T. B.; Choi, S. B.; Yoon, J. H.; Kim, J.; Choi, K.; Choi, S. H. *Journal of Physical Chemistry B* 2006, *110*, 22987.

(82) Dinca, M.; Dailly, A.; Liu, Y.; Brown, C. M.; Neumann, D. A.; Long, J. R. *Journal of the American Chemical Society* 2006, *128*, 16876.

(83) Chen, B. L.; Ockwig, N. W.; Millward, A. R.; Contreras, D. S.; Yaghi, O. M. *Angewandte Chemie-International Edition* 2005, *44*, 4745.

(84) Forster, P. M.; Eckert, J.; Chang, J. S.; Park, S. E.; Ferey, G.; Cheetham, A. K. *Journal of the American Chemical Society* 2003, *125*, 1309.

(85) Simonyan, V. V.; Diep, P.; Johnson, J. K. *Journal of Chemical Physics* 1999, *111*, 9778.

(86) Mulfort, K. L.; Hupp, J. T. *J. Am. Chem. Soc.* 2007, *129*, 9604.

(87) Chui, S. S. Y.; Lo, S. M. F.; Charmant, J. P. H.; Orpen, A. G.; Williams, I. D. *Science* 1999, *283*, 1148.

(88) Vishnyakov, A.; Ravikovitch, P. I.; Neimark, A. V.; Bulow, M.; Wang, Q. M. *Nano Letters* 2003, *3*, 713.

(89) Rappe, A. K.; Casewit, C. J.; Colwell, K. S.; Goddard, W. A.; Skiff, W. M. *Journal of the American Chemical Society* 1992, *114*, 10024.

(90) Li, Y. W.; Yang, R. T. *Journal of the American Chemical Society* 2006, *128*, 726.

(91) Poirier, E.; Chahine, R.; Benard, P.; Lafi, L.; Dorval-Douville, G.; Chandonia, P. A. *Langmuir* 2006, *22*, 8784.

(92) Li, Y. W.; Yang, R. T. *Journal of the American Chemical Society* 2006, *128*, 8136.

(93) Dinca, M.; Long, J. R. *Journal of the American Chemical Society* 2005, *127*, 9376.

(94) Han, S. S.; Goddard, W. A. *Journal of the American Chemical Society* 2007, *129*, 8422.

(95) Sagara, T.; Ortony, J.; Ganz, E. *Journal of Chemical Physics* 2005, *123*.

(96) Hamel, S.; Cote, M. *Journal of Chemical Physics* 2004, *121*, 12618.

(97) Bordiga, S.; Vitillo, J. G.; Ricchiardi, G.; Regli, L.; Cocina, D.; Zecchina, A.; Arstad, B.; Bjorgen, M.; Hafizovic, J.; Lillerud, K. P. *Journal of Physical Chemistry B* 2005, *109*, 18237.

(98) Giese, T. J.; York, D. M. *Journal of Chemical Physics* 2004, *120*, 590.

(99) Tafipolsky, M.; Amirjalayer, S.; Schmid, R. *Journal of Computational Chemistry* 2007, *28*, 1169.

(100) Millward, A. R.; Yaghi, O. M. *J. Am. Chem. Soc.* 2005, *127*, 17998.

(101) Millward, A. R. Adsorption of Environmentally Significant Gases (H2, CO2, H2S, CH4) in Metal-Organic Frameworks, Ph.D. Thesis, University of Michigan, 2006.

(102) Li, D.; Kaneko, K. *Chemical Physics Letters* 2001, *335*, 50.

(103) Fletcher, A. J.; Cussen, E. J.; Prior, T. J.; Rosseinsky, M. J.; Kepert, C. J.; Thomas, K. M. *Journal of the American Chemical Society* 2001, *123*, 10001.

(104) Bourrelly, S.; Llewellyn, P. L.; Serre, C.; Millange, F.; Loiseau, T.; Ferey, G. *Journal of the American Chemical Society* 2005, *127*, 13519.

(105) Kawakami, T.; Takamizawa, S.; Kitagawa, Y.; Maruta, T.; Mori, W.; Yamaguchi, K. *Polyhedron* 2001, *20*, 1197.

(106) Skoulidas, A. I.; Sholl, D. S. *Journal of Physical Chemistry B* 2005, *109*, 15760.

(107) Yang, Q. Y.; Zhong, C. L. *Journal of Physical Chemistry B* 2006, *110*, 17776.

(108) Yang, Q. Y.; Zhong, C. L. *Chemphyschem* 2006, *7*, 1417.

(109) Ramsahye, N. A.; Maurin, G.; Bourrelly, S.; Llewellyn, P.; Loiseau, T.; Ferey, G. *Physical Chemistry Chemical Physics* 2007, *9*, 1059.

(110) Babarao, R.; Hu, Z. Q.; Jiang, J. W.; Chempath, S.; Sandler, S. I. *Langmuir* 2007, *23*, 659.

(111) Rouquerol, F.; Rouquerol, J.; Sing, K. *Adsorption by Powders and Porous Solids*; Academic Press: London, 1999.

(112) Carrasco-Marin, F.; Lopez-Ramon, M. V.; Moreno-Castilla, C. *Langmuir* 1993, *9*, 2758.

(113) Cazorla-Amoros, D.; Alcaniz-Monge, J.; Linares-Solano, A. *Langmuir* 1996, *12*, 2820.

(114) Cazorla-Amoros, D.; Alcaniz-Monge, J.; de la Casa-Lillo, M. A.; Linares-Solano, A. *Langmuir* 1998, *14*, 4589.

(115) Pantatosaki, E.; Psomadopoulos, D.; Steriotis, T.; Stubos, A. K.; Papaioannou, A.; Papadopoulos, G. K. *Colloids and Surfaces a-Physicochemical and Engineering Aspects* 2004, *241*, 127.

(116) Vishnyakov, A.; Ravikovitch, P. I.; Neimark, A. V. *Langmuir* 1999, *15*, 8736.

(117) Yong, Z.; Mata, V.; Rodrigues, A. E. *Separation and Purification Technology* 2002, *26*, 195.

(118) Yong, Z.; Mata, V. G.; Rodrigues, A. E. *Adsorption-Journal of the International Adsorption Society* 2001, *7*, 41.

(119) Lee, J. S.; Kim, J. H.; Kim, J. T.; Suh, J. K.; Lee, J. M.; Lee, C. H. *Journal of Chemical and Engineering Data* 2002, *47*, 1237.

(120) Wang, Q. M.; Shen, D. M.; Bulow, M.; Lau, M. L.; Deng, S. G.; Fitch, F. R.; Lemcoff, N. O.; Semanscin, J. *Microporous and Mesoporous Materials* 2002, *55*, 217.

(121) Ramsahye, N. A.; Maurin, G.; Bourrelly, S.; Llewellyn, P. L.; Loiseau, T.; Serre, C.; Ferey, G. *Chemical Communications* 2007, 3261.

(122) Dybtsev, D. N.; Chun, H.; Yoon, S. H.; Kim, D.; Kim, K. *Journal of the American Chemical Society* 2004, *126*, 32.

(123) Serre, C.; Bourrelly, S.; Vimont, A.; Ramsahye, N. A.; Maurin, G.; Llewellyn, P. L.; Daturi, M.; Filinchuk, Y.; Leynaud, O.; Barnes, P.; Ferey, G. *Advanced Materials* 2007, *19*, 2246.

(124) Walton, K. S.; Millward, A. R.; Dubbeldam, D.; Frost, H.; Low, J.; Yaghi, O. M.; Snurr, R. Q. *Journal of the American Chemical Society* 2007, *(submitted)*.

(125) Potoff, J. J.; Siepmann, J. I. *Aiche Journal* 2001, *47*, 1676.

(126) Perdew, J. P.; Burke, K.; Ernzerhof, M. *Physical Review Letters* 1996, *77*, 3865.

(127) Perdew, J. P.; Burke, K.; Ernzerhof, M. *Physical Review Letters* 1997, *78*, 1396.

(128) Breneman, C. M.; Wiberg, K. B. *Journal of Computational Chemistry* 1990, *11*, 361.

(129) Bondi, A. *Journal of Physical Chemistry* 1964, *68*, 441.

(130) Yang, Q. Y.; Zhong, C. L. *Journal of Physical Chemistry B* 2006, *110*, 655.

(131) Nicholson, T. M.; Bhatia, S. K. *Journal of Physical Chemistry B* 2006, *110*, 24834.

(132) Macario, A.; Katovic, A.; Giordano, G.; Iucolano, F.; Caputo, D. *Microporous and Mesoporous Materials* 2005, *81*, 139.

(133) He, Y. F.; Seaton, N. A. *Langmuir* 2006, *22*, 1150.

(134) NIST. NIST Chemistry Webbook, 2007.

(135) Goodbody, S. J.; Watanabe, K.; Macgowan, D.; Walton, J.; Quirke, N. *Journal of the Chemical Society-Faraday Transactions* 1991, *87*, 1951.

(136) Myers, A. L.; Prausnitz. J. M. *Aiche Journal* 1965, *11*, 121.

(137) Do, D. D. *Adsorption Analysis: Equilibria and Kinetics*; Imperial College Press: Queensland, Australia, 1998; Vol. Vol. 2.

(138) Rowsell, J. L. C.; Spencer, E. C.; Eckert, J.; Howard, J. A. K.; Yaghi, O. M. *Science* 2005, *309*, 1350.

(139) Gonzalez, J.; Devi, R. N.; Tunstall, D. P.; Cox, P. A.; Wright, P. A. *Microporous and Mesoporous Materials* 2005, *84*, 97.

(140) Amirjalayer, S.; Tafipolsky, M.; Schmid, R. *Angewandte Chemie-International Edition* 2007, *46*, 463.

(141) Walton, K. S.; Snurr, R. Q. *Journal of the American Chemical Society* 2007, *129*, 8552.

(142) Dubbeldam, D.; Walton, K. S.; Ellis, D. E.; Snurr, R. Q. *Angewandte Chemie-International Edition* 2007, *46*, 4496.

(143) Harris, J. G.; Yung, K. H. *Journal of Physical Chemistry* 1995, *99*, 12021.

# ***APPENDICES***

## *Appendix A – Material characteristics*

| Material | mass (g/mol) | unit cell volume (Å$^3$) | material density (g/cm$^3$) | $SA_{accessible}$ [$H_2$ probe] ($m^2$/g) | $SA_{accessible}$ [$H_2$ probe] ($m^2/cm^3$) | free volume per unit cell [probe = 0.0] (Å$^3$) | pore volume (Å$^3$) | free volume / mass ($cm^3$/g) | void fraction from free volume |
|---|---|---|---|---|---|---|---|---|---|
| **IRMOF-1** | 6155.8 | 17237.49 | 0.59 | 3882.0 | 2290.4 | 13440.79 | 14026 | 1.372 | 0.780 |
| **IRMOF-4** | 8954.8 | 17272.15 | 0.864 | 2055.8 | 1770.0 | 10317.62 | 8744.5 | 0.588 | 0.597 |
| **IRMOF-5** | 10090.8 | 17100.93 | 0.983 | 984.6 | 964.9 | 7925.48 | 6303.8 | 0.376 | 0.463 |
| **IRMOF-6** | 6779.8 | 17257.72 | 0.65 | 3395.1 | 2206.8 | 12857.07 | 13286 | 1.180 | 0.745 |
| **IRMOF-7** | 7355.8 | 17231.09 | 0.71 | 3730.2 | 2648.4 | 12374.78 | 12776 | 1.046 | 0.718 |
| **IRMOF-8** | 7351.8 | 27247.8 | 0.448 | 4518.2 | 2024.2 | 22389.84 | 23345 | 1.912 | 0.822 |
| **IRMOF-9** | 3989.92 | 10099.64 | 0.658 | 4625.7 | 3043.7 | 7305.103 | 7626.4 | 1.151 | 0.723 |
| **IRMOF-10** | 7979.8 | 40285.53 | 0.33 | 5028.7 | 1659.5 | 34646.23 | 35695 | 2.694 | 0.860 |
| **IRMOF-12** | 9228.84 | 40285.53 | 0.382 | 5266.7 | 2001.3 | 33524.1 | 34942.5 | 2.280 | 0.832 |
| **IRMOF-14** | 9131.8 | 40641.59 | 0.37 | 4964.1 | 1836.7 | 34255.96 | 36147 | 2.384 | 0.843 |
| **IRMOF-15** | 2450.96 | 9882.179 | 0.413 | 6074.9 | 2508.9 | 7985.135 | 8298.6 | 2.039 | 0.808 |
| **IRMOF-16** | 9803.8 | 79399.44 | 0.205 | 6054.6 | 1241.2 | 71836.33 | 73072 | 4.489 | 0.905 |
| **IRMOF-18** | 8651.84 | 16803.77 | 0.858 | 2148.1 | 1836.6 | 11207.21 | 12377.6 | 0.862 | 0.667 |
| **IRMOF-Anthracene** | 8555.8 | 17587.56 | 0.808 | 2261.9 | 1827.6 | 11699.72 | 12823 | 0.903 | 0.665 |
| **Cu-BTC** | 9674.208 | 18276.2 | 0.879 | 2597.6 | 2282.7 | 12865.89 | 13529.36 | 0.801 | 0.704 |
| **Hupp-4** | 1959.085 | 3705.254 | 0.878 | 2420.2 | 2124.9 | 2212.9 | 2175.713 | 0.680 | 0.597 |
| **IRMOF-10-2** | 15972.25 | 40308.76 | 0.658 | n/a | n/a | 29008.75 | n/a | 1.094 | 0.720 |
| **IRMOF-10-3** | 23958.07 | 40308.25 | 0.987 | n/a | n/a | 23386.66 | n/a | 0.588 | 0.581 |
| **IRMOF-16-2** | 19624.71 | 79483.8 | 0.41 | n/a | n/a | 64274.34 | n/a | 1.974 | 0.810 |
| **IRMOF-16-3** | 29436.72 | 79482.87 | 0.615 | n/a | n/a | 56736.57 | n/a | 1.162 | 0.715 |

SA (surface area) calculated via Monte Carlo technique described in chapter 1; $H_2$ probe size: 2.958 Å; free volume was calculated via Monte Carlo technique described in chapter 1; pore volume calculated using method of Myers and Monson[23].

***Appendix B – Coordinate transformation***

# Unit Cell Geometry

*The unit cell is the smallest repeating array of atoms in a crystal that can generate the periodic structure with only translation operations.*

-Defined by coordinates of the atoms, and a set of vectors (**a**, **b**, and **c**) that precisely enclose the array of atoms and dictate the translation direction for the periodicity.

**Orthorhombic Unit Cell: vectors are ALL mutually orthogonal (i.e. $\alpha = \beta = \gamma = 90°$)**

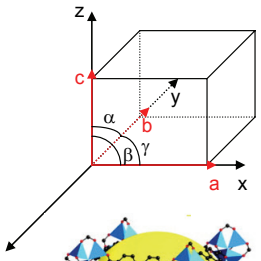


Example:

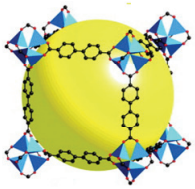

IRMOF-10

Vectors **a**, **b**, and **c** are typically given by three lengths or magnitudes (a, b, and c) and three angles ($\alpha$, $\beta$, and $\gamma$), where:

$\alpha$ is the angle between vectors **b** and **c**
$\beta$ is the angle between vectors **a** and **c**
$\gamma$ is the angle between vectors **a** and **b**

**Non-orthorhombic Unit Cell: vectors are NOT mutually orthogonal (i.e. $\alpha \neq \beta \neq \gamma \neq 90°$)**

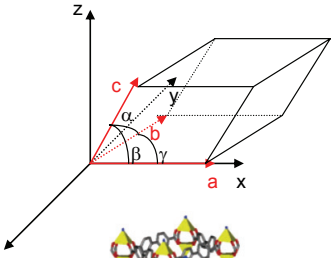


Example:

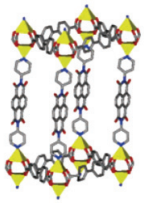

Hupp-5

- How do you determine vectors **a**, **b**, and **c**?

- 1st determine the starting point, or the desired orientation

The x-a convention:

1) Vector **a** coincides with x-axis.
2) Vector **b** lies in xy-plane.

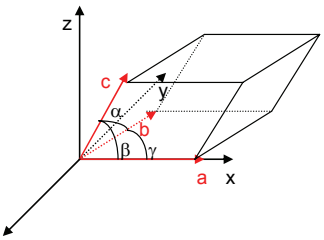


This allows for the determination of the vectors in cartesian space (x,y,z):

**a** = $(a_x,a_y,a_z)$ **b** = $(b_x,b_y,b_z)$ **c** = $(c_x,c_y,c_z)$

$$a_x = |\mathbf{a}| \qquad b_x = |\mathbf{b}|\cos(\gamma) \qquad c_x = |\mathbf{c}|\cos(\beta)$$
$$a_y = 0 \qquad b_y = |\mathbf{b}|\sin(\gamma) \qquad c_y = \frac{|\mathbf{b}||\mathbf{c}|\cos(\alpha) - b_x c_x}{b_y}$$
$$a_z = 0 \qquad b_z = 0 \qquad c_z = \sqrt{|\mathbf{c}|^2 - c_x^2 - c_y^2}$$

- How do we easily implement this in MuSiC and the surface area and free volume algorithm?

Transform the atomic coordinates from the Cartesian coordinate system (x,y,z) to arbitrary coordinate system (a,b,c) via transformation matrix:

$$\mathbf{T}_{xyz} = \begin{pmatrix} a_x & b_x & c_x \\ a_y & b_y & c_y \\ a_z & b_z & c_z \end{pmatrix} \qquad \begin{pmatrix} x \\ y \\ z \end{pmatrix} = \mathbf{T}_{xyz} \begin{pmatrix} a \\ b \\ c \end{pmatrix} \qquad \begin{pmatrix} a \\ b \\ c \end{pmatrix} = \mathbf{T}_{xyz}^{-1} \begin{pmatrix} x \\ y \\ z \end{pmatrix}$$

Turns out if we view the atoms with their coordinates defined in the arbitrary system in Cartesian space, it looks and behaves as if it is an orthorhombic system:

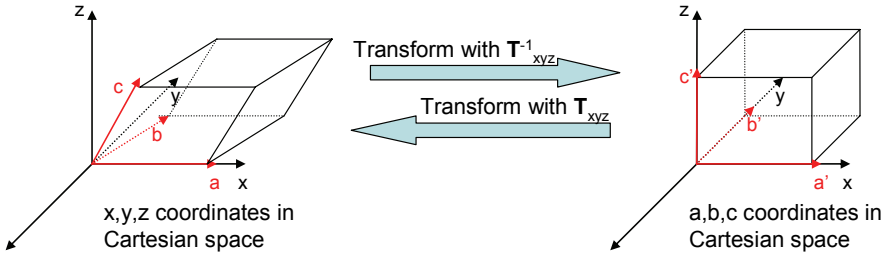

## ***Appendix C – Lennard-Jones parameters***

**Table C.1: Lennard-Jones parameters used in chapters 2 and 3**

| X: | $\sigma_{H2\text{-}X}$ (Å): | $\varepsilon_{H2\text{-}X}/k_b$ (K): |
|---|---|---|
| $H_2$ | 2.958 | 36.7 |
| C | 3.216 | 41.924 |
| H | 2.902 | 16.761 |
| O | 2.996 | 42.056 |
| Zn | 3.501 | 31.882 |

***Appendix D – Simulation methods, tabulated data, and supplemental info for chapter 6***

## Details of GCMC Simulations

The MOFs and carbon dioxide molecules were represented in atomistic detail. $CO_2$-$CO_2$ interactions were modeled using the TraPPE potential[125]. This model places a Lennard-Jones center on each carbon and oxygen atom, a point charge of +0.70 on the center of mass of the carbon atom, and a charge of -0.35 on each oxygen atom to simulate the molecule's quadrupole moment. The C-O bond length is 1.16 Å, and the bond angle is 180º. The Lennard-Jones parameters for the framework atoms were taken from the DREIDING force field[56]. Lorentz-Berthelot mixing rules were employed to calculate sorbate/framework parameters. Lennard-Jones interactions beyond 12.8 Å were neglected. All Lennard-Jones parameters are given in Table D.1.

No charges were used for the MOF frameworks. GCMC simulations which included $CO_2$-$CO_2$ electrostatic interactions agreed very well with experimental isotherms, and inclusion of framework charges did not provide any significant improvement to warrant the expensive Ewald calculations. For the $CO_2$-$CO_2$ Coulomb interactions, a cutoff based on the center-of-mass distance was used. This is justified (instead of the more expensive Ewald summation) because the $CO_2$-$CO_2$ quadrupole-quadrupole interaction is not long ranged.

Simulations were performed using the Music code[53]. For each point on the isotherm, 30 million Monte Carlo steps were performed. Each step consisted of insertion of a new molecule, deletion of an existing molecule, or translation of an existing molecule[52]. Typically, the first half of the run was used for equilibration, and the last half was used to calculate the ensemble averages.

The DREIDING forcefield was chosen for this work based upon its use in previous GCMC simulations of adsorption in MOFs. DREIDING has been shown to successfully reproduce adsorption isotherms for systems such as methane/IRMOFs[42] and hydrogen/IRMOFs[79]. Also, the model works well in reproducing heats of adsorption for hydrogen in the IRMOF materials[79]. In this work, we found very good agreement between simulations and experiment for $CO_2$ in IRMOFs using this model.

Table D.1. Lennard-Jones Parameters Used in GCMC Simulations

| Atom Pair | σ (Å) | $\varepsilon/k_b$ (K) |
|---|---|---|
| C—C | 2.80 | 27.0 |
| O—O | 3.05 | 79.0 |
| C—O | 2.93 | 36.0 |
| C—$C_{MOF}$ | 3.32 | 35.96 |
| C—$H_{MOF}$ | 2.82 | 14.38 |
| C—$O_{MOF}$ | 2.92 | 36.07 |
| C—$Zn_{MOF}$ | 3.42 | 27.35 |
| O—$C_{MOF}$ | 3.26 | 61.51 |
| O—$H_{MOF}$ | 2.95 | 24.59 |
| O—$O_{MOF}$ | 3.04 | 61.70 |
| O—$Zn_{MOF}$ | 3.55 | 46.78 |

Note: $C_{MOF}$ and $O_{MOF}$ are carbon and oxygen framework atoms. These have different force field parameters than the carbon and oxygen atoms in the $CO_2$ molecules.

Adsorption loadings obtained from GCMC simulations were converted from absolute loadings to excess loadings for comparison with experimental adsorption isotherms following the procedure given in Frost et al.[79] Gas-phase fugacities for carbon dioxide were calculated using the Peng-Robinson equation of state. The $CO_2$ bulk density was also calculated from this equation. Absolute adsorption loadings were converted to adsorbed-phase densities using the crystal structure free volumes. These values in $cm^3/g$ are 1.315, 2.615, and 4.413 for IRMOF-1, -10, and -16, respectively[79].

## Details of MOF Synthesis and Adsorption Measurements

MOF syntheses and adsorption experimental details for $CO_2$ isotherms at 298 K can be found in the cited literature[100].

For sub-ambient temperature $CO_2$ sorption experiments, a large batch of IRMOF-1 was prepared following a published procedure[16]. The supernatant from the as-synthesized IRMOF-1 was decanted and the crystals were rinsed with dimethylformamide (3 x 10 mL). The damp material was then immersed in 10 mL $CHCl_3$ to exchange out the solvent guests, and the $CHCl_3$ was refreshed thrice in three days.
Isotherms were collected manually on a previously-reported[6] discontinuous gravimetric sorption apparatus with a Cahn C-1000 microgravimetric balance (1 μg sensitivity) and two MKS Baratron 622 A pressure transducers (10 and 1000 torr, accuracy ± 0.25% of range) enclosed in a glass-ware system. An amount of damp, $CHCl_3$-exchanged IRMOF-1 was estimated so as to target an evacuated sample mass of 400 to 600 mg. The sample

was loaded with minimal exposure to air into a tared cylindrical quartz sample bucket (30 mm height, 18 mm diameter, 4 g weight), and then mounted on the balance and enclosed in the system.

To activate the damp sample *in situ*, the system pressure was reduced slowly to avoid elutriation ("bumping") until the sample mass was constant (within 0.05 mg) at room temperature and full vacuum ($<10^{-3}$ torr). To obtain sub-ambient temperature $CO_2$ isotherms the system temperature was monitored by a thermocouple suspended in close proximity to the sample bucket while the sample chamber was bathed in various slushes: acetone/dry ice (195 K), chloroform/$LN_2$ (208 K), acetone/water/dry ice (218 K), acetonitrile/$LN_2$ (233 K) and ice water (273 K). Attempts to carefully maintain both the level and consistency of the baths were achieved by occasional stirring and addition of cryogen.

To obtain each isotherm, the initial weight of the sample under vacuum was recorded after applying the isotherm bath. The $CO_2$ (Bone Dry) adsorbate was added incrementally and data points were recorded when no further change in mass was observed (< 0.05 mg/min). An empirical buoyancy correction was applied to all data points based on the weight change of standard aluminum foil weights within the analyte gas.

Table D.2: $CO_2$ Adsorption and Desorption Data for IRMOF-1 at 195K

| $P_{eq}$(torr) | $Wt_{buoy}$(mg) | N(mg/g) | $P_{eq}$(torr) | $Wt_{buoy}$(mg) | N(mg/g) |
|---|---|---|---|---|---|
| 0 | 171.5 | 0.0 | 751 | 426.9 | 1489.0 |
| 12 | 176.0 | 26.3 | 700 | 426.8 | 1488.2 |
| 40 | 183.1 | 67.5 | 600 | 425.5 | 1480.9 |
| 74 | 191.7 | 117.6 | 511 | 423.3 | 1467.9 |
| 104.8 | 200.7 | 169.9 | 341 | 414.9 | 1418.8 |
| 116.2 | 205.0 | 195.2 | 260 | 409.7 | 1388.4 |
| 125.3 | 208.5 | 215.7 | 197 | 400.5 | 1335.0 |
| 135.6 | 213.8 | 246.8 | 180 | 397.5 | 1317.3 |
| 145 | 229.4 | 337.3 | 160 | 392.4 | 1287.8 |
| 150 | 315.4 | 838.7 | 150 | 384.4 | 1241.0 |
| 155 | 386.4 | 1252.8 | 146 | 320.4 | 867.8 |
| 165 | 391.4 | 1282.1 | 143 | 240.4 | 401.4 |
| 175 | 394.4 | 1299.7 | 136 | 216.3 | 261.3 |
| 190 | 397.5 | 1317.4 | 125 | 210.3 | 226.2 |
| 215 | 402.5 | 1346.9 | 110 | 203.3 | 185.2 |
| 250 | 407.6 | 1376.6 | 90 | 196.2 | 144.1 |
| 301 | 410.8 | 1394.9 | 29 | 181.1 | 55.7 |
| 350 | 413.9 | 1413.1 | 0 | 173.0 | 8.6 |
| 450 | 419.1 | 1443.7 | | | |
| 547 | 422.4 | 1462.6 | | | |
| 654 | 424.7 | 1475.9 | | | |
| 751 | 426.9 | 1489.0 | | | |

Table D.3: $CO_2$ Adsorption and Desorption Data for IRMOF-1 at 208K

| $P_{eq}$(torr) | $Wt_{buoy}$(mg) | N(mg/g) | $P_{eq}$(torr) | $Wt_{buoy}$(mg) | N(mg/g) |
|---|---|---|---|---|---|
| 0 | 171.2 | 0.0 | 750.2 | 411.7 | 1405.5 |
| 10.7 | 173.4 | 13.3 | 696 | 408.8 | 1388.4 |
| 54.7 | 180.1 | 52.5 | 550 | 401.4 | 1345.3 |
| 92.6 | 186.7 | 91.1 | 375 | 391.0 | 1284.3 |
| 121.4 | 191.8 | 120.7 | 293 | 381.7 | 1230.5 |
| 142.2 | 195.9 | 144.4 | 285 | 380.7 | 1224.5 |
| 156.9 | 198.3 | 158.6 | 275 | 378.7 | 1212.7 |
| 190.5 | 205.8 | 202.4 | 255 | 280.6 | 639.8 |
| 238.1 | 223.4 | 305.3 | 240 | 228.6 | 335.7 |
| 249.1 | 234.3 | 369.2 | 175 | 202.4 | 182.9 |
| 266 | 280.7 | 639.9 | 75 | 184.2 | 76.2 |
| 273.7 | 365.7 | 1136.7 | 0 | 172.0 | 5.0 |
| 300.1 | 380.8 | 1224.7 | | | |
| 336.5 | 386.9 | 1260.3 | | | |
| 362.3 | 388.9 | 1272.4 | | | |
| 427.5 | 393.1 | 1296.7 | | | |
| 510.3 | 399.3 | 1333.0 | | | |
| 605.6 | 404.5 | 1363.7 | | | |
| 750.2 | 411.7 | 1405.5 | | | |

Table D.4: $CO_2$ Adsorption and Desorption Data for IRMOF-1 at 218K

| $P_{eq}$(torr) | $Wt_{buoy}$(mg) | N(mg/g) | $P_{eq}$(torr) | $Wt_{buoy}$(mg) | N(mg/g) |
|---|---|---|---|---|---|
| 0 | 171.5 | 0.0 | 750 | 382.9 | 1232.4 |
| 30 | 174.1 | 14.9 | 713 | 378.8 | 1208.6 |
| 102 | 181.3 | 56.8 | 580 | 365.5 | 1130.8 |
| 145 | 185.4 | 80.7 | 542 | 356.4 | 1077.8 |
| 204 | 191.5 | 116.6 | 510 | 336.3 | 960.7 |
| 276 | 200.7 | 170.1 | 490 | 279.2 | 628.1 |
| 347 | 210.9 | 229.5 | 455 | 229.2 | 336.0 |
| 402 | 220.0 | 282.8 | 358 | 213.9 | 247.1 |
| 448 | 229.1 | 335.9 | 257 | 198.7 | 158.2 |
| 485 | 261.2 | 523.1 | 177 | 189.5 | 104.5 |
| 503 | 304.3 | 774.0 | 75 | 178.2 | 38.9 |
| 525 | 347.3 | 1025.0 | | | |
| 535 | 355.4 | 1071.8 | | | |
| 550 | 361.4 | 1107.0 | | | |
| 601 | 368.5 | 1148.6 | | | |
| 642 | 371.6 | 1166.7 | | | |
| 688 | 376.8 | 1196.5 | | | |
| 750 | 382.9 | 1232.4 | | | |

Table D.5: $CO_2$ Adsorption and Desorption Data for IRMOF-1 at 233K

| $P_{eq}$(torr) | $Wt_{buoy}$(mg) | N(mg/g) | $P_{eq}$(torr) | $Wt_{buoy}$(mg) | N(mg/g) |
|---|---|---|---|---|---|
| 0 | 191.1 | 0.0 | 735.8 | 248.2 | 298.7 |
| 11.9 | 191.8 | 3.8 | 675 | 238.7 | 249.3 |
| 52.3 | 194.1 | 15.6 | 548 | 226.4 | 184.8 |
| 91.5 | 196.3 | 27.3 | 300 | 208.8 | 92.5 |
| 125.6 | 198.2 | 37.4 | 195.3 | 202.2 | 58.0 |
| 147.3 | 199.4 | 43.7 | | | |
| 154.5 | 199.9 | 46.1 | | | |
| 196.1 | 202.4 | 59.1 | | | |
| 240 | 205.1 | 73.4 | | | |
| 353.7 | 212.3 | 111.3 | | | |
| 491.5 | 222.8 | 166.1 | | | |
| 603.9 | 232.0 | 214.3 | | | |
| 735.8 | 248.2 | 298.7 | | | |

Table D.6: $CO_2$ Adsorption and Desorption Data for IRMOF-1 at 273K

| $P_{eq}$(torr) | $Wt_{buoy}$(mg) | N(mg/g) | $P_{eq}$(torr) | $Wt_{buoy}$(mg) | N(mg/g) |
|---|---|---|---|---|---|
| 0 | 191.1 | 0.0 | 748.4 | 203.7 | 66.1 |
| 12 | 191.3 | 1.2 | 424.8 | 198.1 | 36.8 |
| 50.4 | 191.9 | 4.4 | 163.1 | 193.8 | 14.3 |
| 91.2 | 192.6 | 8.1 | 0 | 191.1 | 0.0 |
| 126.4 | 193.2 | 11.0 | | | |
| 144.6 | 193.5 | 12.5 | | | |
| 153.7 | 193.7 | 13.5 | | | |
| 191.7 | 194.3 | 16.6 | | | |
| 250.6 | 195.2 | 21.7 | | | |
| 340 | 196.7 | 29.2 | | | |
| 498.3 | 199.2 | 42.3 | | | |
| 592.1 | 200.9 | 51.5 | | | |
| 748.4 | 203.7 | 66.1 | | | |

Figure D.1: $CO_2$ sorption isotherms for IRMOF-1 from 195 to 273K. Filled circles are adsorption; open circles are desorption.

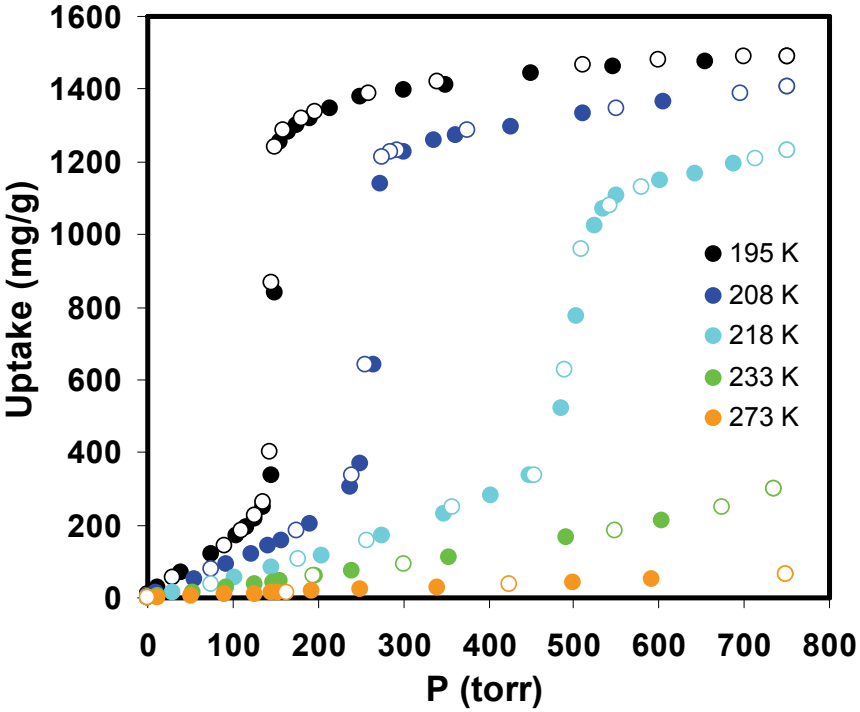

Table D.7: $CO_2$ Adsorption and Desorption Data for IRMOF-1 at 298K

| $P_{eq}$(psia) | $Wt_{buoy}$(mg) | N(mg/g) | $P_{eq}$(psia) | $Wt_{buoy}$(mg) | N(mg/g) |
|---|---|---|---|---|---|
| 0.0 | 24.05 | 0.00 | 612.9 | 47.34 | 968.19 |
| 17.8 | 25.19 | 47.30 | 317.0 | 45.05 | 872.60 |
| 30.1 | 26.00 | 81.03 | 168.3 | 38.03 | 581.11 |
| 46.3 | 27.02 | 123.07 | 15.0 | 25.05 | 41.45 |
| 60.1 | 27.97 | 162.85 | | | |
| 77.0 | 29.24 | 215.75 | | | |
| 92.1 | 30.48 | 267.22 | | | |
| 104.3 | 31.54 | 311.34 | | | |
| 119.0 | 32.95 | 369.87 | | | |
| 136.3 | 34.72 | 443.26 | | | |
| 150.9 | 36.24 | 506.46 | | | |
| 166.5 | 37.78 | 570.77 | | | |
| 178.6 | 38.84 | 614.66 | | | |
| 195.0 | 40.12 | 667.69 | | | |
| 209.2 | 41.05 | 706.44 | | | |
| 224.9 | 41.90 | 741.85 | | | |
| 240.7 | 42.65 | 773.13 | | | |
| 255.2 | 43.25 | 797.86 | | | |
| 269.4 | 43.71 | 817.05 | | | |
| 285.4 | 44.19 | 836.97 | | | |
| 299.2 | 44.56 | 852.34 | | | |
| 313.7 | 44.85 | 864.69 | | | |
| 347.2 | 45.52 | 892.29 | | | |
| 372.8 | 45.89 | 907.80 | | | |
| 404.7 | 46.28 | 923.98 | | | |
| 436.0 | 46.60 | 937.04 | | | |
| 463.8 | 46.82 | 946.28 | | | |
| 494.6 | 47.00 | 953.89 | | | |
| 524.7 | 47.13 | 959.23 | | | |
| 554.3 | 47.25 | 964.27 | | | |
| 584.0 | 47.32 | 967.02 | | | |
| 612.9 | 47.34 | 968.19 | | | |

Table D.8: $CO_2$ Adsorption and Desorption Data for IRMOF-3 at 298K

| $P_{eq}$(psia) | $Wt_{buoy}$(mg) | N(mg/g) | $P_{eq}$(psia) | $Wt_{buoy}$(mg) | N(mg/g) |
|---|---|---|---|---|---|
| 0.0 | 43.82 | 0.00 | 612.9 | 80.19 | 829.91 |
| 16.2 | 46.18 | 53.64 | 416.7 | 79.30 | 809.40 |
| 30.1 | 48.36 | 103.55 | 216.6 | 74.67 | 703.95 |
| 48.1 | 51.41 | 172.99 | 107.8 | 63.22 | 442.59 |
| 61.0 | 53.71 | 225.62 | 14.3 | 45.99 | 49.35 |
| 75.2 | 56.51 | 289.50 | 0.0 | 43.83 | 0.23 |
| 90.1 | 59.49 | 357.47 | | | |
| 105.5 | 62.51 | 426.30 | | | |
| 121.0 | 65.22 | 488.18 | | | |
| 135.2 | 67.48 | 539.86 | | | |
| 148.9 | 69.21 | 579.21 | | | |
| 164.3 | 70.86 | 616.82 | | | |
| 180.1 | 72.20 | 647.59 | | | |
| 194.1 | 73.17 | 669.72 | | | |
| 208.3 | 74.07 | 690.05 | | | |
| 224.8 | 74.88 | 708.69 | | | |
| 239.5 | 75.50 | 722.83 | | | |
| 255.4 | 76.11 | 736.66 | | | |
| 269.5 | 76.57 | 747.09 | | | |
| 284.3 | 76.98 | 756.60 | | | |
| 298.3 | 77.34 | 764.66 | | | |
| 315.1 | 77.73 | 773.69 | | | |
| 343.4 | 78.23 | 785.00 | | | |
| 376.8 | 78.75 | 797.04 | | | |
| 406.0 | 79.12 | 805.45 | | | |
| 432.8 | 79.43 | 812.39 | | | |
| 462.2 | 79.64 | 817.35 | | | |
| 504.3 | 79.94 | 824.21 | | | |
| 523.6 | 79.99 | 825.17 | | | |
| 554.0 | 80.10 | 827.73 | | | |
| 581.6 | 80.16 | 829.19 | | | |
| 612.9 | 80.19 | 829.91 | | | |

Table D.9: $CO_2$ Adsorption and Desorption Data for MOF-177 at 298K

| $P_{eq}$(psia) | $Wt_{buoy}$(mg) | N(mg/g) | $P_{eq}$(psia) | $Wt_{buoy}$(mg) | N(mg/g) |
|---|---|---|---|---|---|
| 0.0 | 16.01 | 0.00 | 616.0 | 39.91 | 1493.48 |
| 14.9 | 16.57 | 35.13 | 314.4 | 36.71 | 1293.68 |
| 31.4 | 17.26 | 78.55 | 212.5 | 30.77 | 922.56 |
| 45.2 | 17.89 | 117.56 | 116.5 | 21.92 | 369.31 |
| 59.1 | 18.53 | 157.41 | | | |
| 76.0 | 19.37 | 210.11 | | | |
| 89.9 | 20.14 | 258.00 | | | |
| 106.0 | 21.11 | 318.84 | | | |
| 120.4 | 22.04 | 377.14 | | | |
| 135.0 | 23.13 | 444.79 | | | |
| 149.7 | 24.33 | 520.01 | | | |
| 165.9 | 25.80 | 611.52 | | | |
| 179.9 | 27.13 | 695.22 | | | |
| 195.8 | 28.70 | 793.23 | | | |
| 209.7 | 30.08 | 879.19 | | | |
| 225.7 | 31.64 | 976.49 | | | |
| 239.4 | 32.90 | 1055.08 | | | |
| 254.0 | 34.04 | 1126.59 | | | |
| 270.1 | 34.96 | 1184.34 | | | |
| 287.2 | 35.72 | 1231.85 | | | |
| 299.7 | 36.21 | 1262.03 | | | |
| 316.5 | 36.76 | 1296.58 | | | |
| 343.4 | 37.51 | 1343.22 | | | |
| 374.6 | 38.14 | 1383.04 | | | |
| 402.9 | 38.61 | 1412.29 | | | |
| 444.1 | 39.14 | 1444.99 | | | |
| 463.6 | 39.30 | 1455.05 | | | |
| 492.6 | 39.51 | 1468.60 | | | |
| 523.7 | 39.70 | 1480.31 | | | |
| 555.6 | 39.78 | 1485.41 | | | |
| 582.8 | 39.89 | 1491.87 | | | |
| 616.0 | 39.91 | 1493.48 | | | |

Figure D.2: $CO_2$ sorption isotherms for IRMOF-1, IRMOF-3 and MOF-177 at 298K. Filled circles are adsorption; open circles are desorption.

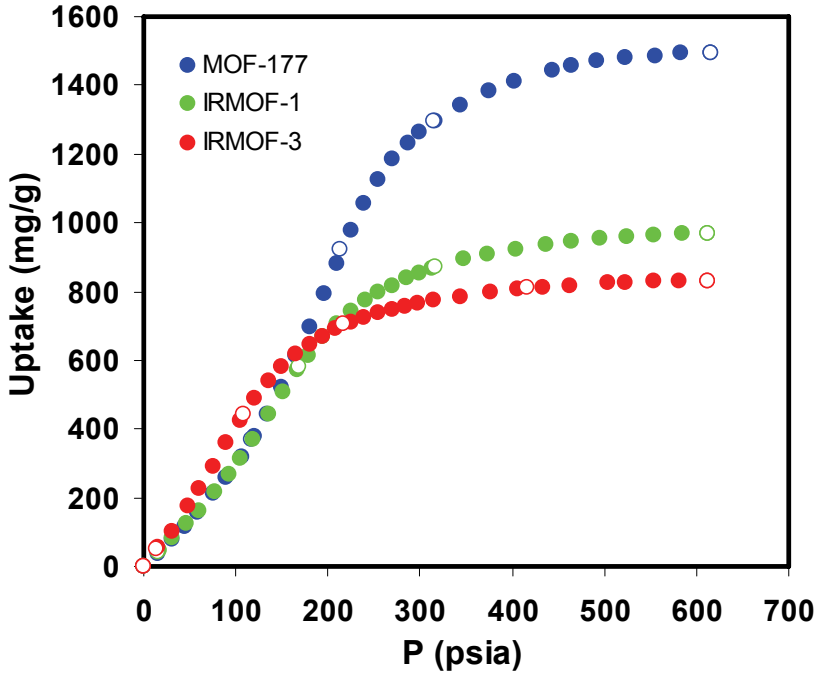

## ***Appendix E – MOF atomic charges***

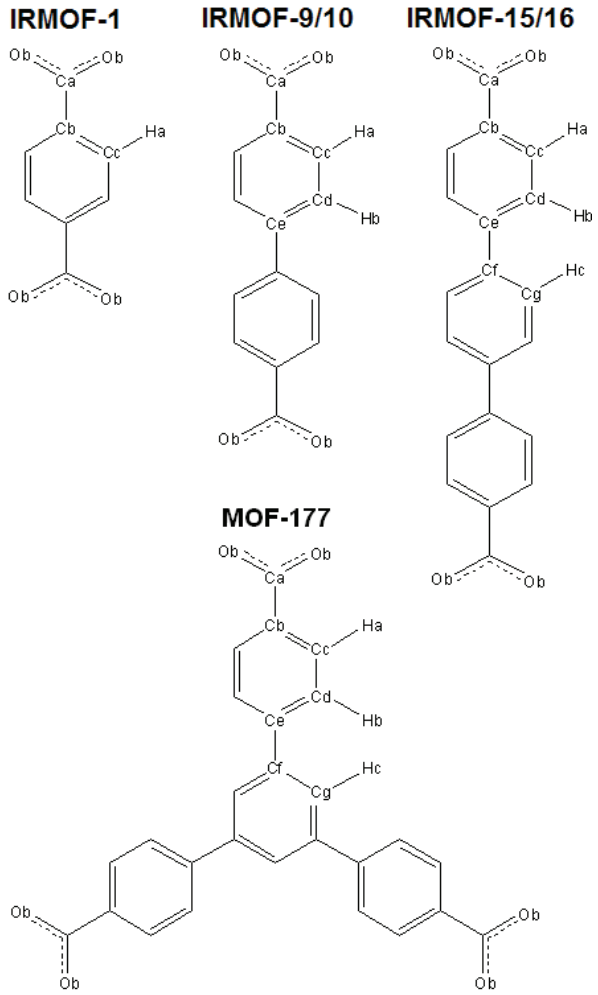


| Material | Zn | Oa | Ob | Ca | Cb | Cc | Cd | Ce | Cf | Cg | Ha | Hb | Hc |
|---|---|---|---|---|---|---|---|---|---|---|---|---|---|
| **IRMOF-1** | 1.29 | -1.56 | -0.59 | 0.47 | 0.13 | -0.16 | *** | *** | *** | *** | 0.16 | *** | *** |
| **IRMOF-9/10** | 1.27 | -1.53 | -0.61 | 0.52 | 0.13 | -0.17 | -0.19 | 0.09 | *** | *** | 0.15 | 0.15 | *** |
| **IRMOF-15/16** | 1.49 | -1.71 | -0.78 | 0.82 | -0.03 | -0.12 | -0.17 | 0.09 | 0.04 | -0.15 | 0.15 | 0.13 | 0.14 |
| **MOF-177** | 1.39 | -1.62 | -0.70 | 0.58 | 0.24 | -0.23 | -0.16 | 0.13 | 0.12 | -0.23 | 0.17 | 0.12 | 0.11 |

**IRMOF-6**

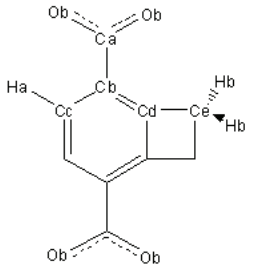


**IRMOF-7**

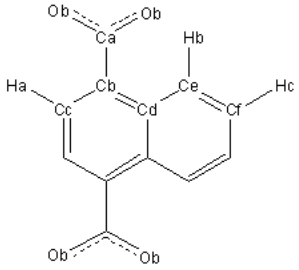


**IRMOF-8**

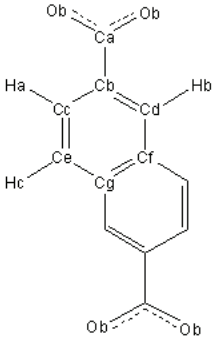


| Material | Zn | Oa | Ob | Ca | Cb | Cc | Cd | Ce | Cf | Ha | Hb | Hc |
|---|---|---|---|---|---|---|---|---|---|---|---|---|
| **IRMOF-6** | 1.25 | -1.50 | -0.60 | 0.52 | 0.17 | -0.21 | -0.11 | 0.11 | *** | 0.14 | 0.00 | *** |
| **IRMOF-7** | 1.39 | -1.60 | -0.71 | 0.72 | -0.06 | -0.15 | 0.14 | -0.25 | -0.11 | 0.16 | 0.18 | 0.14 |
| **IRMOF-8** | 1.39 | -1.64 | -0.69 | 0.70 | 0.06 | -0.19 | -0.26 | -0.26 | 0.16 | 0.17 | 0.17 | 0.17 |

**IRMOF-11/12**

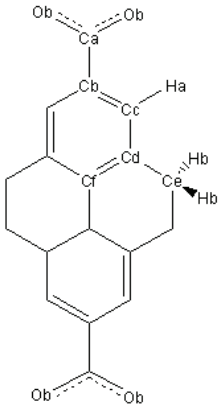


**IRMOF-13/14**

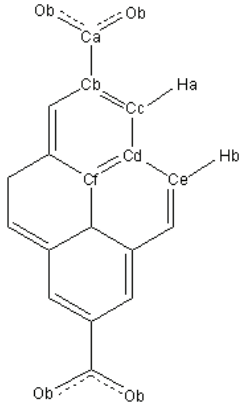


**IRMOF-Anthracene**

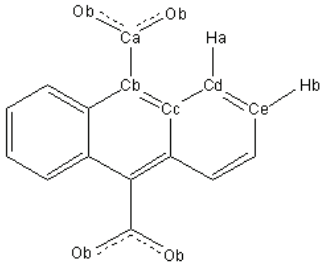


| Material | Zn | Oa | Ob | Ca | Cb | Cc | Cd | Ce | Cf | Ha | Hb |
|---|---|---|---|---|---|---|---|---|---|---|---|
| **IRMOF-11/12** | 1.32 | -1.57 | -0.67 | 0.70 | 0.10 | -0.32 | 0.10 | -0.09 | -0.02 | 0.16 | 0.06 |
| **IRMOF-13/14** | 1.36 | -1.62 | -0.69 | 0.68 | 0.12 | -0.30 | 0.14 | -0.22 | 0.03 | 0.20 | 0.15 |
| **IRMOF-Anthracene** | 1.28 | -1.55 | -0.64 | 0.62 | -0.19 | 0.16 | -0.29 | -0.08 | *** | 0.25 | 0.10 |

**IRMOF-2**

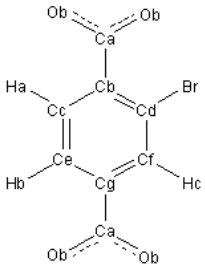


**IRMOF-3**

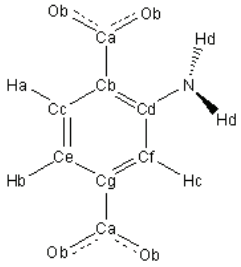


**IRMOF-18**

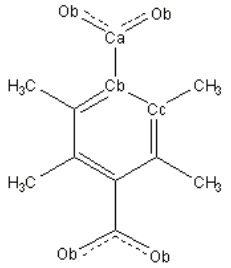


**IRMOF-4**

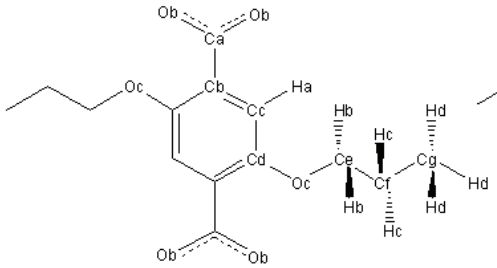


**IRMOF-5**

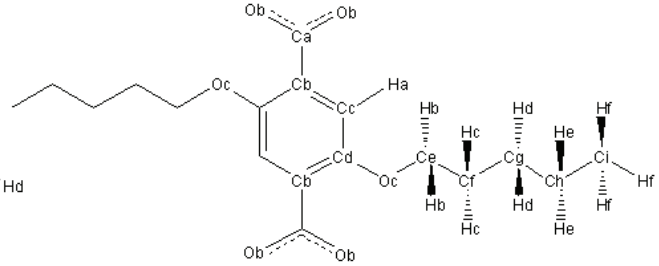


| Material | Zn | Oa | Ob | Oc | Ca | Cb | Cc | Cd | Ce | Cf | Cg | Ch | Ci | Ha | Hb | Hc | Hd | He | Hf | Br or N |
|---|---|---|---|---|---|---|---|---|---|---|---|---|---|---|---|---|---|---|---|---|
| **IRMOF-2** | 1.37 | -1.63 | -0.67 | *** | 0.63 | 0.26 | -0.25 | -0.10 | -0.14 | -0.05 | 0.09 | *** | *** | 0.17 | 0.14 | 0.08 | *** | *** | *** | -0.09 |
| **IRMOF-3** | 1.34 | -1.59 | -0.67 | *** | 0.65 | -0.08 | -0.16 | 0.51 | -0.24 | -0.36 | 0.14 | *** | *** | 0.16 | 0.15 | 0.20 | 0.48 | *** | *** | -1.14 |
| **IRMOF-4** | 1.29 | -1.55 | -0.61 | -0.45 | 0.54 | 0.08 | -0.38 | 0.27 | 0.28 | 0.06 | -0.12 | *** | *** | 0.22 | 0.00 | 0.01 | 0.03 | *** | *** | *** |
| **IRMOF-5** | 1.33 | -1.59 | -0.64 | -0.29 | 0.63 | -0.10 | -0.26 | 0.29 | 0.21 | -0.06 | -0.09 | 0.28 | -0.32 | 0.15 | 0.01 | 0.03 | 0.02 | -0.03 | 0.06 | *** |
| **IRMOF-18** | 1.31 | -1.61 | -0.69 | | 0.86 | -0.21 | 0.02 | *** | the | $CH_3$ | group | has | zero | charge | | | | | | |

**Cu-BTC**

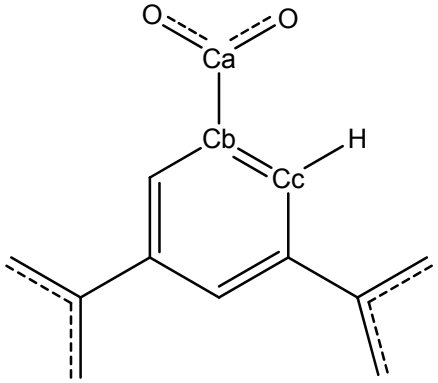


| Atom | Cu-BTC atom charges |
|---|---|
| Cu | 1.00 |
| O | -0.59 |
| Ca | 0.67 |
| Cb | -0.04 |
| Cc | -0.11 |
| Ha | 0.14 |